University of New Mexico
UNM Digital Repository

Nuclear Engineering ETDs | Engineering ETDs

6-26-2015

Ionization Chamber Design, Development, and Testing for the UNM Fission Fragment Spectrometer

Lena Heffern

Follow this and additional works at: https://digitalrepository.unm.edu/ne_etds

Recommended Citation
Heffern, Lena. "Ionization Chamber Design, Development, and Testing for the UNM Fission Fragment Spectrometer." (2015).
https://digitalrepository.unm.edu/ne_etds/46

This Thesis is brought to you for free and open access by the Engineering ETDs at UNM Digital Repository. It has been accepted for inclusion in Nuclear Engineering ETDs by an authorized administrator of UNM Digital Repository. For more information, please contact disc@unm.edu.

Lena Heffern

Candidate

Chemical & Nuclear Engineering

Department

This thesis is approved, and it is acceptable in quality and form for publication:

Approved by the Thesis Committee:

Dr. Adam Hecht, Chairperson

Dr. Robert Busch

Dr. Gary Cooper

Ionization Chamber Design, Development, and Testing for the UNM Fission Fragment Spectrometer

By

Lena E. Heffern

Bachelor of Science – Mechanical Engineering, Physics 2013

California State University: Chico

Submitted in Partial Fulfillment of the
Requirements for the Degree of

Master of Science

Nuclear Engineering

The University of New Mexico
Albuquerque, New Mexico

May 2015

Ionization Chamber for Design, Development, and Testing for the UNM Fission Fragment Spectrometer

by

Lena Heffern

B.S., Mechanical Engineering, Physics, CSU Chico, 2013

M.S., Nuclear Engineering, University New Mexico, 2015

ABSTRACT

Fission fragment and product inventories play an important role in many areas of nuclear science from simulation of fissioning systems to active and passive interrogation of nuclear materials. The characteristic properties of fission fragment distributions are currently lacking in experimental data. New data is needed to reduce the uncertainty in the current standard data and to expand on current data for other incident neutron energies.

To attain the goal of new fission fragment data, the Spectrometer for Ion Detection in Fission Research (SPIDER) project is currently underway at Los Alamos National Labortory (LANL). The SPIDER project is intended to be a multi-armed spectrometer that will use high resolution measurements and event by-event analysis to add to the library of nuclear fission data. Our group at the

University of New Mexico is working as a collaborator on the SPIDER project to achieve a mass resolution of 1 amu with our own UNM fission fragment spectrometer. Mass is determined by combining particle-by-particle data from a time-of-flight detector and an ionization chamber energy detector. Our UNM spectrometer will also be capable of gathering fission fragment charge (Z) data, due to the addition of an active cathode in the ionization chamber. Preliminary testing has already taken place at the LANSCE facility at Los Alamos, resulting in uncorrelated energy and timing data. Futher data will be taken at a later date at the LANSCE facility.

The UNM ionization chamber has achieved uncorrelated, uncalibrated preliminary results at LANL for fission fragment energy distributions at the LANSCE facility. A current energy resolution of 1.5% at high pressures for alpha particles has been measured. In addition to energy measurements, the ionization chamber has achieved measuring the range of alpha particles and both light and heavy fission fragments through use of an active cathode. Further characterizing has also been done on the ionization chamber to better understand the effects of internal andexternal variables on energy resolution and particle range measurement.

TABLE OF CONTENTS

Ionization Chamber Design, Development, and Testing for the UNM Fission Fragment Spectrometer **ii**

ABSTRACT *iii*
ACKNOWLEDGEMENTS *vii*
INDEX OF FIGURES *viii*
INDEX OF TABLES *xv*

Chapter 1: Introduction & Purpose **1**

1.1 Overview *1*
1.2 Background and Prior Work *5*
1.3 Organization of Thesis *8*

Chapter 2: Theory **10**

2.1 2E-2V Method *10*
2.2 Time of Flight *14*
2.3 Ionization Chamber *17*
2.3.1 Characteristics 17
2.3.1 Energy Resolution 23
2.4 Charge Mobility *27*
2.5 Ion Interactions *31*
2.6 Particle Charge and Range *35*
2.6.1 Bragg Curve Spectroscopy 36
2.6.2 Active Cathode 44

Chapter 3: Overview of Instrumentation **48**

3.1 Ionization Chamber Physical Design *48*
3.1.1 Anode-Guard Ring Sub-assembly 52
3.1.2 Window-cathode Sub-assembly 54
3.1.3 Frisch Grid 57
3.2 Ionization Gas *57*
3.3 Ionization Chamber Signal Processing *58*
3.4 Data Acquisition System *61*
3.4.1 Main DAQ 61
3.4.2 Arduino Environmental DAQ 63

Chapter 4: Experiments & Results **65**

4.1 Introduction *65*

4.2 Experimental System 65
4.2 Window Thickness Pressure Tests 66
4.3 Pressure Tests 70
4.4 Peak Drift 72
4.4.1 External Environmental Effects 73
4.4.2 Gas Flow 75
4.4.3 Peak drift stability 78
4.5 Voltage Tests or E/P 80
4.5.1 Energy Resolution 80
4.6 Alpha Range Tests 81
4.7 Lateral Measurements 83
4.8 Noise Reduction 84
4.9 Z Determination 86
4.9.1 Bragg Curve Spectroscopy 87
4.9.2 Active Cathode Energy Extension 89

Chapter 5: Preliminary Analyses of Charge and Mass **95**

5.1 LANL Preliminary Energy Data 95
5.2 Energy Loss and Straggling 96
5.3 Active Cathode Analysis 101
5.4 Preliminary Calculations of Mass 106

Chapter 6: Conclusions & Future Work **111**

6.1 Combined Spectrometer and Window 112
6.2 Energy Measurement 113
6.3 Range Measurement 113
6.4 Spectrometer Arms 114
6.5 Chamber Gas 115
6.6 Testing Facilities 116

Bibliography **117**

Appendix A **123**

A.1 IC Assembly Design Drawings 123
A.2 LANL Window Design Drawings 141

Appendix B **145**

B.1 Environmental DAQ Python Code 145

ACKNOWLEDGEMENTS

I'd like to begin by thanking my family: my parents, Karen and James Heffern, and my brothers Robert and Brian Heffern for their unconditional support. Without them, my accomplishments wouldn't be possible.

I'd also like to thank my adviser Dr. Adam Hecht for his diligent efforts in setting up beneficial projects and opportunities. Thank you to professors Dr. Robert Busch, Dr. Gary Cooper, and Dr. Anil Prinja for their support. I'd also like to thank Anthony Gravange for putting up with our re-machining demands.

I'd especially like to thank my undergraduate physics professors Dr. Eric Ayars, Dr. David Kagan, Dr. Louis Buccholtz, Dr. Xeuli Zou, Dr. Chris Gaffney, Dr. Anna Petrova-Mayor, and Dr. Eric Dietz for their continuing advice, support, and mentorship throughout my academic and professional career. Thank you to Dr. Morgan Burks and Tom Gosnell at LLNL for inspiring me in the first place.

Finally, and most of all, I want to thank my fellow lab group members and friends: Rick Blakeley, James Cole, Corey Vowell, Paul Gilbreath, and Patrick O'Rourke, for their support both in and out of the lab.

INDEX OF FIGURES

Figure 1: Schematic view of a single-arm spectrometer.

Figure 2: Proposed two arm fission fragment spectrometer configuration.

Figure 3: Light fragment mass distribution measured using the Cosi Fan Tutte Spectrometer [Boucheneb, 1989].

Figure 4: Nuclear charge distribution for A=87 measured using the Cosi Fan Tutte spectrometer [Boucheneb, 1989].

Figure 5: Solid CAD model of the single arm UNM fission fragment spectrometer.

Figure 6: Illustration of the timing module, with carbon foil at right, electrostatic mirror at left, and MCP at bottom.

Figure 7: Photograph of the copper faced FR4 plastic mirror frames.

Figure 8: Solid CAD model of the TOF mirror assembly.

Figure 9: Electrode grid geometry of the electrostatic mirror [Blakeley, 2013].

Figure 10: Basic design of a transverse ionization chamber [Mader, 2013].

Figure 11: Basic design of an axial ionization chamber [based on Knoll, 2000].

Figure 12: Pulse height vs. V curve for a gas detector [Knoll, 2000].

Figure 13: Definition of detector resolution, from [Knoll, 2000]. For peaks whose shape is Gaussian with standard deviation σ, the FWHM is 2.35σ.

Figure 14: E/P vs. electron drift velocity curve for P-10 gas as calculated based on empirical equations from Khryachkov et al. [Khryachkov, 2003].

Figure 15: E/P vs. electron drift velocity for isobutane gas [Peisert, 1984].

Figure 16: Bragg curve as simulated using SRIM [Ziegler, 2014] for a ^{239}Pu alpha particle in P-10 gas.

Figure 17: The Bragg curve for three different energy alphas [Mader, 2013].

Figure 18: SRIM alpha particle [Zeigler, 2014] simulation superimposed onto a SIMION electric field simulation result [Mader, 2013]. The cathode is on the left, Frisch grid on the right, and anode on the far right.

Figure 19: The Bragg peak vs. deposited energy for particles of different mass and atomic charge [Sanami, 2008].

Figure 20: Bragg curve for a light (> 1 MeV/amu) fission fragment in P-10 gas.

Figure 21: Bragg curve for a heavy (< 1 MeV/amu) fission fragment in P-10 gas.

Figure 22: Schematic diagram of a Bragg curve counter; d is the cathode-grid distance, Fr is the particle range, and x is the distance from the cathode to the center of gravity of the charge [Sanami, 2008].

Figure 23: Signals from the charge sensitive preamplifiers connected to the cathode and anode. Left, diagram from ref [Sanami, 2008]; the point at t = 0 corresponds to the fragment incident time. Right, oscilloscope traces from our early tests.

Figure 24: Active Cathode particle range results from Sanami [Sanami, 2008].

Figure 25: Schematic drawing of the ionization chamber for the UNM fission fragment spectrometer.

Figure 26: Solid CAD cut-away model of the UNM ionization chamber.

Figure 27: SIMION simulated electric field lines inside of a previous iteration of the UNM IC [Mader, 2013].

Figure 28: Exploded solid CAD model of the two IC sub-assemblies; the cathode-window sub-assembly (left) and the anode-guard ring sub-assembly (right).

Figure 29: Solid CAD model of the anode-guard ring sub-assembly.

Figure 30: Exploded solid CAD model of the window-cathode sub-assembly.

Figure 31: The output voltage as a function of time, where 0 to t- is the rise time of electrons and t- to t+ is the rise time of the ions [Ahmed, 2007].

Figure 32: Schematic of the original DAQ for the IC, using Maestro.

Figure 33: Electronics schematic of the signal processing and data collection system for the DAQ.

Figure 34: Photo of the Arduino circuit and sensor used to measure internal pressure, external pressure, and temperature over time.

Figure 35: Original wire mesh window backing for the TOF-IC window.

Figure 36: "Saltshaker" window backing with the surrounding window frame for the TOF-IC window. The mylar is stretched across, and epoxyed to, the window frame.

Figure 37: Graph showing the effect of pressure vs. alpha (5156 keV) energy resolution when the drift velocity (related to E/P) is kept constant.

Figure 38: Graph showing the effect of different E/P values at different pressures vs. alpha (5156 keV) energy resolution.

Figure 39: (top) ^{252}Cf alpha particle energy data taken for 7200 s (2 hrs), showing no centroid drift; (bottom) ^{252}Cf and ^{239}Pu alpha particle energy data taken for 7200 s, showing centroid drift.

Figure 40: Data showing no correlation between IC peak centroid location from alpha particle radiation (top), external temperature (middle), and external pressure (bottom).

Figure 41: MFC comparison of the 10 sccm MFC (top) and the 500 sccm MFC (bottom) both run for 10 hours with flow set to 10 sccm on both controllers. The 500 sccm peaks show less drift based broadening.

Figure 42: Overnight (12 hrs) drift with gas flow at 30 sccm (top), 25 sccm (middle), and 20 sccm (bottom). The optimimal flow rate is not clear.

Figure 43: Results of tracking internal pressure and centroid location over a period of 48 hours.

Figure 44: The effect of voltage change (E/P) on energy resolution for a pressure of 350 Torr.

Figure 45: Range data for alphas and fission fragments in P-10 gas at different pressures with relation to our chamber length (red line).

Figure 46: Lateral testing results starting from the detector's axial center (0 cm) showing a very slight increase in energy resolution percentage as the alphas approach the edges of the ion chamber guard ring interior diameter.

Figure 47: Normalized low-end energy measurements of before (green) and after (red) grounding straps were wrapped around the cathode preamp. RF noise was significantly decreased by wrapping grounding straps around the preamps. The cutoff below channel 10 is just an artifact of the data acquisition threshold.

Figure 48: Bragg Curve Spectroscopy results for alpha particles. This is an expanded view of the low energy section of Figure 49.

Figure 49: Bragg Curve Spectroscopy results for fission fragments and alphas, noting the horizontal scale is 10^4 keV.

Figure 50: Active cathode timing and energy data for the Tri-nuclide alpha source.

Figure 51: Active cathode timing and energy data for the ^{252}Cf and ^{239}Pu sources, full spectra shown. Due to the great difference in count rate due to alpha vs.

fission branching in ^{252}Cf, only the alphas are visible in the counts vs. energy plot.

Figure 52: Active cathode timing and energy data scaled to display alpha particle data for ^{252}Cf and ^{239}Pu.

Figure 53: Active cathode timing and energy data scaled to display ^{252}Cf fission fragment data

Figure 54: LANSCE preliminary energy measurement results.

Figure 55: Energy losses in Mylar windows based on SRIM simulations.

Figure 56: Experimental energy of tri-nuclide source without Mylar (top), with 1.5 μm Mylar (middle), and with 2.5 μm Mylar (bottom).

Figure 57: Standard Deviation (energy broadening) of 5156 keV ^{239}Pu alpha particle.

Figure 58: Energy broadening (standard deviation) of alpha particles and fission fragments based on Mylar thickness.

Figure 59: Active cathode drift time plot for alphas in P-10 gas at a pressure of 300 Torr with varying drift velocity.

Figure 60: Alpha particle experimental range data based on maximum drift velocity (v_d = 3.45 cm/μs) for alphas in P-10 gas at approximately 300 Torr.

Figure 61: Experimental range plot for ^{252}Cf fission fragments, assuming a maximum drift velocity of 3.45 cm/μs at a pressure of approximately 300 Torr.

Figure 62: Mass plot for ^{252}Cf and ^{239}Pu alphas.

Figure 63: Mass plot for fission fragments.

INDEX OF TABLES

Table 1: The recombination coefficients for various gases at STP [Brown, 1949].

Table 2: Alpha energies in keV and branching in % for sources used [BNL, 1952].

Table 3: Results of Mylar window tests without mesh backing.

Chapter 1

Introduction & Purpose

1.1 Overview

Even today, fundamental questions regarding the complex process of fission remain unanswered. Theoretical models and simulations have given a better understanding of these processes, but to achieve a more complete picture, high precision experimental data must be obtained. Measurements of fission fragment mass distributions performed over a large range of neutron-incident energies and fissioning systems will provide further insight into understanding the entire nuclear fission process.

Fission fragment distribution data has widespread applications for nuclear reactor safety and maintenance, simulations, and a better understanding of the

fundamental fission process. Applications specific to reactors include using particular fission product yields to determine the total number of fissions occurring within reactor fuel, but the particular yields must be well known. A better understanding of reactor fuel is directly related to material accounting and identification, both of which can aid in nuclear non-proliferation. Applications to simulation include verification for nuclear criticality, transmutation rates, and radiation effects and heating for fuel.

The current research is toward building, developing, and using a dual-arm fission fragment spectrometer to study binary fission. Important parameters include measurements of energy, atomic number, and mass. The spectrometer is based on the 2E-2V method [Boucheneb, 1989], where a time-of-flight (TOF) measurement is used to determine fragment velocity, followed by an ionization chamber (IC) which measures fragment energy. A simple diagram of a single velocity-energy (E-V) system is presented in Figure 1. By placing spectrometers on both sides of the target, a 2E-2V system, as in Figure 2, both fragments from binary fission may be measured simultaneously. The combination of E and V measurements allow us to extract a mass measurement, A, of the fragment. Further information on E and Z can be determined by examining details of energy loss within the IC [Tovesson, 2013]. The dual-arm spectrometer will allow

us to extract A, Z, and E of both fragments on an event-by-event basis, providing correlated data sets and uncertainties. The goal of this experiment is to keep the uncertainties at a minimum to achieve a mass resolution of less than one amu for fission fragments.

The University of New Mexico effort is part of a larger collaboration: the Spectrometer for Ion Detection in Fission Research (SPIDER) project, led by Los Alamos National Laboratory (LANL). The UNM effort is towards prototyping and testing detectors and techniques to advance the full project faster, while building an independent spectrometer, UNM-SPIDER, for independent data.

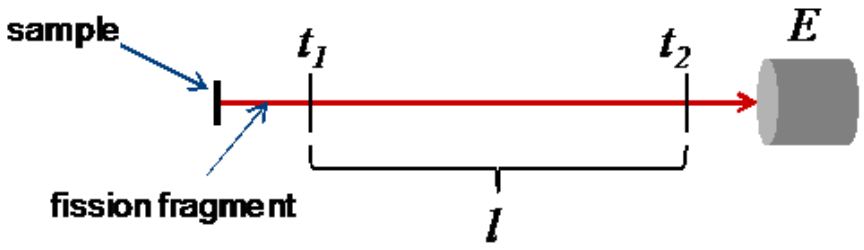


Figure 1: Schematic view of a single-arm spectrometer.

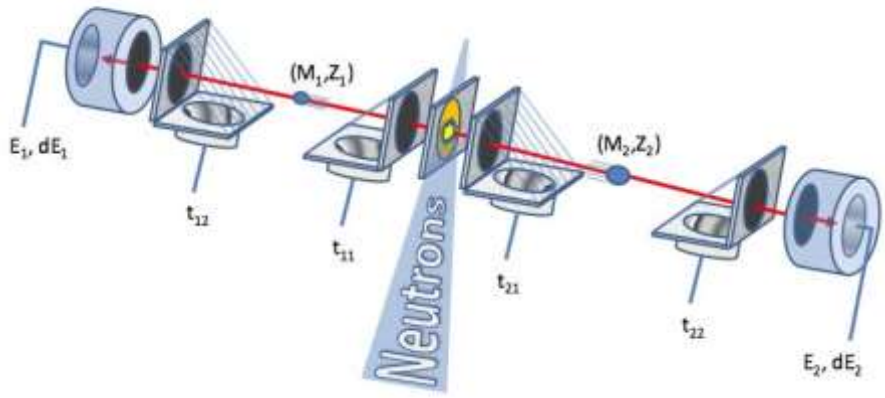


Figure 2: Proposed two arm fission fragment spectrometer configuration.

Our group at the University of New Mexico (UNM) is working in collaboration with LANL on the SPIDER project and currently designing and testing a single-arm spectrometer with different capabilities than the LANL-based spectrometer. LANL is focused on improving mass resolution while the UNM team is improving ionization chamber capabilities. The UNM spectrometer is currently a single arm E-V spectrometer. Initial measurements of the UNM spectrometer will focus on the thermal fission of ^{235}U and ^{239}Pu targets. Preliminary measurements of fission fragment velocity and energy have already been taken with fragments from low energy neutron-induced fission on a ^{235}U target at the Los Alamos Neutron Science Center (LANSCE) and future measurements are scheduled.

The purpose of this work is to build and test an active cathode ionization chamber with low uncertainty to ensure better than one amu mass resolution.

This IC is different from the previous UNM iteration due to the implementation and testing of an active cathode design. This design change allows for a powerful improvement in data by enabling us to take Z measurements. Initial tests with alpha particles and a spontaneous ^{252}Cf fission source will be used to characterize the IC to ensure a high energy resolution measurement as well as to obtain initial active cathode measurements.

The primary goal for the IC is to achieve consistent energy resolution measurements at low pressures. An energy resolution of less than 1.5% is desired for the alpha particles, implying a resolution of better than 0.47% for fission fragments, based on electron counting statistics. A more strict definition of energy resolution will be covered in later sections but can be loosely defined as being related to the width of the energy peak. The secondary goal, the active cathode for Z measurements, will also be described in depth.

1.2 Background and Prior Work

Previous fission fragment experiments have been carried out using the Cosi Fan Tutte spectrometer and have successfully measured light fragments with a resolution of 1 amu and heavy fragments with a resolution of 2-3 amu [Boucheneb, 1989]. These experiments were done with thermal neutrons incident

on a ^{229}Th target. The Cosi Fan Tutte detector had a low efficiency, making two arm coincidence measurements on an event-by-event basis difficult. The results from the Cosi Fan Tutte light fragment mass data can be seen in Figure 3, where individual masses may be resolved and Gaussian curves are fit to each peak to aid in analysis. This spectrometer was also able to collect Z data for the light fragments (>1 MeV/amu) using Bragg spectroscopy (explained later), which can be seen in Figure 4.

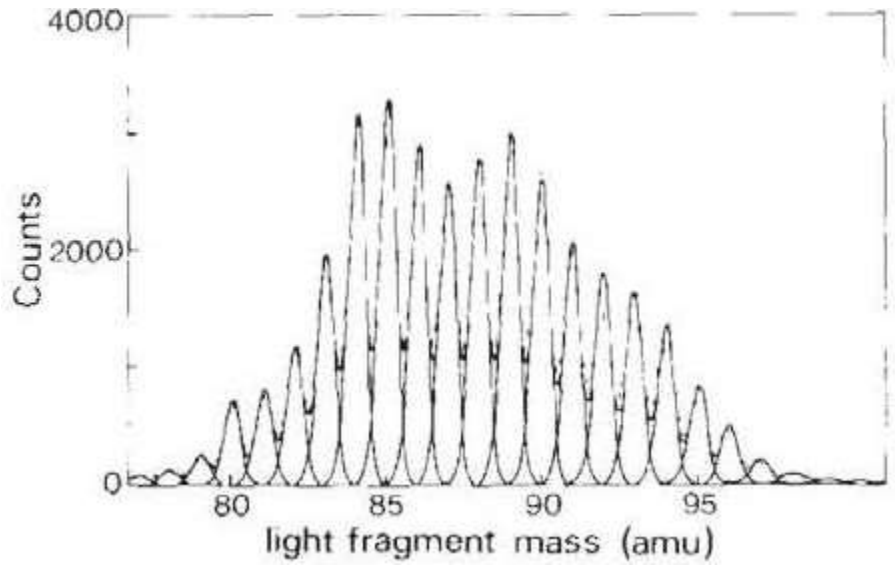


Figure 3: Light fragment mass distribution measured using the Cosi Fan Tutte Spectrometer [Boucheneb, 1989].

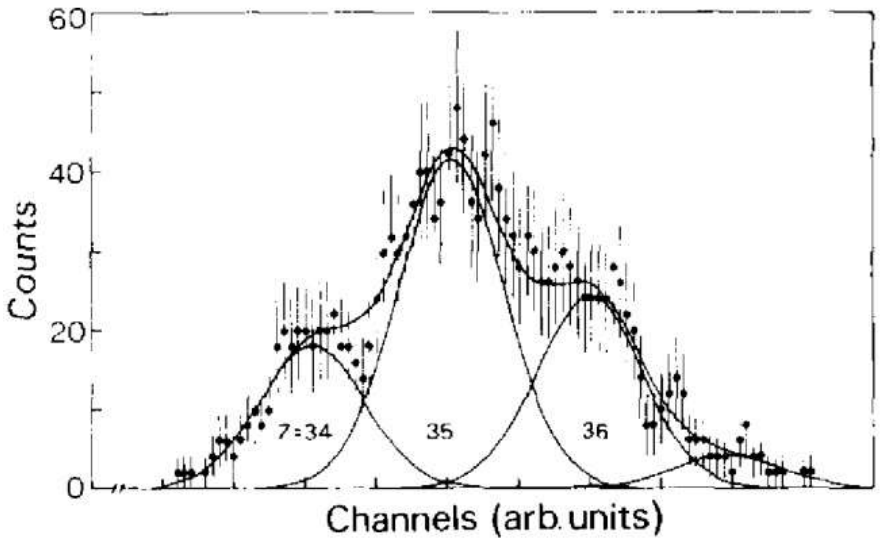


Figure 4: Nuclear charge distribution for A=87 measured using the Cosi Fan Tutte spectrometer [Boucheneb, 1989].

The Cosi Fan Tutte spectrometer was used as a primary example for development of spectrometers involved in the SPIDER collaboration. The SPIDER collaboration includes improvements in fast timing electronics, availability of the LANSCE neutron beam line, and thinner entry windows between the TOF and IC chambers to reduce energy losses and, more importantly, energy straggling that broadens resolution [Mierbachtol, 2014a; Tovesson, 2013; Arnold, 2014].

The UNM spectrometer is being constantly improved based on experimental feedback. The UNM ionization chamber used in the final spectrometer configuration presented here is the second iteration of an ionization chamber that

was previously developed at UNM by a former graduate student, Drew Mader. The previous iteration did not include the use of an active cathode for use in particle range measurements, though it did achieve a good basis for characterizing our current chamber, especially for energy response [Mader, 2103].

The current work includes a complete redesign of the ionization chamber to use an insulated cathode - not tied to the grounded vacuum chamber - that was used to implement the active cathode concept. In addition, the ionization chamber was also recently coupled to the time-of-flight detector, creating the full spectrometer for mass and energy measurements.

1.3 Organization of Thesis

Work done on this project includes the design, debugging, and testing of the active cathode ionization chamber as well as design of the thin window between the TOF and IC chambers. Chapter 2 introduces the basic fundamental theory behind the spectrometer as well as in-depth theory of the ionization chamber and its functions. Chapter 3 discusses the actual physical design of the ionization chamber and thin window, as well as the electronics used in the design. Chapter 4 provides the experimental results as well as analysis of basic experiments.

Chapter 5 is devoted to the results of data taken to demonstrate the active cathode Z determination method, as well as preliminary mass analysis results. Finally, Chapter 6 discusses the conclusions of this work and gives insight into future work and improvements.

Chapter 2

Theory

2.1 2E-2V Method

The 2E-2V Method is a method used for determining the masses of fission fragments and other particles [Arnold, 2014; Meierbachtol, 2014b; Tovesson, 2013]. A Time-of-Flight (TOF) detector is used to determine the velocity of an incoming particle, and an ionization chamber is used to determine the energy of that incoming particle. When these E-V detectors are paired back-to-back around the fission source for coincident measurements of binary fission pairs, it is called the 2E-2V method. A solid CAD model of the UNM single-arm spectrometer can be seen in Figure 5. At the front end of the TOF detector is a target chamber that holds the actinide to be bombarded by neutrons. The ionization chamber (IC) is located at the back end of the TOF detector. The fission fragment spectrometer

currently as built at UNM uses a single arm to determine the velocity and energy, and is hence a 1E-1V detector. After a fission event, binary fission fragments travel in nearly opposite directions from the fission source, such that the UNM single arm spectrometer will only record one fragment per event. Detector arms on either side of the target, an "arm pair", allow for simultaneous measurement of both fission fragments from a binary fission event. Increasing the number of detector arms also increases the angular efficiency of the detector. The final expected configuration of the LANL SPIDER spectrometer will contain a total of nine arm pairs.



Figure 5: Solid CAD model of the single arm UNM fission fragment spectrometer.

The TOF detector is held at high vacuum (10^{-7}Torr) and measures the time of flight of a particle indirectly from electrons scattered by the particle, using electrostatic mirrors, thin foils, and micro-channel plate (MCP) detectors,

together called a timing module. As seen in Figure 6, a particle passes through the thin foil, causing electrons to eject; these electrons are then affected by the potential difference from the electrostatic mirror and forced downward into the MCP. The potential change on the MCP sends out a signal that corresponds to a time-stamp. The MCP pulse has a FWHM on the order of a nanosecond, but using timing electronics (constant fraction discriminator), the timing pulse centroid can be measured to about 100 ps. The electrostatic mirrors have a small physical cross section, and the particle passes through with high efficiency and only minor perturbation from the electric field. As the particle continues along the TOF chamber, it passes through another timing module, giving out a second MCP signal corresponding to a second time. With a known distance between MCP/mirror assemblies, ΔL, and a known flight time, Δt, the velocity, v, of the particle can be determined:

$$\mathrm{v} = \frac{\Delta L}{\Delta t} \qquad \text{[Eq. 1]}$$

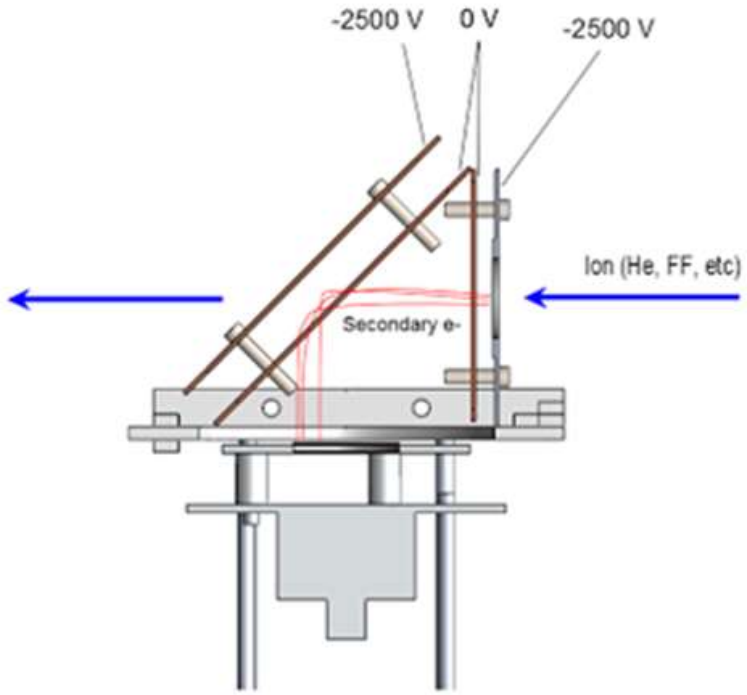


Figure 6: Illustration of the timing module, with carbon foil at right, electrostatic mirror at left, and MCP at bottom.

The energy, E, of the particle is measured by the ionization chamber, which will be discussed much more in depth. With the measurements of time (t), length (L), and energy (E), the mass (m) of the particle can be determined by rearranging the classical kinetic energy expression as follows,

$$\mathrm{m} = 2\mathrm{E}\left(\frac{\Delta t}{\Delta L}\right)^2 \qquad \text{[Eq. 2]}$$

The main task in collaboration with the SPIDER project is to achieve a mass uncertainty (∂m) of less than one amu. The equation for this uncertainty can be found through use of a squared total differential from Equation 2,

$$(\partial m)^2 = \left(\frac{dm}{dE}\partial E\right)^2 + \left(\frac{2dm}{dl}\partial L\right)^2 + \left(\frac{2dm}{dt}\partial t\right)^2 \qquad \text{[Eq. 3]}$$

Carrying out the differentiation in Equation 3, we arrive at the following uncertainty in mass,

$$\frac{\partial m}{m} = \sqrt{\left(\frac{\partial E}{E}\right)^2 + \left(\frac{2\partial L}{L}\right)^2 + \left(\frac{2\partial t}{t}\right)^2} \qquad \text{[Eq. 4]}$$

The relative uncertainty in length, ∂L/L, is much lower than any other quantity in Equation 4, and can be determined directly through alpha particle calibrations [Blakeley, 2013]. The uncertainties in energy, ∂E, and time, ∂t, are determined based on the FWHM for each measurement. Currently the energy uncertainty dominates the final mass uncertainty, so this is where most experimental effort is focused.

2.2 Time of Flight

The time-of-flight detector uses thin foils, electrostatic mirrors, and micro-channel plates to take timing measurements. The thin foils are made of 100 μg/cm^2 thick carbon, chosen to minimize the attenuation of the passing particle, and hence minimize the energy loss. Thinner foils may be used once timing straggling becomes the limiting factor in mass measurements, but the current thickness is much less prone to breaking. As the particle passes through the

carbon foil, secondary electrons are produced isotropically and emitted from the front and back of the foil. Some of these, depending on geometry, are reflected from electrostatic mirrors towards the microchannel plate electron detectors. The electrostatic mirrors consist of copper faced FR4 plastic frames with gold-plated tungsten wire grid patterns, seen in Figure 7.

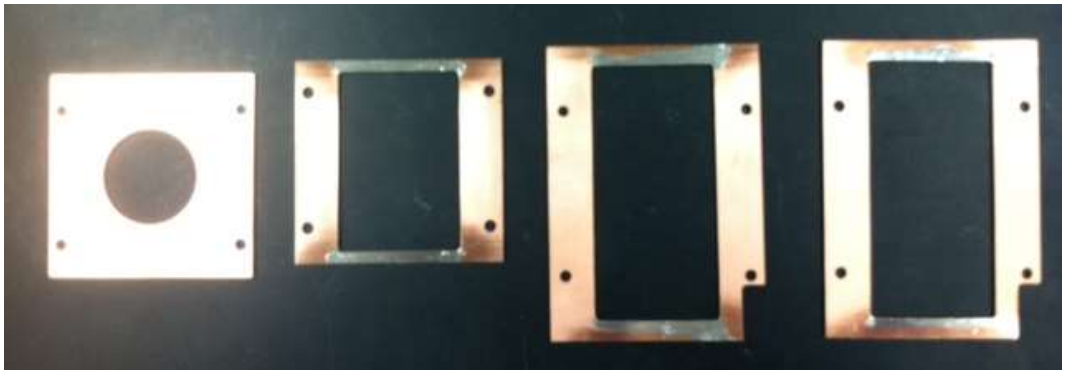


Figure 7: Photograph of the copper faced FR4 plastic mirror frames.

A 3-D solid CAD model of the mirror assembly can be seen in Figure 8. As seen in Figure 9, there are several different electric potential regions. The ejected electrons are first accelerated from the foil towards an acceleration grid to bring them all to about the same kinetic energy, to reduce travel time and thus improve timing resolution, and to bias their direction towards the mirror. Past the acceleration grid they enter a field-free region and then pass a diagonal grid to enter the reflection region where they experience the repulsion from a second

diagonal grid. Those reflected electrons pass through the first diagonal grid, reentering the field free region, where they continue on to impact on the MCP detector face, producing a time stamp. Comparing the timing between two detector modules for a given energy of alpha particles, the FWHM for the TOF timing is currently reported to be 400 ps [Blakeley, 2013].

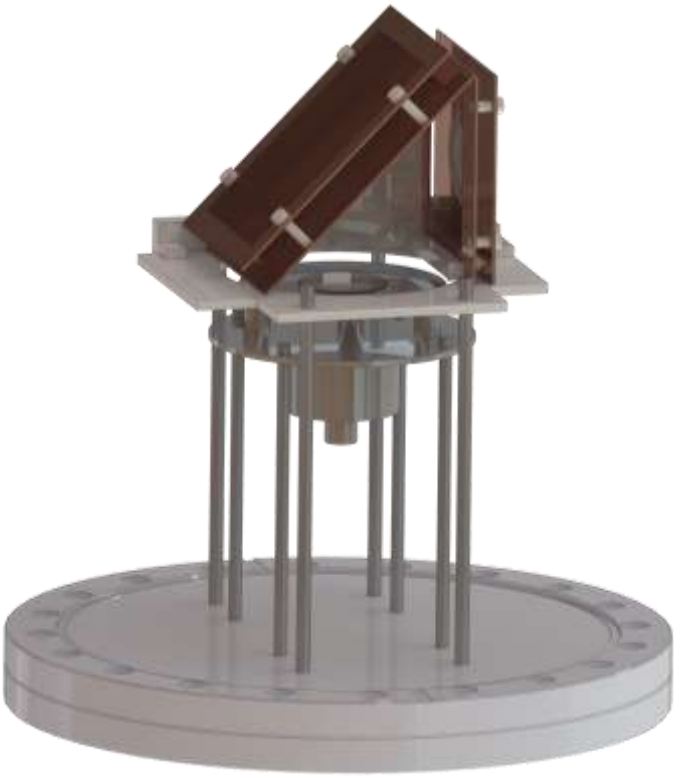


Figure 8: Solid CAD model of the TOF mirror assembly.

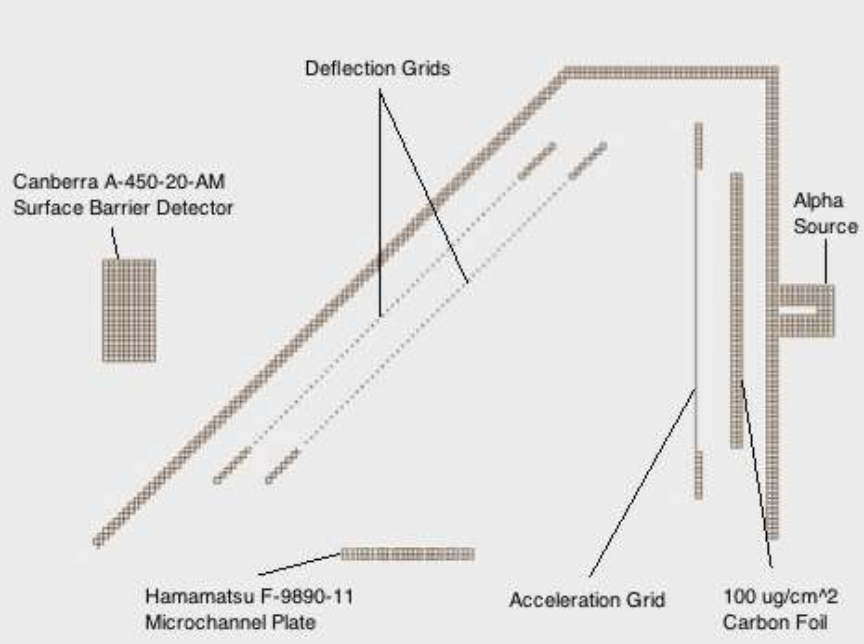


Figure 9: Electrode grid geometry of the electrostatic mirror [Blakeley, 2013].

2.3 Ionization Chamber

2.3.1 Characteristics

Several previous experiments involving 2E-2V spectrometers used solid state surface barrier detectors (e.g., [Kozulin, 2008]), though these showed an increased uncertainty in regards to energy measurements of heavy ions, specifically fission fragments. The advantages of ionization chambers, are that they are simple to construct and can be made to be any shape or size, have a relatively small pulse-height defect and low sensitivities to backgrounds of photon and neutrons, and by cycling gas through show a low level of degradation due to radiation damage [Sanami, 2008]. Our spectrometer uses an

ionization chamber not only due to a lower uncertainty, but also due to a larger solid angle as well as the possibility of using the IC as a time-projection chamber where the depth of penetration of the ion may be used for understanding its atomic number. Penetration depth is not discernible in surface barrier detectors. IC use as a time-projection chamber will be explained in depth later in this discussion.

An ionization chamber (IC) consists of an anode spaced apart from a cathode, and an ionization gas all within a closed chamber. As a particle travels in an IC, it interacts with gas molecules, causing the gas to ionize. As a particle ionizes between electrodes, an area termed the active region, the applied electric field acts upon the resulting ions and free electrons formed in the gas. Due to the electric field, free electrons drift towards the anode of the IC, whereas ions drift towards the cathode. The anode and cathode act as a capacitor and hence have an initial capacitance. The movement of positive or negative charges towards an electrode causes an induced potential difference which gives rise to a transient current in the external circuit. This can be understood in terms of the changing energy of the system through the change in capacitance between the electrodes due to the motion of the charges within. Thus the voltage induced on the electrodes is a function of the number and velocity of the free charges within.

Knoll expresses this mathematically through conservation of energy as [Knoll, 2000]:

$$\frac{1}{2}CV_0{}^2 = n_0eEv^+t + n_0eEv^-t + \frac{1}{2}CV_{ch}{}^2 \qquad \text{[Eq. 5]}$$

The term on the left represents the original stored energy, the first term on the right represents the energy absorbed by moving ions, the second term on the right represents the energy absorbed by moving electrons, and the last term on the right represents the remaining stored energy. The signal voltage, V_R, is based on the difference between the initial voltage, V_0, and the remaining stored energy voltage, V_{ch}. Based on this, Equation 5 reduces to a readable voltage from the induced current:

$$V_R = \frac{n_0e}{dC}(v^+ + v^-)t \qquad \text{[Eq. 6]}$$

where the ion velocity v+ is typically several orders of magnitude smaller than the electron velocity v-, n_0 is the number of original ion pairs, e is the electronic charge per ion, C is the capacitance of the IC, E is the electric field between cathode and anode, and d is the distance from cathode to anode.

The time integral of the transient current from charged particle movement produces a charge pulse or voltage pulse on each electrode [Sharma, 2006]. Electrons typically move many times more quickly than ions (approximately 1000x in the P-10 gas used in our work), and so the induced pulse is considered

to be from electron motion. When an IC is operated in pulse mode, the magnitude of the signal pulse is proportional to the energy of the incoming particle [Knoll, 2000], the alpha or fission fragment in our case.

Though an ionization chamber can be perceivably built to any shape, several types of common and tested geometries already exist. The most common types of IC geometry include transverse (Figure 10), coaxial, and axial (Figure 11) designs. The axial design, which is the design used for this experiment, consists of an electric field parallel to the particle track direction; the particle enters through a hole in the cathode then travels down towards the solid anode.

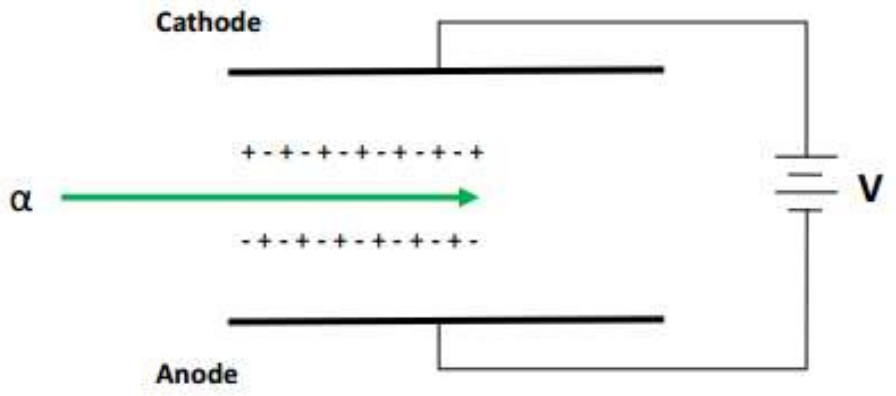


Figure 10: Basic design of a transverse ionization chamber [Mader, 2013].

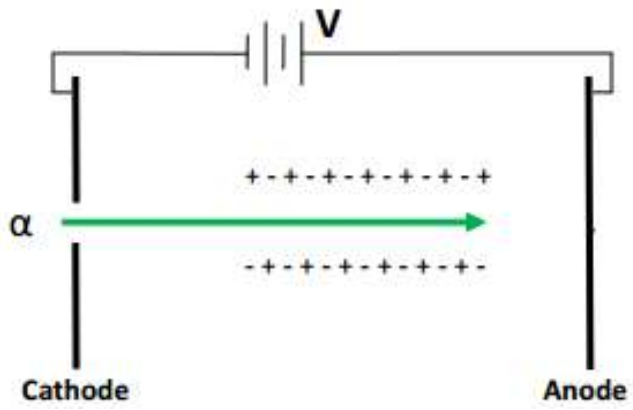


Figure 11: Basic design of an axial ionization chamber [based on Knoll, 2000].

Ionization occurring along the particle track is called primary ionization. After the electrons and ions are freed within the gas, they are free to interact inside of the gas and recombination may occur. An applied electric field is used to move them towards opposite electrodes, both increasing induced current and reducing recombination. This is the basis of proportional gas detectors. However, when the electric field (voltage difference) between the anode and cathode is increased enough, electrons and ions can gain more energy and ionize more of the gas within the detector; this is called secondary ionization which produces charge multiplication, and is not considered here. Secondary ionization is a mechanism that is not ideal for operating ionization chambers. Ionization chambers rely on collecting the signals induced by primary ionizations. As such, ionization chambers operate in a region called the saturation region and do not rely on charge multiplication.

When discussing gas detectors, it is important to discuss the plot of pulse height vs. voltage for a given energy event, Figure 12. The physics behind ion interactions will be discussed later in Section 2.5, but in regions of low operating voltage, the induced electric field is insufficient to prevent recombination of the original electron-ion pairs, and hence a small signal pulse, or ionization current, is seen for that operating voltage. As the electric field is increased, recombination is greatly reduced and nearly the full ionization in the gas is collected. This is called the saturation region, where charge collection is insensitive to small changes in voltage, and this is where our IC operates. As the voltage is increased further, secondary ionization occurs and charge multiplication begins to occur, thus causing the ionization current to increase with the voltage: this is called the proportional region. The proportional region is named as such because the pulse amplitude is proportional to the number of original electron-ion pairs formed in initial ionization, though also dependent on small changes in applied voltage. As the voltage is increased still further, the pulse amplitude experiences non-linear effects due to space charge and hence the region of the graph becomes the limited proportional region. Finally, space charge effects begin to dominate the electric field as the voltage is increased still further into the Geiger-Mueller region of the graph.

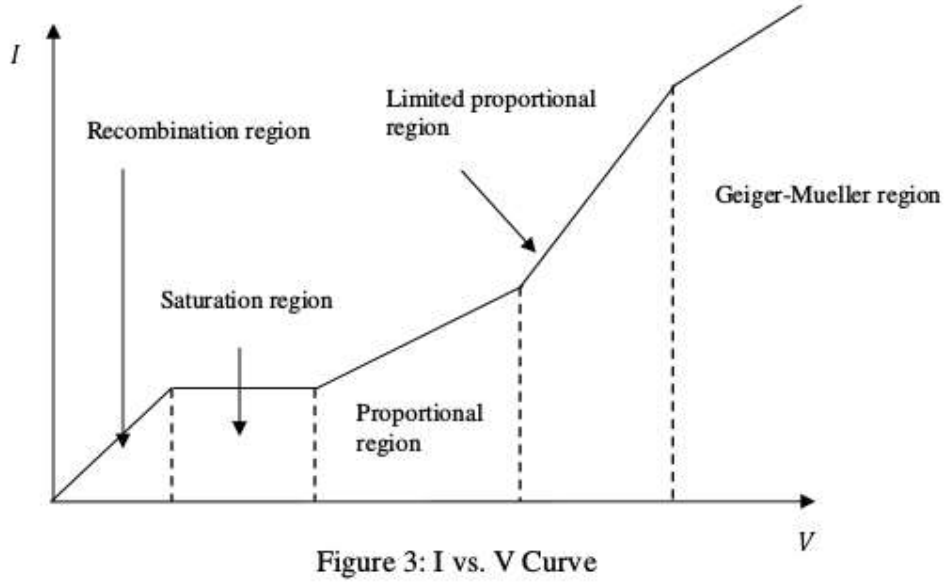


Figure 12: Pulse height vs. V curve for a gas detector [Knoll, 2000].

An advantage of ICs operating in the saturation region is that fluctuations in the power supply have little effect on the magnitude of the output pulse, though the field does affect the electron drift velocity as will be discussed. Without charge multiplication occurring, the ionization gas also degrades less quickly [Mader, 2013].

2.3.1 Energy Resolution

How well the IC can resolve the energies of different particles is pivotal to the overall mass resolution of the spectrometer. The energy resolution (ER) of the IC is defined by Equation 7:

$$ER = \frac{FWHM\ (H_o)}{H_o} \qquad \text{[Eq. 7]}$$

where the full width at half maximum (FWHM) and location of the peak centroid H_o are illustrated in Figure 13.

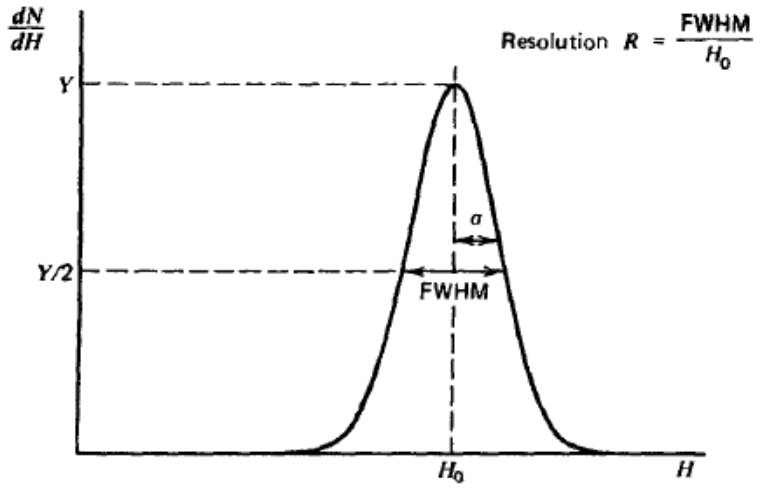


Figure 13: Definition of detector resolution, from [Knoll, 2000]. For peaks whose shape is Gaussian with standard deviation σ, the FWHM is 2.35σ.

The FWHM (for Gaussian shaped peaks) is defined theoretically by [Knoll, 2000]:

$$FWHM = 2.35\sqrt{fWn_o} = 2.35\sigma \qquad \text{[Eq. 8]}$$

where σ is the standard deviation, W is the energy per ion pair produced (known as the *W-value)*, n_o represents the mean total number of electron-ion pairs formed, and *f* is known as the *Fano factor* and will be discussed.

When a particle ionizes in a gas it creates an electron-ion pair. As it does so it must transfer at minimum an amount of energy equal to the ionization energy of the gas to complete the ionization process. The minimum energy to ionize the gas is lower than the average energy deposited in the gas per ion pair produced. The average energy lost by the incident particle per electron-ion pair formed, the W-value, accounts for energy lost to excitations such as vibrations, etc. The W-value is dependent upon the type of fill gas, incoming particle type, and energy of the particle. Typically, W-values for alpha particles are from 20-40 eV/pair. The average total number of electron-ion pairs formed, n_o, is then proportional to the W-value, assuming that the W-value remains constant.

The total number of electron-ion pairs formed is dependent on the incoming particle energy and the W-value, meaning it is then also dependent upon the type of incoming particle and the fill gas. The value of n_o is defined by the following:

$$n_o = \frac{E_o}{W} \qquad \text{[Eq. 9]}$$

where E_o is defined as the incoming particle's initial energy. Measurements of the ionization process have been done extensively, and as such, the value of n_o is shown to be governed by Poisson statistics. The Fano factor, *f*, is an empirical coefficient used to account for the observed variance in expected vs. measured

values of n_o and has been discussed in detail by several references [Knoll, 2000; Mader, 2013].

A theoretical limit exists for the energy resolution of the ionization chamber. Substituting in the definitions of FHWM from Equation 8 and n_o from Equation 9, the energy resolution takes on the following form:

$$ER = \frac{2.35\sqrt{fWn_o}}{E_o} = \frac{2.35\sqrt{f}}{\sqrt{Wn_o}} \qquad \text{[Eq. 10]}$$

This represents the theoretical minimum for obtainable energy resolution, based on counting statistics. For example, for a 5.5 MeV alpha particle in P-10 gas (90% Argon, 10% Methane) the theoretical energy resolution minimum is near 0.47% [Mader, 2013]. Measurements near this have used cooled electronics and other methods to reduce other noise contributions. For higher energy particles such as fission fragments, with near 100 MeV of energy, the number of electrons liberated is on the order of 20 times larger. Thus, based solely on counting statistics, resolution should improve by the square root of 20, or better than 4 times. Various other experiments have been performed with ionization chambers to improve energy resolution for both alpha particles and fission fragments and as such, a goal of 0.47% ER for heavy fission fragments is reasonable [Oed, 1984; Mader, 2013; Bocquet, 1988; Boucheneb, 1989]. The previous iteration of an ionization chamber characterized by Mader showed consistent energy resolution

measurements for 5.5 keV alpha particles at around 1.5% [Mader, 2013]. Extrapolating this based on Equation 10 indicates that the goal for heavy fission fragments of 0.47% (or about 1/4 of 1.5%) is reasonable. Experiments by Oed have found energy resolution of 0.41% and 0.73% for light and heavy fission fragments, respectively [Oed, 1984].

2.4 Charge Mobility

When a particle ionizes in a gas with an applied electric field, the resulting ions and free electrons reach a terminal velocity. This terminal velocity, the drift velocity, is characteristic of the E field and the gas the ions and electrons are interacting with. Ions and electrons have different charge mobilities within a gas that contribute to their respective drift velocities. The drift velocity of a charge carrier within a gas can be described by the following,

$$v_d = \frac{\mu E}{P} \qquad \text{[Eq. 11]}$$

where v_d is the drift velocity, μ is the charge mobility, E is the applied electric field, and P is the pressure of the gas. The charge mobility, μ, is characteristic of the molecular structure of the gas. Free electrons have a high mobility and have a drift velocity on the order of a cm/μs. For ions, the drift velocity is on the order of a cm/ms, meaning that ions have a relatively low mobility. This difference is due to electrons having a much lower mass than that of ions, allowing them a greater

acceleration [Knoll, 2000]. For this reason the induced pulse from electrons in P-10 gas is much faster than that of ions, microseconds vs. milliseconds, and only the electron-induced pulse is usable. This was confirmed in extensive experiments performed by Sharma and Khryachkov. For P-10 gas at an E/P of 0.2 V/cmTorr the electron drift velocity is approximately 3.5 cm/μs [Khryachkov, 2003], whereas the ion drift velocity at the same E/P is approximately 54cm/ms [Sharma, 2006], > 10,000 times slower. As the ion pulse spreads over a much longer time than the electron pulse, and thus effectively buried in the system noise, we focus entirely on the electron induced pulse in this work.

Knoll suggests that for hydrocarbons and argon-hydrocarbon mixtures, the drift velocity for electrons reaches a maximum or saturation point over a range of E/P values. Indeed, if the electron drift velocity is plotted versus the reduced electric field, E/P, then a maximum does exist. This maximum drift velocity can be seen for P-10 gas in Figure 14. Khryachkov et al. explain in detail the experimental process for determining the drift velocity of electrons in an argon-methane gas mixture and introduce an empirical formula for determining the drift velocity [Khryachkov, 2003] based on E/P values and percentage of argon. Other examples of this saturation effect on argon-hydrocarbon mixtures can be found in references [Knoll, 2000 & Sharma, 2008]. It is possible that the reduction in

velocity above a certain field strength may be due to electron energy loss via secondary ionization such as seen in the classic Franck-Hertz experiment, moving the detector into the proportional counter regime, but this is not addressed in detail in the references. This, though, would explain the different E/P for the maxima in different gasses.

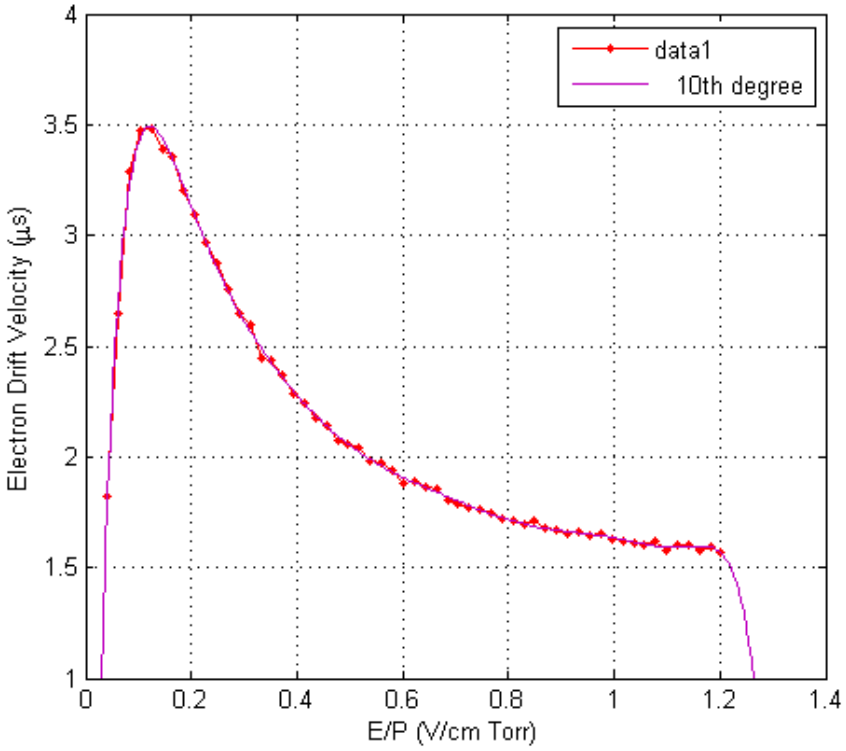


Figure 14: E/P vs. electron drift velocity curve for P-10 gas as calculated based on empirical equations from Khryachkov et al. [Khryachkov, 2003].

Knoll also offers that for other gases, such as isobutane (C_4H_{10}) in Figure 15, there exists no clear saturation point and instead the drift velocity increases with increasing reduced electric field.

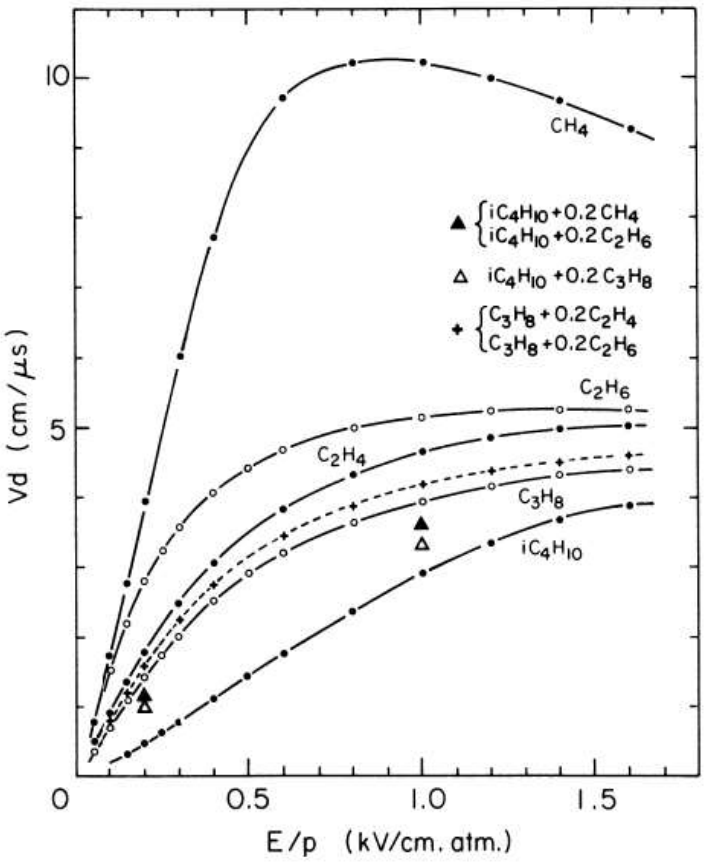


Fig. 185 Lehraus et al. (1982)

Figure 15: E/P vs. electron drift velocity for isobutane gas [Peisert, 1984].

The motion of the charge in the IC induces the pulse read out, which is scaled to determine the energy deposited in the IC. To maintain a uniform response of the detector to the same incident radiation, that is to be able to calibrate the pulses

from the ionization chamber and relate them to particular energies, it is important to keep the electron drift velocity stable. The drift velocity is highly dependent upon the pressure, temperature, and purity of the gas, as suggested by Sharma [Sharma, 2006]. As such, to keep a relatively consistent drift velocity, it is ideal to operate an ionization chamber where v_d is less sensitive to other changing parameters. In relation to P-10 gas, this would be when v_d is at a point of minimum slope with respect to reduced electric field, E/P, either at the maximum value of v_d or at a very high value of E/P where the slope begins to level off. This makes the drift velocity less variable with small fluctuations in voltage and pressure. As the induced signal depends on the drift velocity, this is extremely important for stability of the response of the system.

2.5 Ion Interactions

Rigorous treatment of the theory of ion interactions within gas detectors has been summarized in the various references quoted [Mader, 2013; Knoll, 2000], here it is very simply reminded without mathematical detail. Various interactions can occur within the detector that can affect the ion and free electron motion, and therefore affect the signal from the detector. Four interactions occur in relation to the electrons within the detector, two of which are more significant in ionization chambers: electron capture and recombination. The other two interactions are

intrinsic to all gas counting detectors: diffusion and space charge. These are discussed below.

Electron capture, also known as charge transfer, occurs when a neutral gas molecule experiences a collision with a free electron, resulting in the ion acquiring a free electron. In relation to ionization detectors, one of the free signal electrons that was a result of the initial ionization may be captured by a neutral gas molecule, thereby not being collected at the anode and contributing to a signal pulse. The electron capture process is time dependent and can have its effects minimized by decreasing the amount of time for the electrons to be collected at the anode. To decrease collection time, the drift velocity of the electrons should be as high as possible. However, impurities in the counting gas can have negative effects on the drift velocity of the gas and thus cause more electron capture to occur, decreasing the output signal. To minimize electron capture and maximize the signal output, the counting gas should be free of impurities and the electric field and pressure should be chosen to maximize the electron drift velocity.

In gas detectors, there exist two types of recombination: initial and volume. Recombination occurs when a free electron and a positive ion combine to form a

neutral gas molecule. Initial recombination, also known as columnar recombination, occurs when an electron and ion from the same ionizing event recombine along the particle track. High linear energy transfer (LET) particles deposit their energy in very short distances, and as such electrons and ions are ionized close together, increasing their probability for recombination. Alpha particles and fission fragments are both high LET particles, and as such ionization chambers are highly susceptible to the effects of initial recombination, leading to a pulse height readout not representing the full initial ionization - a pulse height defect. The greater LET for heavy fragments versus lighter fragments also contributes to a greater pulse height defect for heavy fragments that must be accounted for. Volume recombination occurs when a free electron and an ion from different events combine, usually further away from the initial particle track. Knoll suggests that a higher applied electric field can contribute to minimizing recombination [Knoll, 2000].

The general equation for recombination [Mader, 2013] is dependent on a gas parameter called the recombination coefficient (α), which is dependent on the molecular structure of the counting gas. From Table 1, one can see that Argon has a very low value of α, whereas air, hydrogen, and helium have higher values of α. The lower value of α corresponds with a smaller probability that the ions

and electrons will recombine, meaning that the more pure the gas, the less chances of recombination and the greater probability of a fully collected signal. Summarizing, a high electric field combined with a pure gas quality will minimize recombination.

Gas	α (cm^3/s)
He	6.8×10^{-9}
Ar	6.8×10^{-11}
Air	1.7×10^{-7}
H_2	1.6×10^{-7}

Table 1: The recombination coefficients for various gases at STP [Brown, 1949].

Electrons and ions naturally diffuse and experience many collisions with gas molecules, and may leave the active region of a detector instead of collecting at the electrodes. The diffusion of gas molecules within the presence of an electric field is again dependent on the molecular structure of the counting gas. To combat diffusion of electrons to outside the collection region, a higher electric field to move electrons to the anode can be used along with increased spatial dimensions.

Electrons travel with a higher velocity than that of their ion partners, such that the electrons will be collected by the anode sooner than the ions. As the ions drift

very slowly through the detector, they may build up in the volume of the detector over several radiation events, affecting the electric field experienced within the detector volume due to Columbic forces. These slow moving ions may be referred to as "space charge". These may thus affect the free, fast-moving electrons. For low activity sources, meaning low rates of incoming particles, the distortion in the electric field can be considered approximately the same for all events and shouldn't have a significant effect on signal collection. The charge collection time for ions in P-10 gas for the detector size and fields used is on the order of milliseconds, whereas the counts per second of standard lab check sources is around 2-5 counts per second, so we wouldn't expect many ions within the detector at the same time, just from single radiation events. We thus expect space charge to not be a factor. In addition, while space charge has a large effect in central electrode wire detectors, strongly shielding the central region when slow moving ions build up near it; in the parallel plate IC system used this is a much more minimal effect.

2.6 Particle Charge and Range

Two methods to use the ionization chamber to extract information on the charge of the incident particle were considered in this work: these are Bragg curve spectroscopy and active cathode range determination. Both approaches are based

on the influence of the specific particle charge on the energy loss rate, -dE/dx, and thus the particle range.

2.6.1 Bragg Curve Spectroscopy

The specific energy loss, -dE/dx, of a charged particle in a given medium can be characterized by the Bragg curve (Figure 16). This is described in detail in the Bethe formula [Turner, 2007] as follows:

$$-\frac{dE}{dx} = \frac{4\pi}{m_e c^2}\frac{nZ^2}{\beta^2}\left(\frac{e^2}{4\pi\varepsilon_o}\right)^2\left[ln\left(\frac{2m_e c^2\beta^2}{\mathrm{I}(1-\beta^2)}\right) - \beta^2\right] \qquad \text{[Eq. 12]}$$

where m_e is rest mass of an electron, n is electron density of the material, Z is the particle's charge, c is speed of light in vacuum, β is ratio of the particle's velocity to the speed of light, e is the elementary charge, ε_o is the vacuum permittivity, and I is the mean excitation potential of the material.

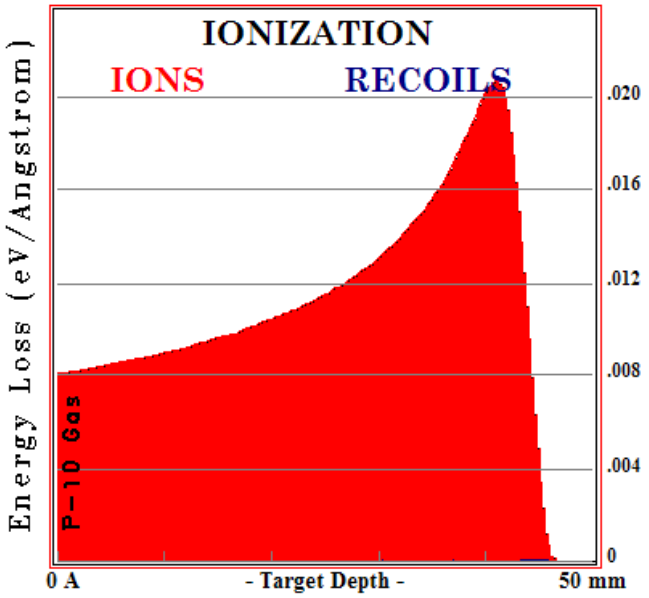


Figure 16: Bragg curve as simulated using SRIM [Ziegler, 2014] for a ^{239}Pu alpha particle in P-10 gas.

As a charged particle slows in a medium, the specific energy loss, -dE/dx, slowly increases, leading to the formation of the Bragg Peak near the end of the path. For a given target material, the amplitude of the Bragg Peak is not a function of mass or initial energy of the incident particle, but is a function of particle charge, which is dependent on the particle atomic number (Z). By examining the Bragg curve peak height, Z information may be extracted [Barna, 2004; Gruhn, 1982]; this is called Bragg curve spectroscopy. Previous SRIM simulations were performed by Mader to confirm the Bragg peak characteristics of alpha particles. The results of these simulations can be seen in Figure 17 and show that the alpha

particles have the same peak heights as well as similar Bragg curve shapes [Mader, 2013].

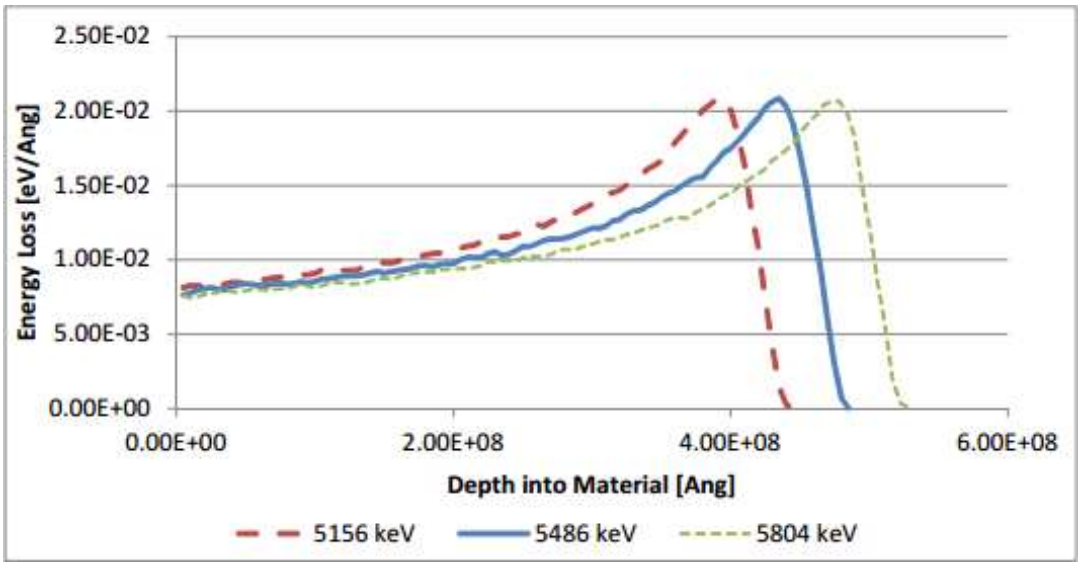


Figure 17: The Bragg curve for three different energy alphas [Mader, 2013].

The UNM ionization chamber UNM ionization chamber may be used to examine the Bragg curve for appropriate particles and energies. It is a parallel plate chamber design with a cathode at one end and an anode at the other end, and a Frisch grid (FG) in between close to the anode. Specifics of the design will be explained in Chapter 3, though it is important to explain how the design works in regards to Bragg curve spectroscopy and active cathode measurements. The design of the chamber includes guard rings that are spaced evenly between the Frisch-grid and cathode region of the chamber. These guard rings are connected

by resistors for a smooth drop in potential along the chamber length and allow for a uniform electric field to exist between the FG and cathode. In this region, the "active region" between the cathode and the FG, the particle enters and ionizes the gas. The electric field imposed within this region causes a fairly parallel electron trajectory and a constant drift velocity of electrons towards the FG and then anode. The freed electron density in the cathode-to-Frisch-grid region spatially follows the Bragg curve. Figure 18 shows the results of a SIMION simulation [Mader, 2013] with a SRIM alpha particle simulation [Zeigler, 2014] superimposed on top to give a visual representation of equipotential lines and incident alpha particles within the detector. In the applied field within the parallel field IC, the electron distribution drifts towards the Frisch grid preserving the spatial distribution. Hence the peak of the Bragg curve passes into the Frisch grid-to-anode region first and a fast pulse is induced on the anode from the Bragg peak [Sanami, 2008; Sanami, 2009]. The full distribution crosses into this region over a longer time period and so over a longer time period the full distribution induces an anode signal.

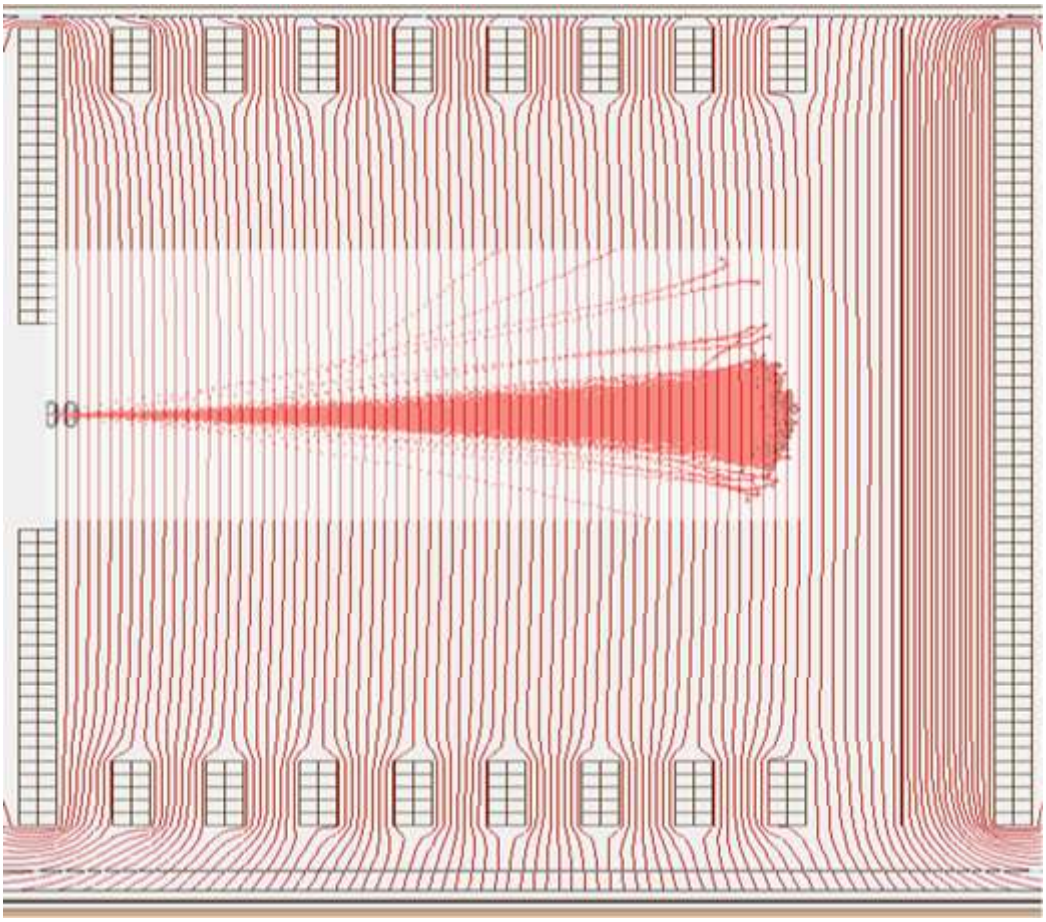


Figure 18: SRIM alpha particle [Zeigler, 2014] simulation superimposed onto a SIMION electric field simulation result [Mader, 2013]. The cathode is on the left, Frisch grid on the right, and anode on the far right.

In application, the Bragg Peak height is determined based on the pulse height induced on the anode, which can be read through an amplifier with a fast integration time, while the full energy signal can be read through an amplifier with a slower integration time. Bragg Peak results from Hagiwara can be seen in Figure 19 with different ion species [Hagiwara, 2008], and are useful for fast particles (> 1 MeV/amu). The height of the Bragg peak can be used to distinguish

between different ion species; for our applications we characterized alpha particles and light fission fragments (> 1 MeV/amu). Below 1 MeV/amu the Bragg peak is not present in the ionization distribution, so a different method using an active cathode will be discussed, which works for both heavy and light fission fragments.

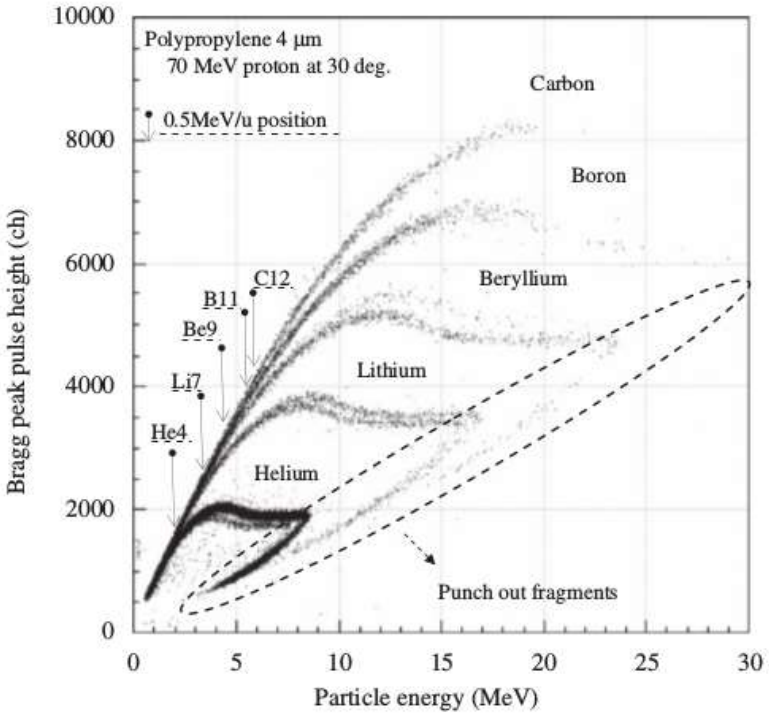


Figure 19: The Bragg peak vs. deposited energy for particles of different mass and atomic charge [Sanami, 2008].

The typical Bragg curve for a light fission fragment in P-10 gas as generated by SRIM [Ziegler, 2014] can be seen in Figure 20; the peak of the curve is present, making charge identification possible. However, for heavy fission fragments (< 1

MeV/amu), the Bragg peak is lower than the initial energy track and charge identification becomes difficult. Figure 21 shows the Bragg curve for a heavy fission fragment in P-10 gas, where the Bragg Peak is unidentifiable. A different approach must be used for heavy fragments.

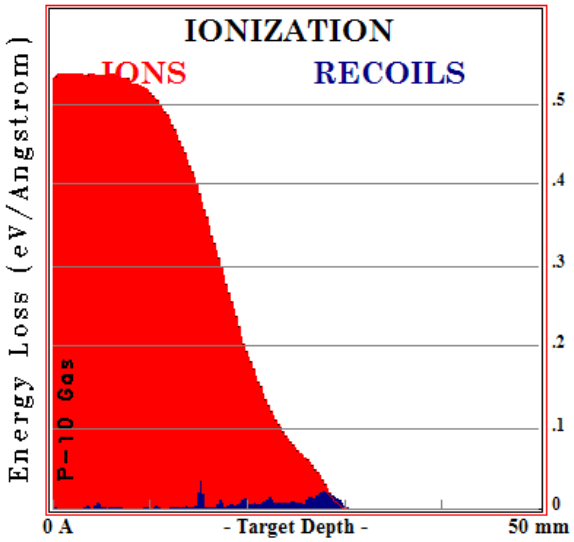


Figure 20: Bragg curve for a light (> 1 MeV/amu) fission fragment in P-10 gas.

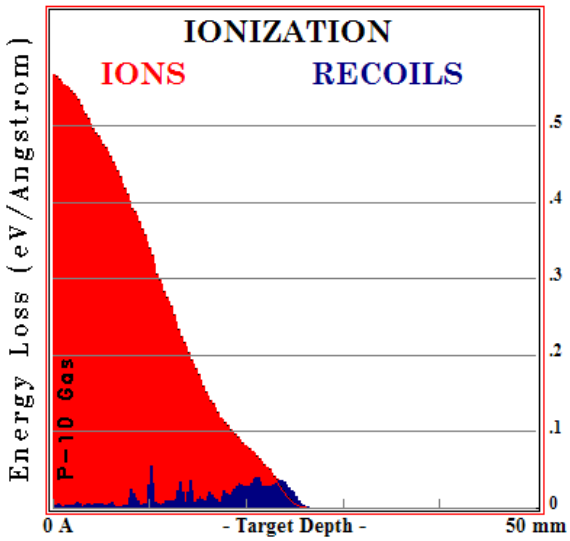


Figure 21: Bragg curve for a heavy (< 1 MeV/amu) fission fragment in P-10 gas.

It is worth noting that when binary fission fragments are both identified, the charge determination of the lighter fragment will then identify the heavier fragment, following charge conservation. Simulations from Tovesson have concluded that a charge resolution of approximately Z=1 should be sufficient for light fragment, and thus heavy fragment, identification. This charge resolution has also been confirmed to be possible to obtain based on simulations [Tovesson, 2013]. Nevertheless, direct identification of both fragment charge will further reduce uncertainties and can also be used as an important check on results.

2.6.2 Active Cathode

An alternative method for determining the charge is by examining the range of penetration of the particle in the gas. This also follows the Bethe equation, integrating energy loss per distance -dE/dx to zero energy. To extract range, timing an active cathode may be used; the active cathode method employed by Sanami et al. [Sanami, 2008] uses a time of flight measurement of the electrons within the ionization chamber itself and the electron drift velocity to indirectly determine a particle's range. Using this method we can determine the range of heavy fission fragments (< 1 MeV/amu) that do not have easily distinguished Bragg peaks. The stopping is based on the charge state of the atom, rather than just on the nuclear charge and, especially near the end of the trajectory, there is a great deal of charge exchange, making calculations extremely difficult. Tyukavkin et al. [Tyukavkin, 2009] found that the specific nuclides were still discernible and, when plotted with energy vs. velocity, the data were distinct for different atomic numbers.

The mechanics of finding the particle range in the ionization chamber depend on the time difference of the induced pulses on the anode and cathode. We can record the induced pulse on the cathode at a time t_1, followed shortly by the induced pulse on the anode at a time t_2. Based on the E/P value and type of gas,

we can calculate the value of the drift velocity of the liberated electrons. The incident particle ionizes gas and almost immediately induces a pulse in the cathode from the electron drift. The further the incident particle penetrates the gas and ionizes electrons, the faster those electrons will then pass the Frisch grid and induce a pulse on the anode. The timing difference between the cathode and anode thus allows us to then calculate a particle range. Figure 22 from Sanami et al. [Sanami, 2008] shows the fragment trajectory and distances for an incoming particle in an active cathode ionization chamber.

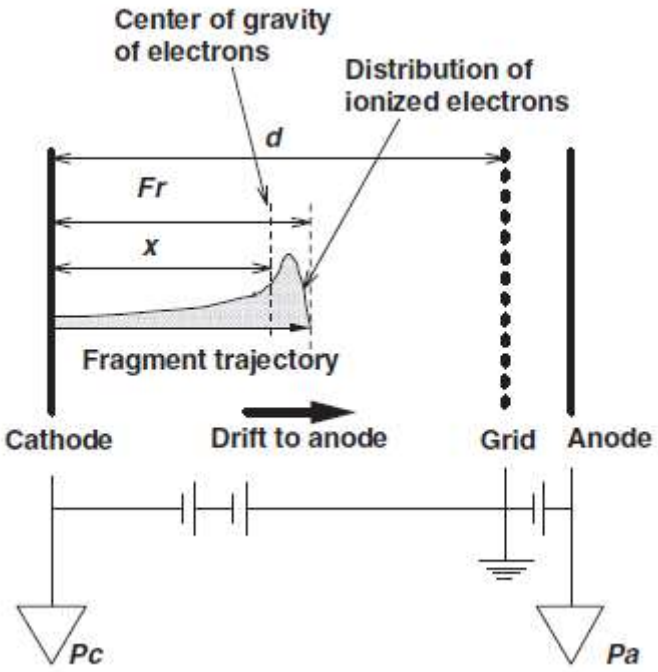


Figure 22: Schematic diagram of a Bragg curve counter; d is the cathode-grid distance, Fr is the particle range, and x is the distance from the cathode to the center of gravity of the charge [Sanami, 2008].

The drift distance that the electron front travels in the drift time is the length of the cathode to Frisch grid active area, d, minus the particle range length, Fr. Again these values are defined in Figure 22. The particle range can be calculated based on the following equation:

$$Fr = d - v_d(t_2 - t_1) \qquad \text{[Eq. 13]}$$

The anode and cathode timing signals are determined from the rise of the induced signal using charge-sensitive pre-amplifiers. Figure 23 shows the anode and cathode signal pulses from Sanami's experiments [Sanami, 2008].

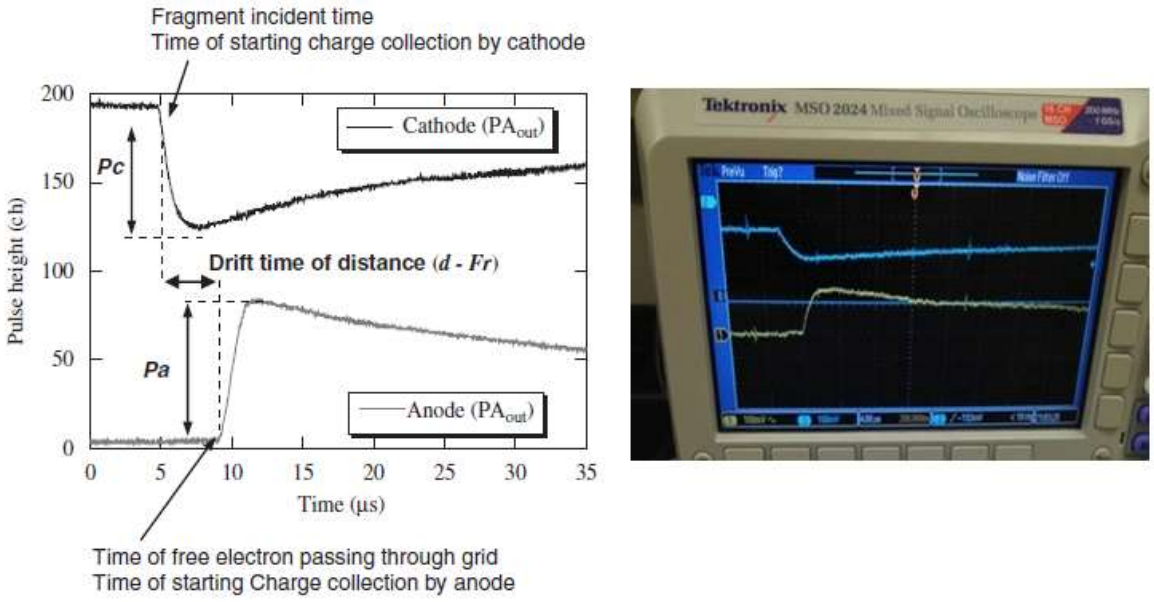


Figure 23: Signals from the charge sensitive preamplifiers connected to the cathode and anode. Left, diagram from ref [Sanami, 2008]; the point at t = 0 corresponds to the fragment incident time. Right, oscilloscope traces from our early tests.

The data depicted in Figure 24 shows the results of the experiment done by Sanami et al. who used the active cathode method for determining particle range; a timing resolution of about 140ns was reported based on drift velocity [Sanami, 2008]. It is very important to note that the species are separated down to an energy of about 0.5 MeV/amu; lower than possible with Bragg curve work. It is also important to note that the drift time can be controlled by altering the gas pressure and the distance between electrodes, thus allowing for possible optimization and improvement on timing resolution.

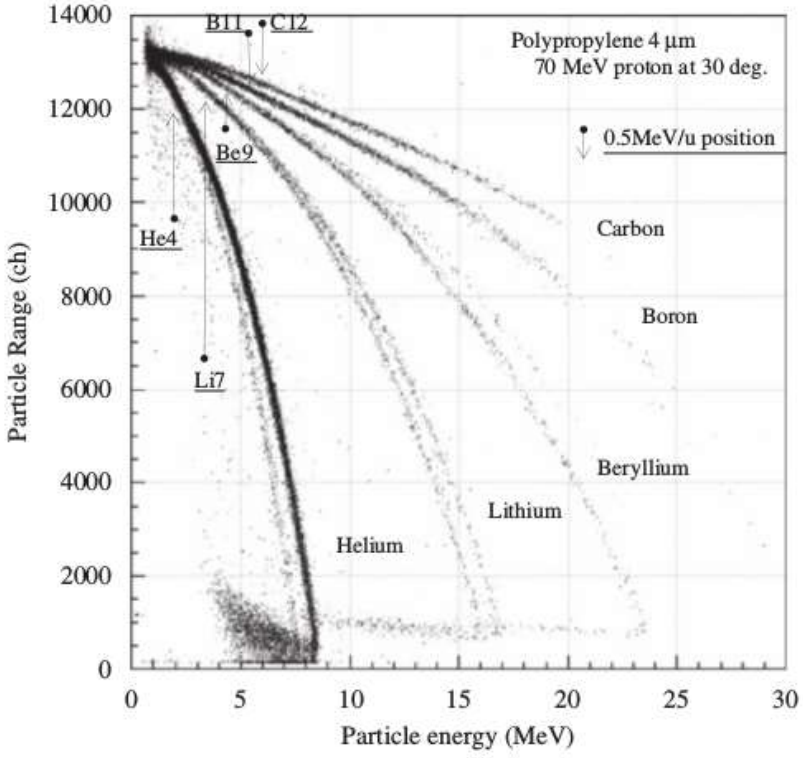


Figure 24: Active Cathode particle range results from Sanami [Sanami, 2008].

Chapter 3

Overview of Instrumentation

3.1 Ionization Chamber Physical Design

The ionization chamber uses a parallel plate chamber design; the chamber is a cylinder with the cathode and anode at opposite ends. The entrance to the ionization chamber is through a hole in the cathode. Previous designs had the cathode attached directly to the vacuum chamber. To use the cathode as an active cathode, the cathode cannot directly connect to the vacuum chamber, and this required an involved design. The ionization region for the incident particle is near the cathode, and a Frisch grid (FG) near the anode shields the anode from signal pickup from this initial particle ionization. Between the FG and cathode is a series of twelve 102 mm inner diameter copper electrode guard rings, the FG shares the same 102 mm inner diameter. A diagram of the ionization chamber

can be seen in Figure 25. The outer diameter of the anode is approximately 132 mm, and the outer diameter of the cathode, FG, and guard ring electrodes is approximately 121 mm. The distance from the face of the cathode to the face of the FG is approximately 129.1 mm. The distance between each guard ring is approximately 7 mm, as are the distance from the first guard ring to the cathode, and the distance from last guard ring to the FG. The distance from the anode to the FG is approximately 9 mm. The overall active volume between the FG and cathode is approximately 1054.9 cm^3. The cathode (C) plate has an entrance hole approximately 3 cm in diameter to allow for particle entry into the active region of the detector. The cathode plate is run at a negative potential which steps down the guard ring electrodes via the resistor chain to the Frisch grid which is grounded to the chamber wall; the anode (A) consists of a positive potential, with a stronger E field in the FG-A region than in the C-FG region. Both the anode and cathode plates are made of solid copper. The full ionization chamber assembly can be broken down into two sub-assemblies which are the anode-guard ring sub-assembly and the window-cathode sub-assembly. A solid model cut-away of the ionization chamber can be seen in Figure 26. Design drawings for all assemblies can be found in Appendix A. Extensive work has been done by Mader [Mader, 2013] in determining the electric field within an ionization

chamber similar to this design; a sample of these SIMION simulations can be seen in Figure 27.

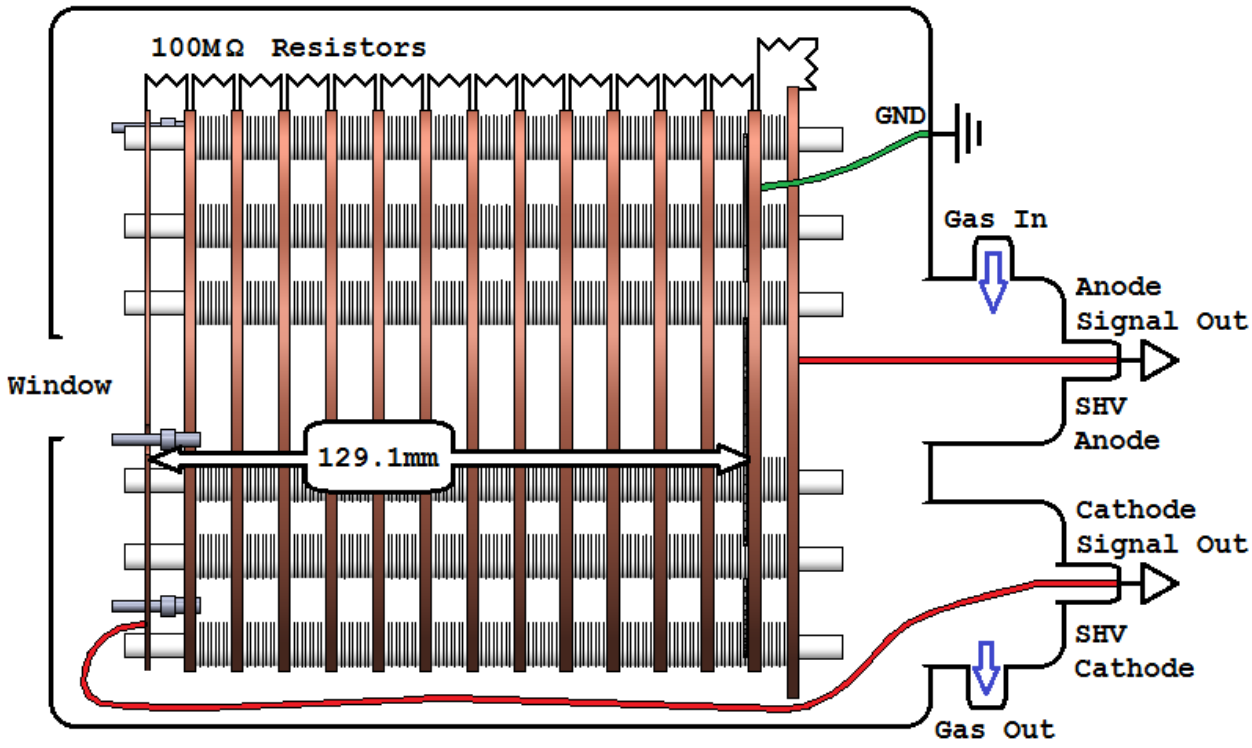


Figure 25: Schematic drawing of the ionization chamber for the UNM fission fragment spectrometer.

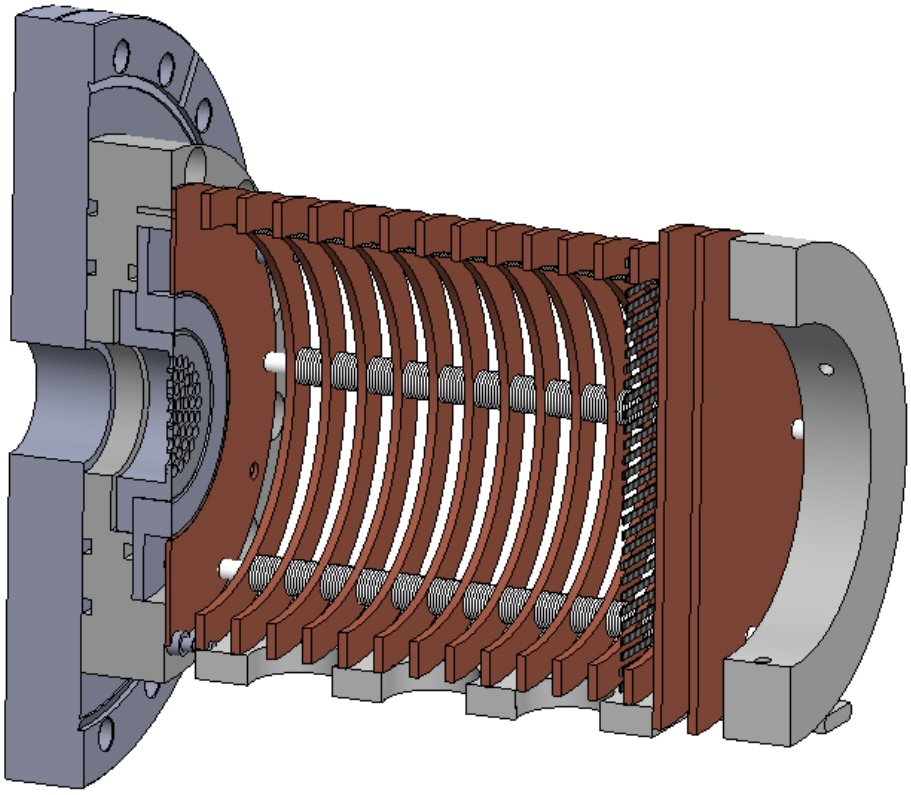


Figure 26: Solid CAD cut-away model of the UNM ionization chamber.

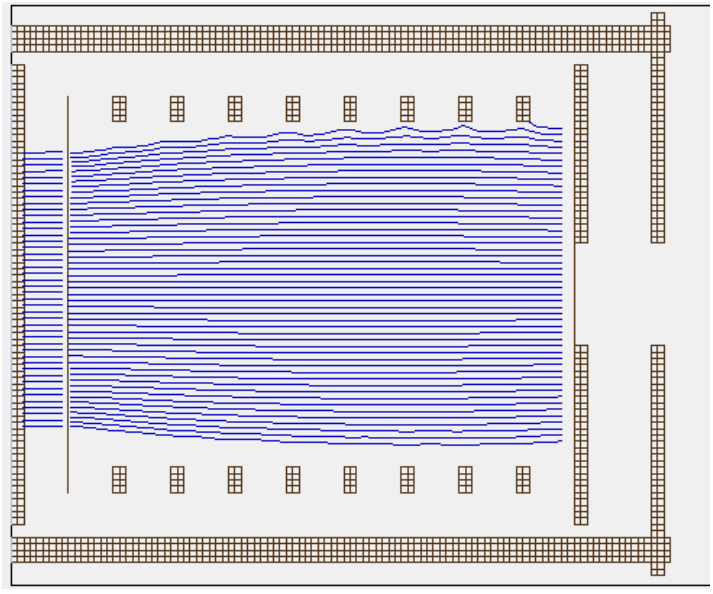


Figure 27: SIMION simulated electric field lines inside of a previous iteration of the UNM IC [Mader, 2013].

3.1.1 Anode-Guard Ring Sub-assembly

The twelve guard rings are made of solid copper gaskets and are connected to each other via soldered crimp connectors and 100 MΩ resistors. In this construction the change in voltage between each guard ring is constant. The guard rings are separated from each other by 5 mm of Teflon spacers and held in place by acetyl rods, all electrically insulating. This construction allows for the electric field within the active region of the chamber to remain uniform as it steps down along the chamber, and confines the field lines to be nearly parallel within the active region. The change in voltage between each guard ring is constant. The guard rings are made of solid copper gaskets and are connected to each other via soldered crimp connectors and resistors. The final guard ring, closest to the cathode plate, contains three male micro-banana pins attached by bronze braising. These three micro-banana connectors allow for the anode-guard ring sub-assembly of the IC, from anode to final guard ring, to plug into the window-cathode sub-assembly, as can be seen in Figure 28. These micro-banana connectors add stability and position repeatability when connecting the guard ring/Frisch grid electrode sub-assembly to the anode. Repeatability in the electrode sub-assembly placement is crucial due to the need for calibration of the detector. To maintain structural stability, the electrode assembly is attached to a thick Teflon ring beyond the anode by the acetyl rods, and the electrode structure

rests on a Teflon sled. A CAD model drawing of the detachable anode-guard ring sub-assembly can be seen in Figure 29. The distance from the Frisch grid to the anode is approximately 7 mm and is kept separated by Teflon spacers. The resistor connection from the anode to the Frisch grid is doubled that of the guard ring ladder resistors, consisting of two 100 MΩ resistors in series. Because the cathode is not grounded to the chamber, it is instead attached to a Teflon plate that is difficult to detach. Thus the remaining electrode assembly has been designed to be removed without the cathode to allow access to the IC-TOF window.

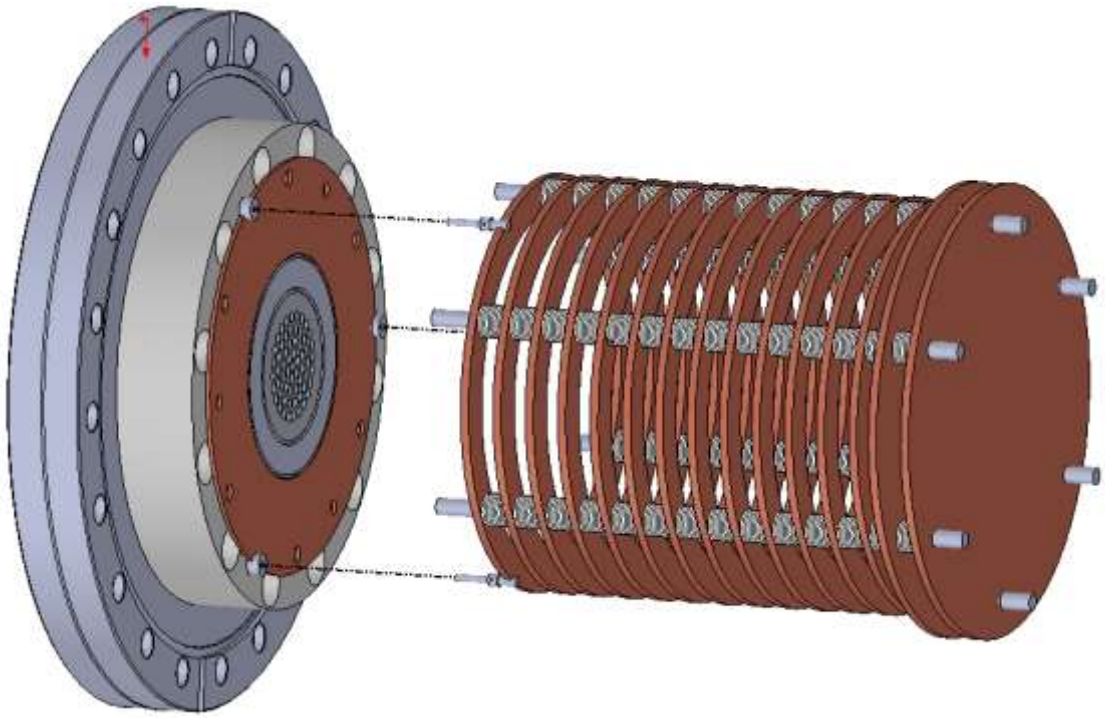


Figure 28: Exploded solid CAD model of the two IC sub-assemblies; the cathode-window sub-assembly (left) and the anode-guard ring sub-assembly (right).

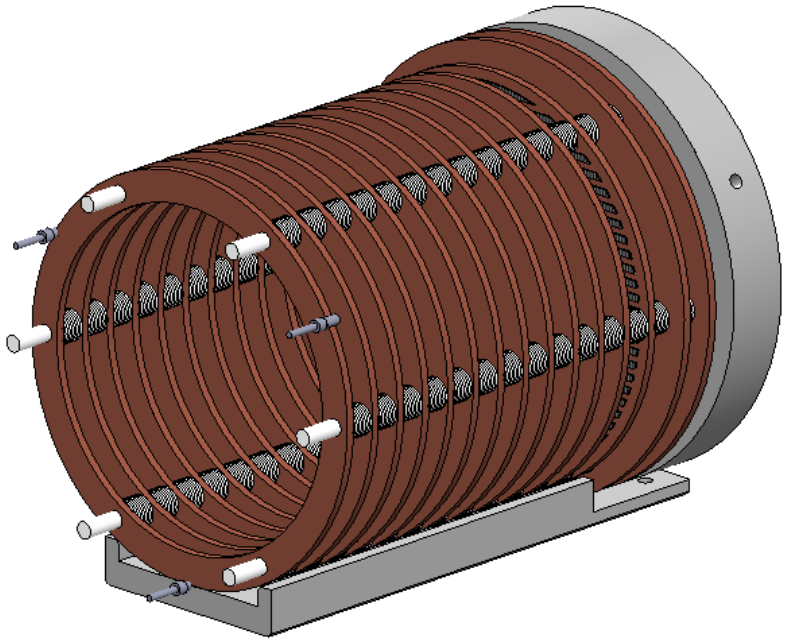


Figure 29: Solid CAD model of the anode-guard ring sub-assembly.

3.1.2 Window-cathode Sub-assembly

The window design separating the gas IC region from the vacuum TOF region in the UNM spectrometer was based on the design from the LANL-SPIDER spectrometer. The original LANL-SPIDER design consists of the window plate and mesh plate; design drawings from LANL can be found in Appendix A. A very thin window is preferred to minimize particle energy loss and straggling, but that requires backing to hold the window. The thin Mylar window we are using is backed by the backing plate to prevent window stretching and/or breaking from the pressure differential between the IC and the high vacuum TOF region. The window-backing plate inserts into the window frame and presses up

against the thin window; this basic design was used to create the UNM window. The actual hole diameter of the window frame is approximately 3 cm, but transmission is reduced by the backing. The backing plate is really a plate with holes in it, resembling a salt shaker head, as seen in the middle of Figure 30, and has a transmission of 70%. Prior to the current design, a wire mesh backing was used, but this proved too destructive to the thin Mylar windows. Unlike the design from LANL with a grounded cathode, the UNM window plate and mesh plate mate together and sit inside of a cylindrical Teflon part. The Teflon part exists to ensure that the window frame and backing tied to the cathode annulus voltage are electrically isolated from the outer chamber walls, for use as part of the active cathode to read off signal pulses. The metal pieces of the cathode-window sub-assembly are all directly connected and at the same voltage, and are insulated from the metal vacuum flange by the Teflon. A CAD drawing of the sub-assembly can be seen in Figure 30.

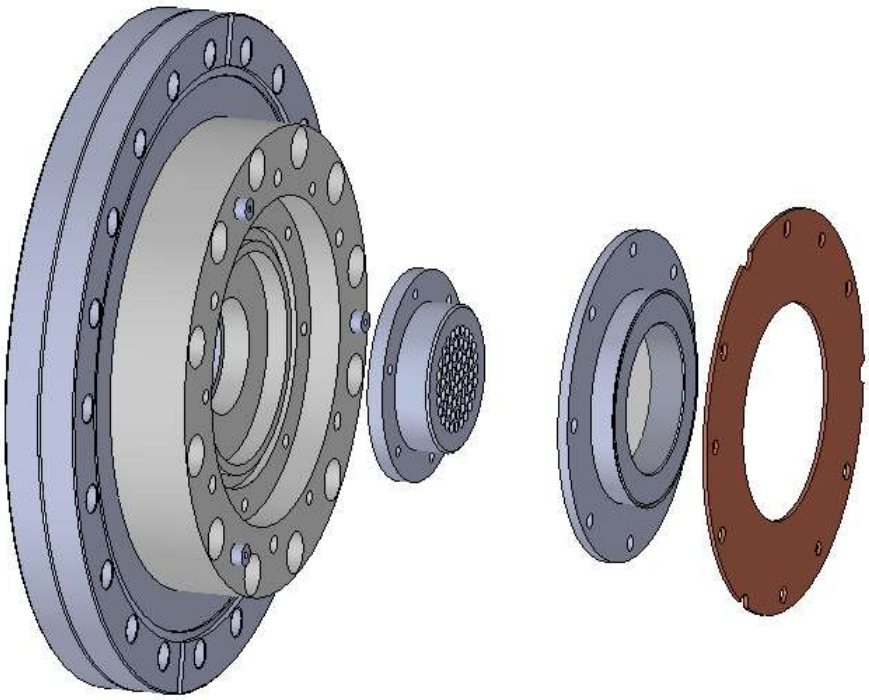


Figure 30: Exploded solid CAD model of the window-cathode sub-assembly.

The window-cathode sub-assembly is then connected to the anode-guard ring sub-assembly via a resistor and female micro-banana jacks. The resistor ensures the voltage drop from the cathode to the closest guard ring. The Teflon part holds vacuum from the TOF chamber via a seal between the Teflon and outer chamber wall, as well as a seal between the Teflon and the window plate. Again, the combination of the two sub-assemblies can be seen in Figure 28.

3.1.3 Frisch Grid

The purpose of a Frisch grid is to act as a shielding grid electrode between the anode and the cathode to screen the anode from charges within the cathode-to-Frisch-grid region. A signal is only induced on the anode when the drifting electrons cross the grid into the Frisch-grid-to-anode region. A very detailed explanation of the use of Frisch grids in ionization chambers has been written by previous graduate student Drew Mader. A previous iteration of the Frisch grid, designed by Mader, was made of FR4 copper plated circuit board with the gold-plated tungsten grid wires silver-soldered on [Mader, 2013]. The most recent design of the Frisch grid uses a copper ring that has had electro-formed gold grid mesh electroplated onto it, manufactured and electroplated by the Precision E-Forming company. The advantage to the electroplated Frisch grid is that it minimizes the vibrational noise from loose wires, and no longer has small solder joints that could cause non-uniformity within the electric field.

3.2 Ionization Gas

The quality of the counting gas can decrease over time as the gas degrades and impurities build up within the chamber [Sanami, 2008] and so gas flow is used to refresh the gas. For this work, a gas flow Proportional-Integral-Differential (PID) system was used to control the flow rate of gas into and out of the chamber to

allow for gas replacement. The main controller used is an MKS Type 250, which can be set to a pressure set point; this controller controls a pneumatic actuator that allows the gas to flow into the chamber. The main PID controller determines the amount of gas to let into the chamber based off of the reading on the piezo MKS #722B13TCD2FA pressure gauge. The gas outflow controller and power supply is an MKS Type 246 and can be set to a specific out flow rate that remains constant, allowing gas to exit through a Mass Flow Controller (MFC). Two MFC's were tested, and a 500 sccm (standard cubic centimeters per second) MFC was chosen for all experiments. The current pressure reading from the piezo gauge is read out onto an MKS #PDR-D-1 red dial and is also recorded by an Arduino Uno microcontroller every 5 seconds.

3.3 Ionization Chamber Signal Processing

Signal processing and power supplies were comprised of several Ortec NIM power supplies, amplifiers, 722 spectroscopy preamplifiers, and stand alone Ortec Easy MCAs for single channel digitization. An extensive explanation of the pulse height calculation and evaluation has been done by several references [Mader, 2013; Knoll, 2000]. For the purposes of this discussion, a very brief summary will be presented.

The IC was run in pulse mode, described below, with a Frisch grid. This enables us to collect information on the energy and timing of the pulse signal. As mentioned throughout the theory in Section 2, the incident particle ionizes gas within the active region of the chamber between the cathode and the Frisch grid. An IC operating in pulse mode measures change in voltage across a resistor from the induced current pulse on the electrode. The readout signal is produced from energy changes due to the motion of charged particles in an electric field changing the capacitance, not due to charge collection, as described in Section 2.3. As presented in Figure 30, the first initial fast rise in voltage per time of the signal is due to the movement of electrons, whereas a much slower second rise in voltage per time of the signal is due to the movement of the ions. The voltage signal per time for an example detector is presented in Figure 31 [Mader, 2013; Ahmed, 2007]. In our IC the ions travel many times slower than the electrons. The discernible pulse is from electron motion, and the ion induced pulse is not discernible above electronic noise.

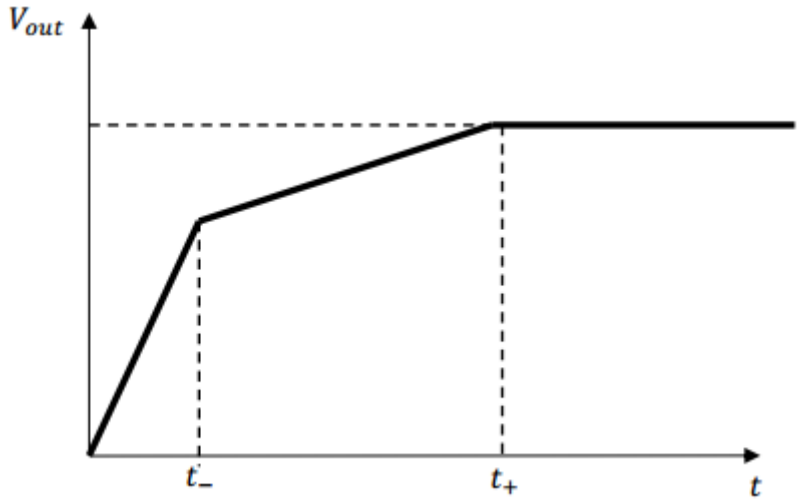


Figure 31: The output voltage as a function of time, where 0 to t- is the rise time of electrons and t- to t+ is the rise time of the ions [Ahmed, 2007].

In an ideal Frisch gridded IC, the Frisch grid completely screens the anode from induced charges produced by the drift of the ions, so the resulting anode signal is produced only due to electrons. The output voltage as a function of time for a Frisch gridded IC has a fast rise time, which allows us to quickly extract the output signal.

The cathode signal, not having a Frisch grid for screening, is produced almost immediately following ionization from the movement of both ions and electrons, though the only discernible signal is due to the movement of electrons. We are still able to readout a time-stamp signal on the cathode due to movement of the

electrons, enabling the active cathode method used for particle range measurements.

The induced signal on the anode depends on the full charge passing the Frisch grid and gives a strong signal we use to determine particle energy. In the cathode to Frisch grid region, the electrons only drift for a portion of the total length, and this is dependent on the incident particle charge and velocity following the Bethe formula. As such, the induced cathode pulse is much smaller and varies for the same energy for different species. The Frisch grid is used to prevent such effects on the induced anode pulse.

To further improve the induced pulse on the anode, the Frisch grid to anode region has a higher electric field than the cathode to Frisch grid region, increasing electron acceleration and increasing the induced pulse on the anode.

3.4 Data Acquisition System

3.4.1 Main DAQ

Initially, the IC data were collected using Ortec Easy MCAs with Maestro installed on a Windows PC. A simple schematic of this DAQ system can be seen in Figure 32.

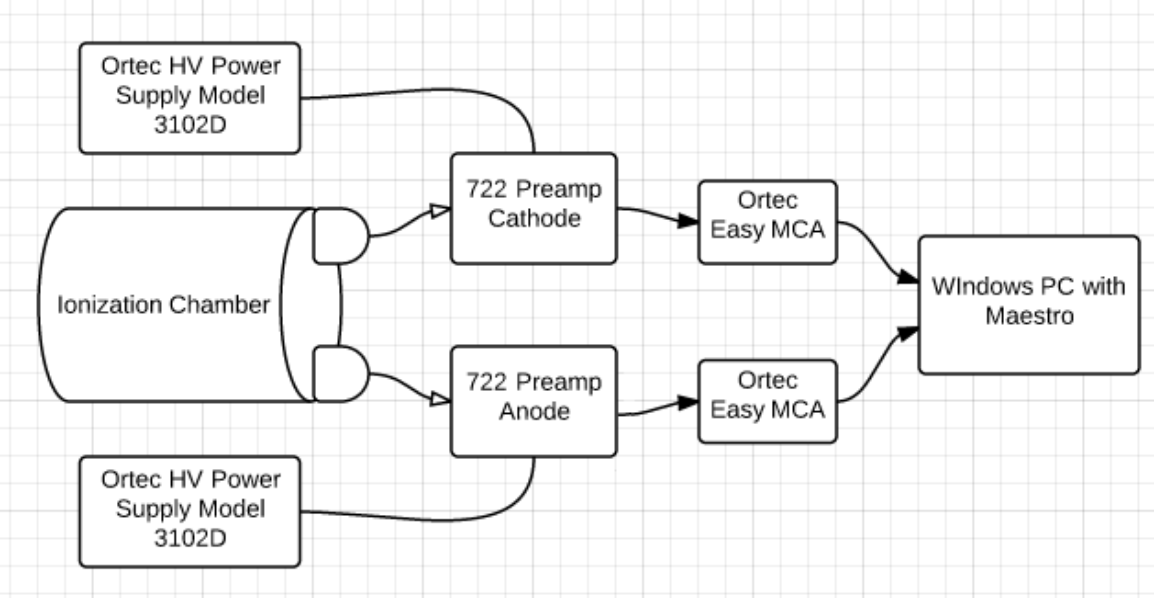


Figure 32: Schematic of the original DAQ for the IC, using Maestro.

The final data acquisition (DAQ) system used for the experiments at UNM used a CAEN DT5724 desktop digitizer. The CAEN digitizer has four signal input channels (labeled CH0 to CH3) with 100 megasamples/second (MS/s) per channel for signal digitization output and with trapezoid fit signal processing [CAEN, 2014] to give list mode pulse height vs. time for each channel. For purposes of both Bragg curve spectroscopy and active cathode measurements, only three of the four inputs were used for the experiments mentioned in this thesis. The signal from the cathode was read into the CH0 of the CAEN digitizer. The anode signal was split in two and read into CH1 and CH2 of the CAEN digitizer. The CAEN digitizer allows for signal processing within the Javascript CAEN

program, so the two anode signals can be processed using different shaping times in the trapezoid fit. A diagram of the final DAQ system can be seen in Figure 33.

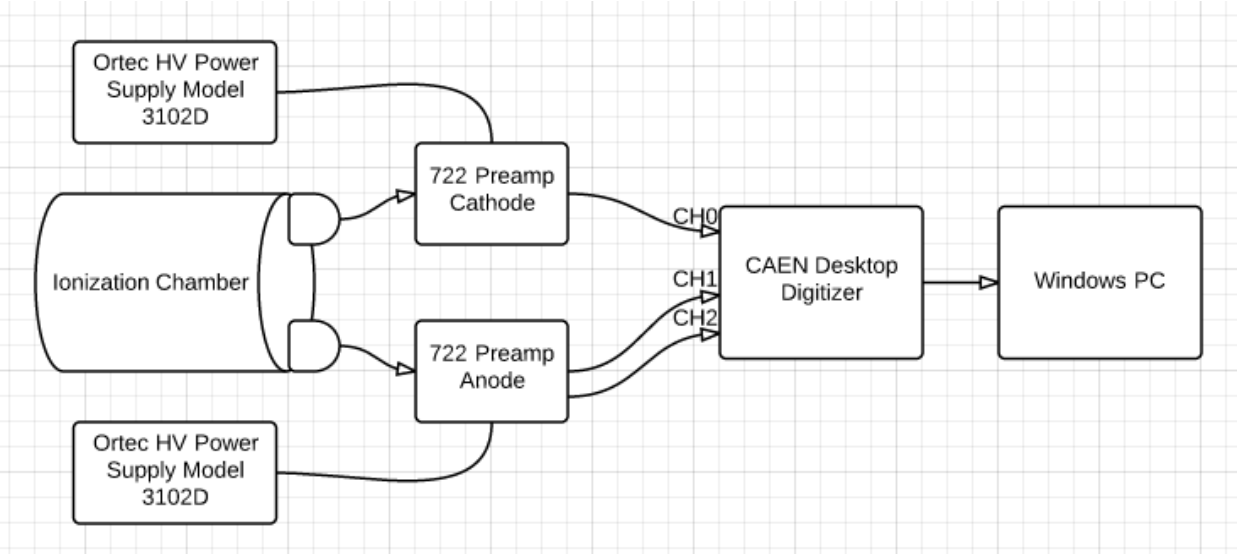


Figure 33: Electronics schematic of the signal processing and data collection system for the DAQ.

3.4.2 Arduino Environmental DAQ

The internal pressure of the IC, external pressure, and external temperature were recorded to determine if the pulse heights read out from the IC were affected by the building HVAC system. This data was recorded using an Arduino Uno microcontroller that utilized a voltage divider circuit to record the internal pressure from the piezo gauge, as well as a Bosch BMP180 pressure and temperature sensor. The data was saved every 5 seconds from the Arduino to a

PC using a python script. The Arduino circuit and python script used can be found in Appendix B. An image of the Arduino set-up can be seen in Figure 34.

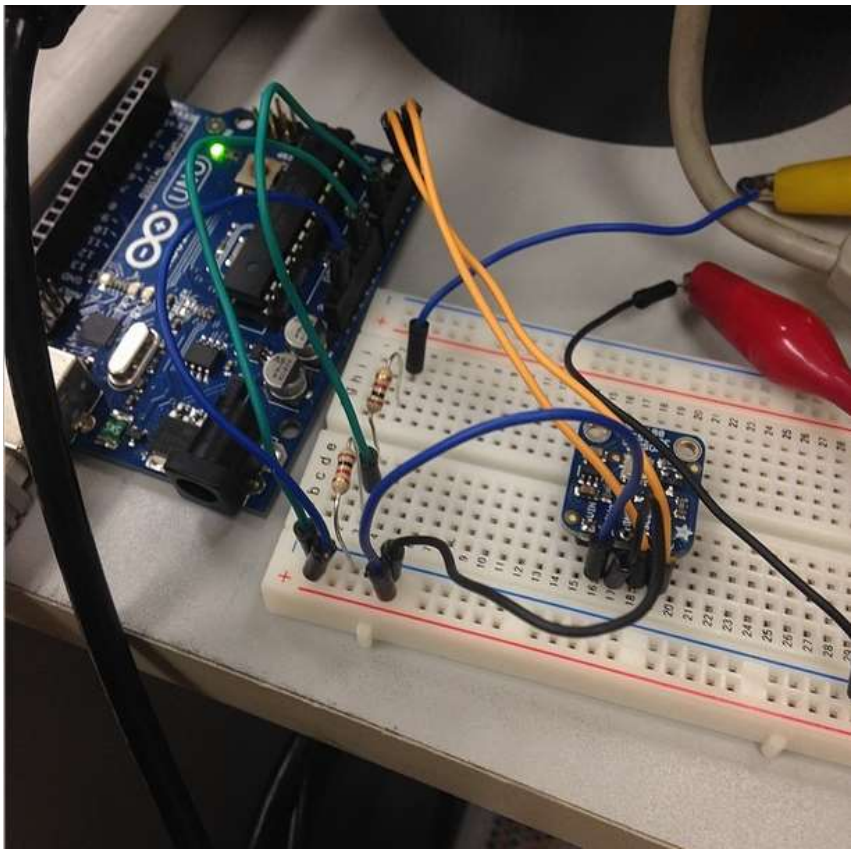


Figure 34: Photo of the Arduino circuit and sensor used to measure internal pressure, external pressure, and temperature over time.

Chapter 4

Experiments & Results

4.1 Introduction

Experiments were performed to both optimize run settings and to understand the physics of the detector. Optimization experiments consisted of the effect of gas flow rate, applied voltages, pressures, and Mylar window thickness on various metrics. The main data recorded, referred to as the standard metrics, were centroid location, FWHM, and peak area. Experiments were done using alpha particles and fission fragments.

4.2 Experimental System

The physical characteristics and electronic system of the ionization chamber (IC) has been previously described. Before placing the IC electrode assembly into the

beam pipe, all IC components and the interior of the beam pipe were cleaned with 100% ethyl alcohol. The IC electrode assembly was placed in the vacuum pipe and then plugged into the appropriate electrical connections. The vacuum pipe was closed and sealed. The IC was then pumped down using an Edwards XDS 10 vacuum pump to sufficient vacuum (< 1 mbar) to begin gas flow.

Alpha particles and fission fragments were used in various experiments. The majority of experiments were performed using ^{239}Pu as an alpha source and ^{252}Cf as both an alpha and fission fragment source. Other sources include a tri-nuclide source which contains ^{241}Am, ^{239}Pu, and ^{244}Cm. The activities and main alpha energies of all sources used are in Table 2.

Cf -252		Pu-239		Am-241		Cm-244	
Energy	Branching	Energy	Branching	Energy	Branching	Energy	Branching
6118	84.2	5106	11.94	5443	31.3	5664	0.02
6076	15.7	5144	17.11	5486	84.8	5763	23.1
5977	0.25	5157	70.77	5545	0.37	5805	76.9

Table 2: Alpha energies in keV and branching in % for sources used [BNL, 1952].

4.2 Window Thickness Pressure Tests

As shown in several figures, the gas-filled IC was separated from the high vacuum TOF region with a thin Mylar window that allows particles to pass into

the IC. Thin Mylar windows were mounted on window frames using epoxy resin to produce a gas tight seal. Window testing was performed for 1 μm, 1.5 μm, and 2.5 μm thick Mylar windows to ensure P-10 gas would not leak. Thinner windows are preferred to reduce energy straggling of the fission fragments, but a working detector was the first priority. The 1 μm and 2.5 μm tests were done with both the old window backing, Figure 35 (wire mesh), and the new window backing Figure 36 ("saltshaker"). These tests were done to determine which pressures the detectors could operate at without a significant leaking or diffusion of gas from the IC chamber to the TOF region, as well as to determine the maximum pressure the windows could withstand. The "saltshaker" window backing was more successful in not puncturing the Mylar window, and was chosen as the primary window backing.

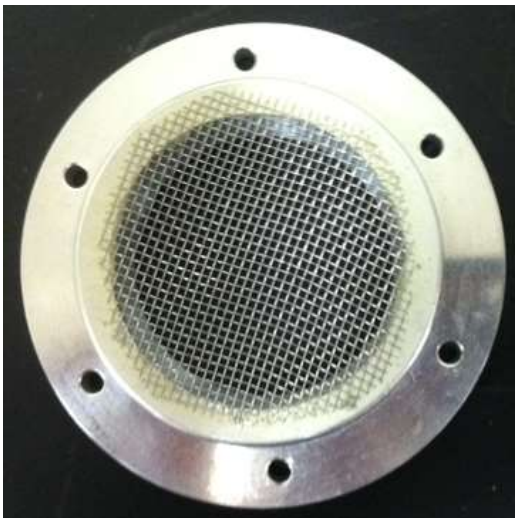


Figure 35: Original wire mesh window backing for the TOF-IC window.

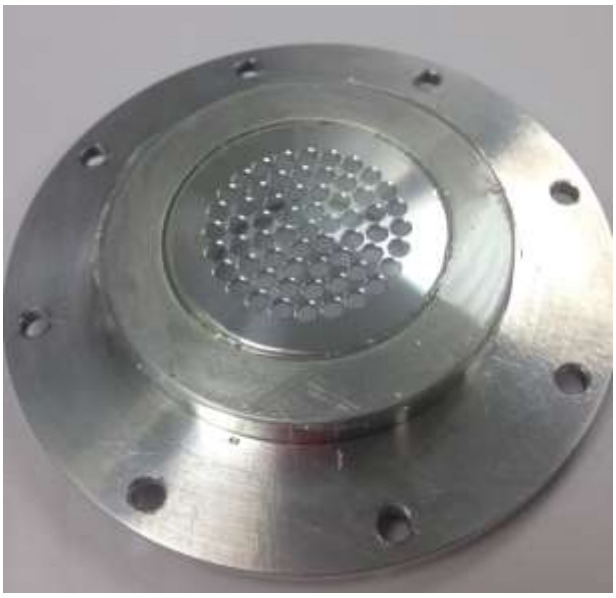


Figure 36: "Saltshaker" window backing with the surrounding window frame for the TOF-IC window. The mylar is stretched across, and epoxyed to, the window frame.

We determined that the 1.0 μm and 1.5 μm Mylar windows showed a decreased pressure within the IC chamber over a period of 24 hours without gas flow, for both the mesh window backing and the "saltshaker" window backing. Either a leak existed between the chambers due to a seal, or the gas was diffusing through the Mylar. An experiment was done using a flat piece of solid aluminum in place of the window frame to determine whether a leak existed due to the seal. With the flat plate, no pressure change was observed, leading to the conclusion that either a leak existed within the window or that the gas was diffusing through the Mylar.

The 2.5 μm Mylar window with the "saltshaker" window backing was placed into the chamber and held pressure overnight (24 hrs) without change, repeatedly for both full window removal and reinstallation and for gas cycling. Thus, all measurements using the full spectrometer were then done using 2.5 μm Mylar windows with the "saltshaker" mesh backing.

Tests were performed on the 1.5 μm and 2.5 μm windows without mesh backings to determine the maximum pressure that the window could hold before breaking. The pressure was raised at a slow (< 5 Torr/s) rate until the Mylar reached its limit and broke. The results of these tests can be found in Table 3. Based on testing, we determined that the 2.5 μm window could be used to an IC pressure of 250 Torr, without a backing. For IC measurements, the window was always backed. Though this reduces transmission efficiency, it maintains a constant plane for the gas boundary and provides continuity for the cathode to maintain the uniformity of the electric field.

Thickness (μm)	$P_{initial}$ (mmH2O)	P_{final} (mmH2O)	ΔP (Torr)
2.5	-26.9	-15.8	281.9
2.5	-25.8	-15.0	274.3
1.5	-25.9	-20.2	144.8
1.5	-27.2	-20.1	180.3

Table 3: Results of Mylar window tests without mesh backing.

4.3 Pressure Tests

Experiments were done to better understand the energy resolution (ER) at different pressures. As described in Section 2.4 the reduced electric field, E/P, affects the drift velocity of the electrons within a gas. In one experiment, the drift velocity was kept at a constant by keeping the E/P value at a constant and the standard metrics were recorded, recalling that standard metrics are centroid location, FWHM, and peak area. As the pressure decreases, the voltage must be decreased to preserve the reduced electric field, E/P. The results of this experiment can be seen in Figure 37, and tell us that as the pressure is decreased, regardless of the drift velocity, the energy resolution increases (gets worse). One possible explanation for the increase in energy resolution could be due to the decrease in gas pressure, and thus a decreased stopping power; some of the alpha particles may be penetrating past the Frisch grid without depositing their full energy in the active region of the chamber because of their increased range [Mader, 2013]; an effect called "punch through".

A second experiment was done, expanding on the first experiment, looking at pressures for different values of E/P. In this experiment, as seen in Figure 38, data was taken based on ER vs. E/P for different pressure sets. Here the effect of a lower pressure on energy resolution is more distinct; at higher pressures the ER

is much lower, regardless of E/P (and hence drift velocity), whereas the ER increases at lower pressures. This again supports that higher stopping power of the gas improves the energy resolution. Using this data, we can better understand how to optimize the IC when a pressure change is made.

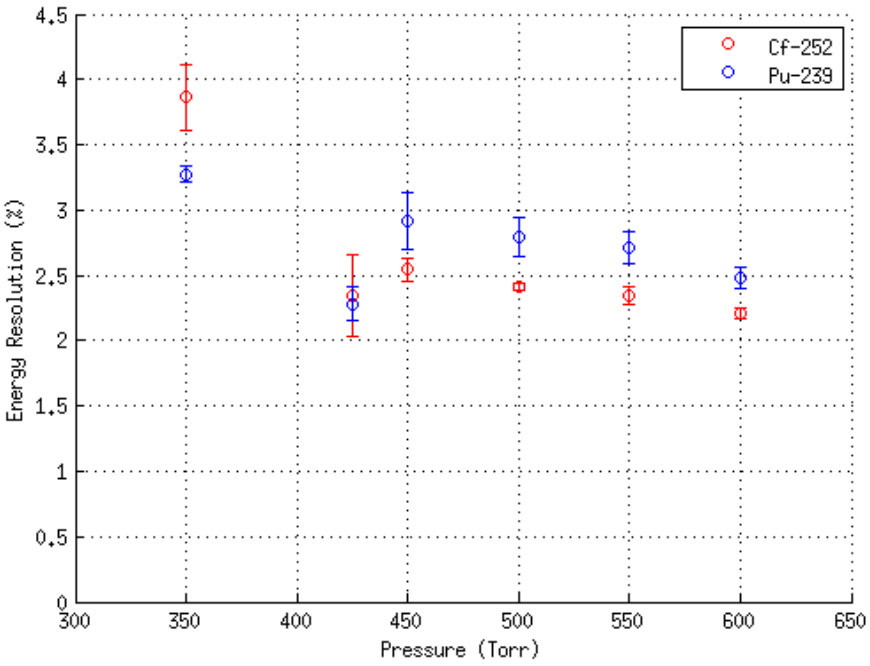


Figure 37: Graph showing the effect of pressure vs. alpha (5156 keV) energy resolution when the drift velocity (related to E/P) is kept constant.

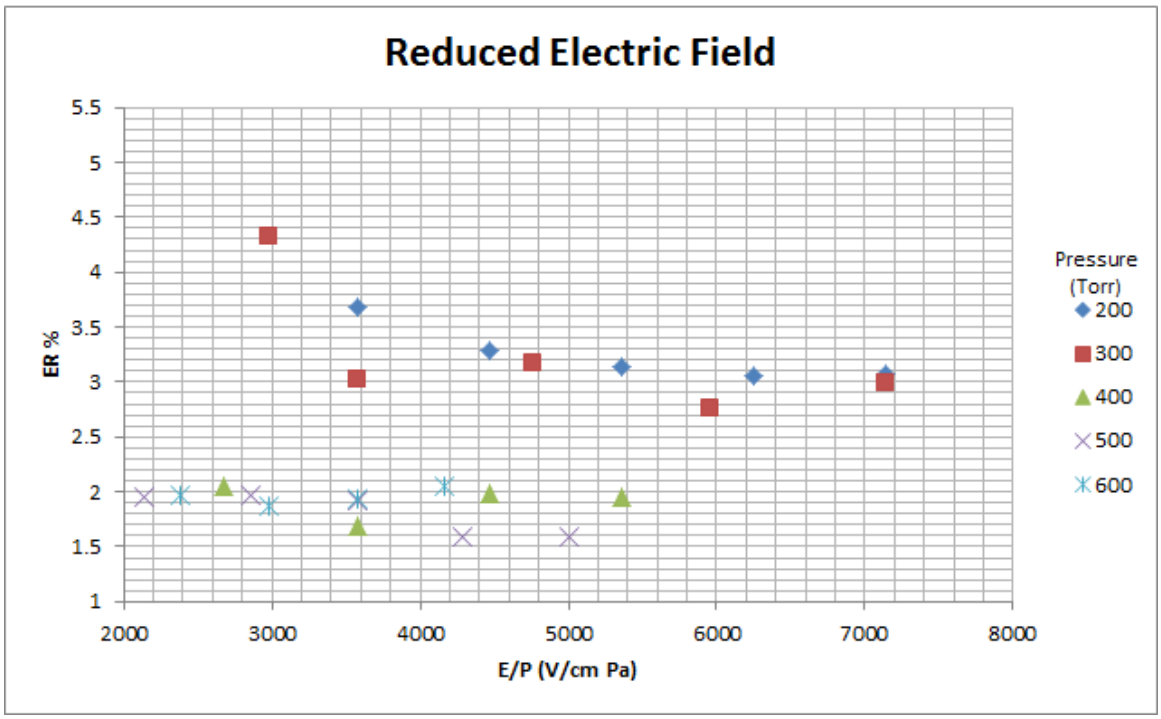


Figure 38: Graph showing the effect of different E/P values at different pressures vs. alpha (5156 keV) energy resolution.

4.4 Peak Drift

Examples of long and short acquisition time IC spectra are presented in Figure 39. We noticed that IC signal peak height from alpha particle tests changed for longer times, while no intentional system changes were made. Several tests were performed to try to understand the cause and to minimize the effect.

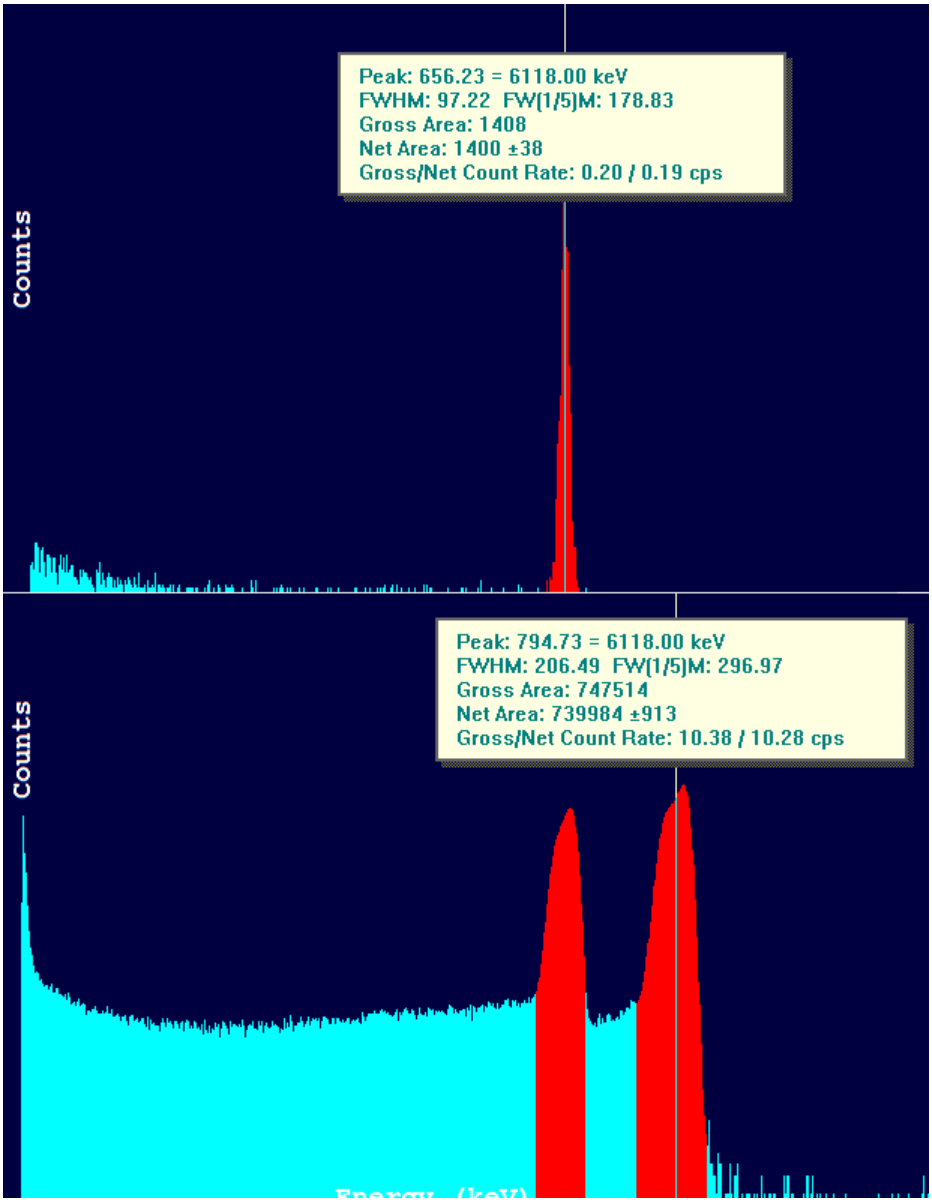


Figure 39: (top) ^{252}Cf alpha particle energy data taken for 7200 s (2 hrs), showing no centroid drift; (bottom) ^{252}Cf and ^{239}Pu alpha particle energy data taken for 7200 s, showing centroid drift.

4.4.1 External Environmental Effects

We used the Arduino Evironmental data acquisition (DAQ) to record internal pressure, external pressure, and temperature to determine whether or not the lab

building's HVAC system was having any effect on the peak drift or energy resolution. Measurements with the Arduino DAQ and the IC were taken for a period of 48 hours. The centroid locations of the alpha peaks were recorded once every 2 hours and plotted against the temperature, humidity, and pressures, as seen in Figure 40. No correlation was found between peak drift and environmental conditions. This drift must still be understood.

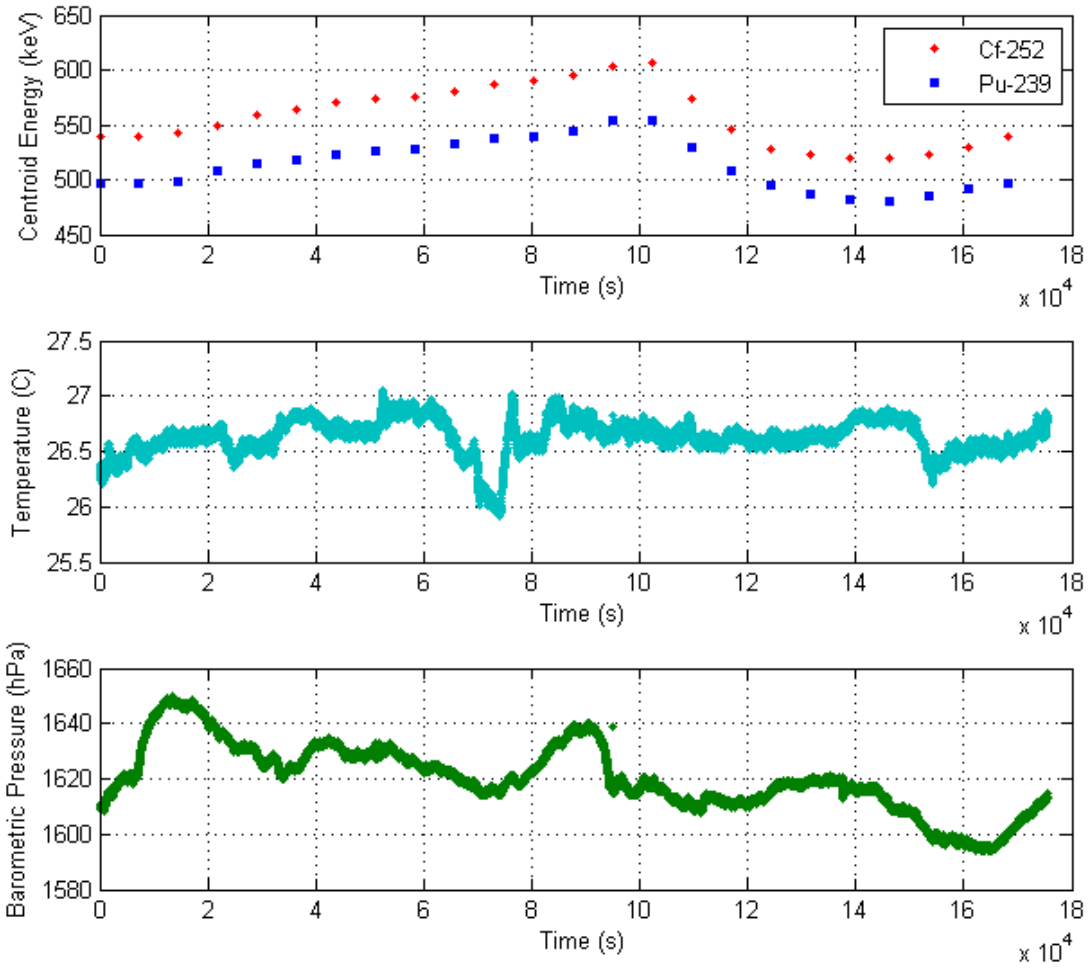


Figure 40: Data showing no correlation between IC peak centroid location from alpha particle radiation (top), external temperature (middle), and external pressure (bottom).

4.4.2 Gas Flow

The gas flow controller originally used was a 10 sccm Mass Flow Controller (MFC). We were able to acquire a 500 sccm MFC and determined that the 500 sccm MFC was a better option based on a simple comparison test of peak drift, seen in Figure 41. We then altered the gas flow rate using the 500 sccm MFC to determine if we could decrease the amount of centroid drift over time [Figure 42]. We determined that further testing is needed to determine the optimum gas flow setting to minimize peak drift. Researchers at LANL have found a similar problem in their ionization chamber and suggested segmenting the data into 2 hour blocks and then individually calibrating each data set to combine into one full data set. This is the method that will be used until further optimization is done on the gas flow system.

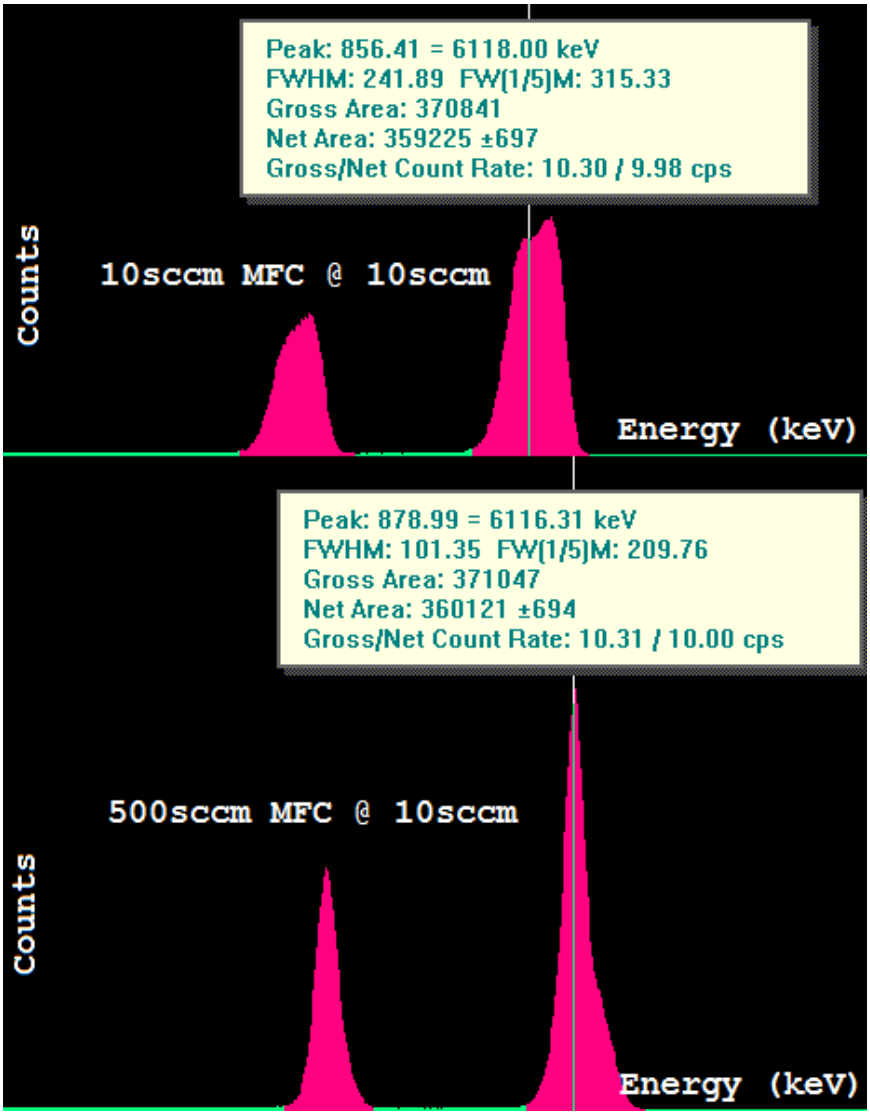


Figure 41: MFC comparison of the 10 sccm MFC (top) and the 500 sccm MFC (bottom) both run for 10 hours with flow set to 10 sccm on both controllers. The 500 sccm peaks show less drift based broadening.

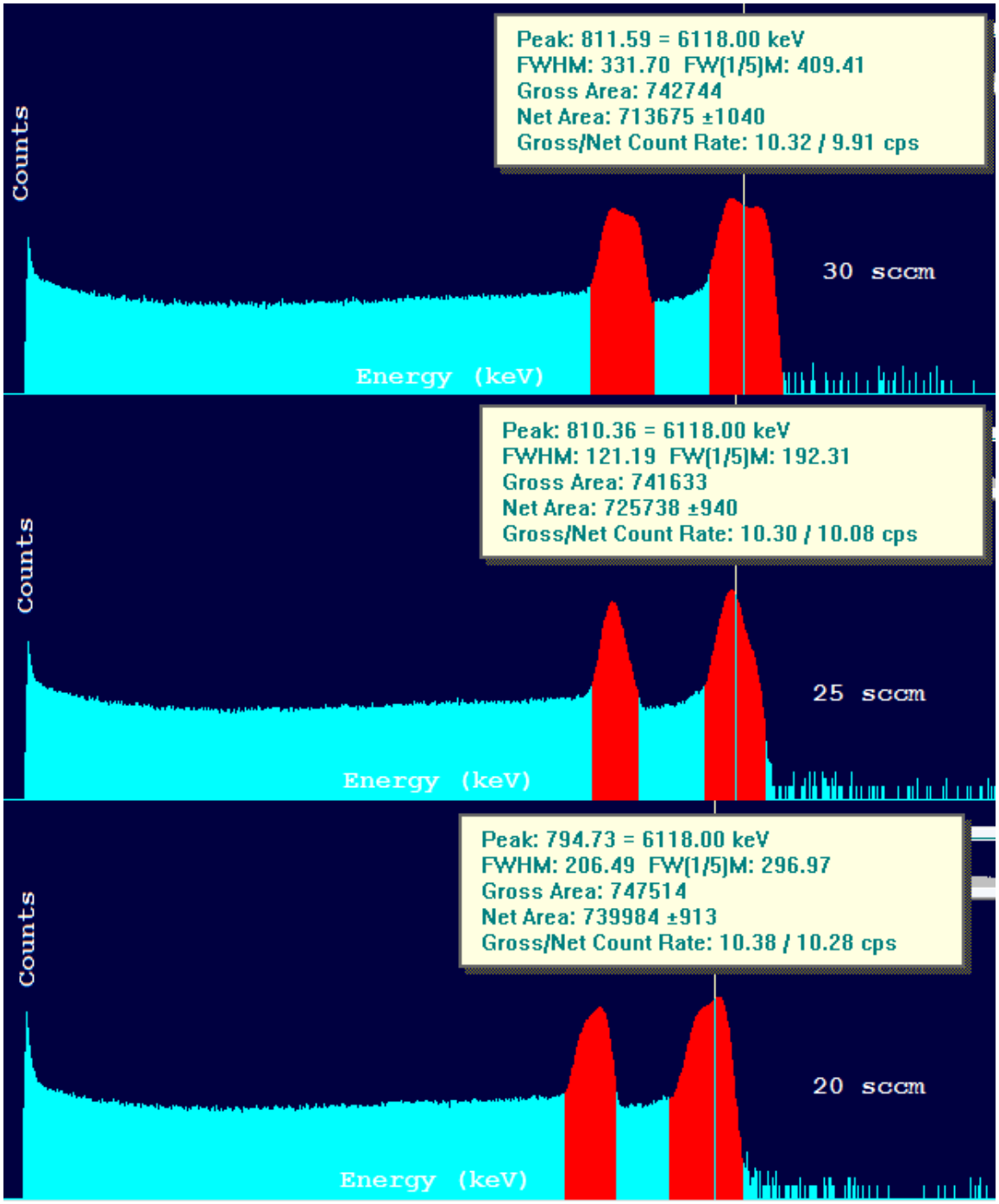


Figure 42: Overnight (12 hrs) drift with gas flow at 30 sccm (top), 25 sccm (middle), and 20 sccm (bottom). The optimimal flow rate is not clear.

4.4.3 Peak drift stability

The pressure and voltage were kept constant, and data was recorded with corresponding timestamps. This allowed us to analyze the data in one hour and two hour blocks. The Arduino environmental DAQ was used to ensure that the internal pressure remained constant for the duration of the experiment. For this experiment, gas flow was used to ensure minimal gas impurities. We then looked at the standard metrics, specifically centroid location, for each data segment with respect to time. The results of this experiment can be seen in Figure 43.

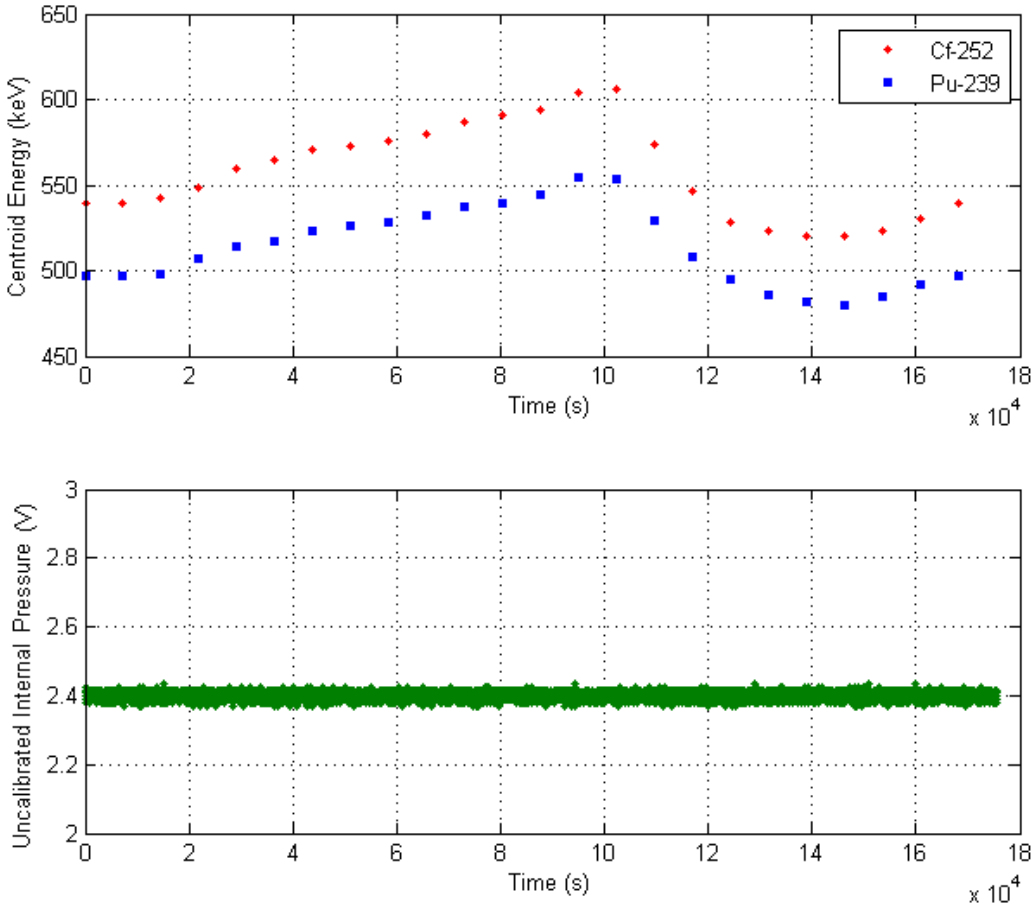


Figure 43: Results of tracking internal pressure and centroid location over a period of 48 hours.

We determined that the internal pressure remains constant to within +/- 0.125%, though the centroid location continues to drift. We examined temperature and pressure and saw no correlated changes. The drift is still unaccounted for but may be reduced by high flow, or corrected for in the data analysis by examining data over small time periods within long data runs.

4.5 Voltage Tests or E/P

4.5.1 Energy Resolution

The applied voltage on the IC between the cathode and FG directly affects the drift velocity in the active region. This being the case, it is important to look at the effect of voltage change on the energy resolution, examined in Figure 44.

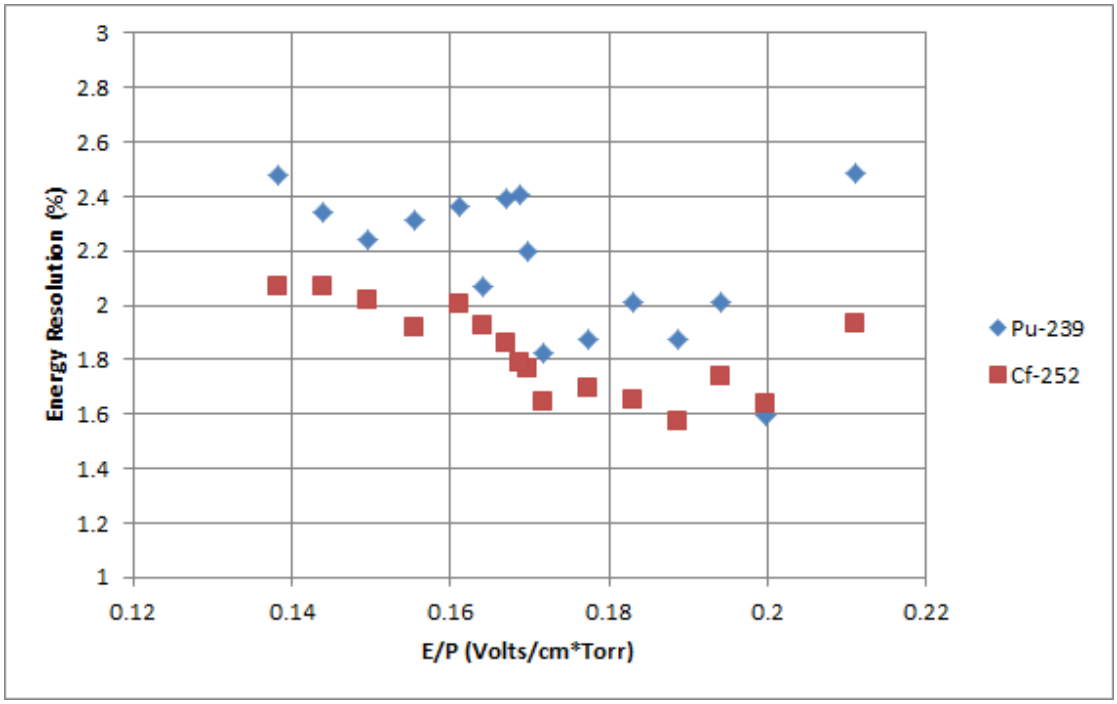


Figure 44: The effect of voltage change (E/P) on energy resolution for a pressure of 350 Torr.

Recalling the E/P vs. drift velocity curve for P-10 gas, we notice in Figure 44 a dramatic improvement in energy resolution from around 2% at 0.16 Volts/cm*Torr to around 1.6% at 0.19 Volts/cm*Torr. The experimental E/P is not

exactly where the maximum drift velocity would be expected, as the experimental E/P value is approximate, though the improvement in resolution may still be related to the drift velocity maximum. Further investigation on the effect of voltage change on the energy resolution has been performed extensively by Mader [Mader, 2013] on an IC similar to ours. Based on the data from Mader there also exists an improvement (drop in %) in energy resolution at an E/P value that may correspond with the maximum drift velocity peak.

4.6 Alpha Range Tests

Due to the structural limitations of the thin Mylar window, the internal pressure of the IC must be fairly low (100-300 Torr). SRIM [Ziegler, 2104] simulations were run to determine the ranges of various alpha particles and fission fragments in P-10 gas. The results of the SRIM tests can be seen in Figure 45, with range inversely proportional to pressure. The results follow the standard functional dependence [Turner, 2007]:

$$R[g/cm^2] = R[cm]\rho[g/cm^3] \qquad [Eq. 14]$$

Where $R[g/cm^2]$ is considered constant for a given projectile, energy, and target material, and the gas density is proportional to pressure.

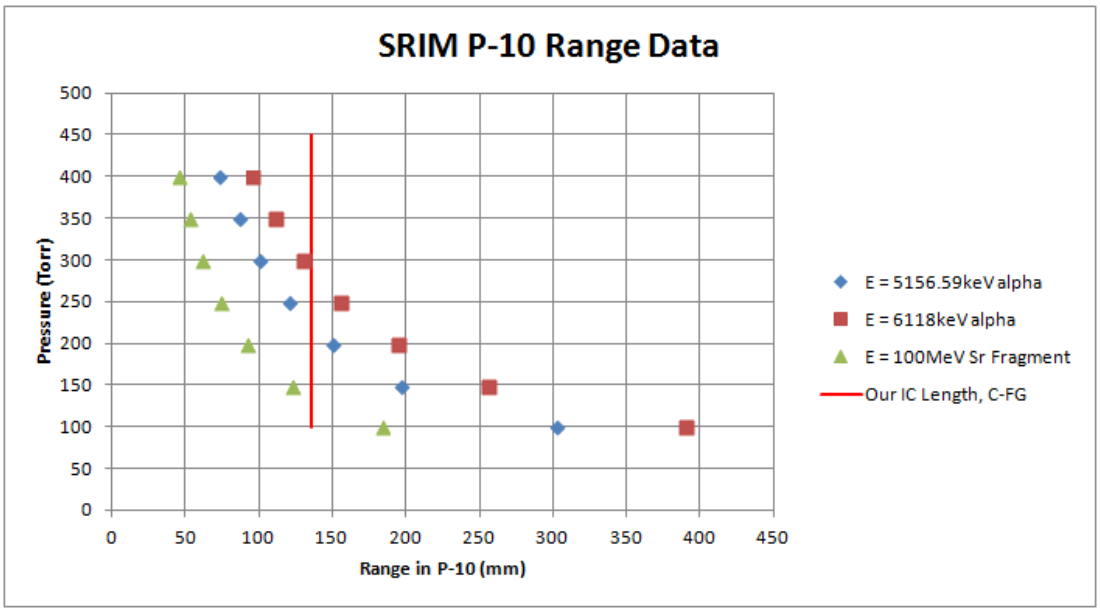


Figure 45: Range data for alphas and fission fragments in P-10 gas at different pressures with relation to our chamber length (red line).

Experiments were run using ^{252}Cf and ^{239}Pu alpha particle sources to confirm when the alpha particles started "ranging out," passing through the active region of the detector and thus depositing only partial energy in the active region. The standard metrics were recorded for these experiments. It was found that, as predicted by SRIM, the 6.1 MeV ^{252}Cf alpha particles range out at below 250 Torr in the 13 cm chamber. This was evident by observing the movement of the ^{252}Cf centroid peak location from a high channel number to a lower channel number, meaning the full energy was not being collected, and hence that the particle was ranging out, while lower energy alpha particles from Pu (5.1 MeV) produced consistent peaks.

4.7 Lateral Measurements

The IC was designed to have a uniform response within the active region. One test of this is to send collimated alpha particles into the chamber from different lateral positions from the IC centerline. Several pieces of FR4 were used to create a source holder that could be adjusted laterally. This source holder was then marked to designate several lateral positions, in 0.5 cm steps. A collimated ^{239}Pu source was placed in the holder, and standard metrics were recorded to extract resolution for sets (three) of two hour measurements at different lateral locations. The results of this experiment can be seen in Figure 46. As seen in the graph, there is very little effect on the energy resolution as the source is moved laterally within 3 cm of axial center (meaning an entrance window of up to that radius may be used without negative effects on energy resolution) and only a small degradation in resolution out to 4 cm. Though not statistically significant, the energy resolution increases very slightly with an increase in collimated source position from the axial center, though still below 1.5% out to 3 cm lateral position. Further investigation on lateral measurements in regards to energy resolution in ion chambers can be found in the previous thesis by Mader [Mader, 2013].

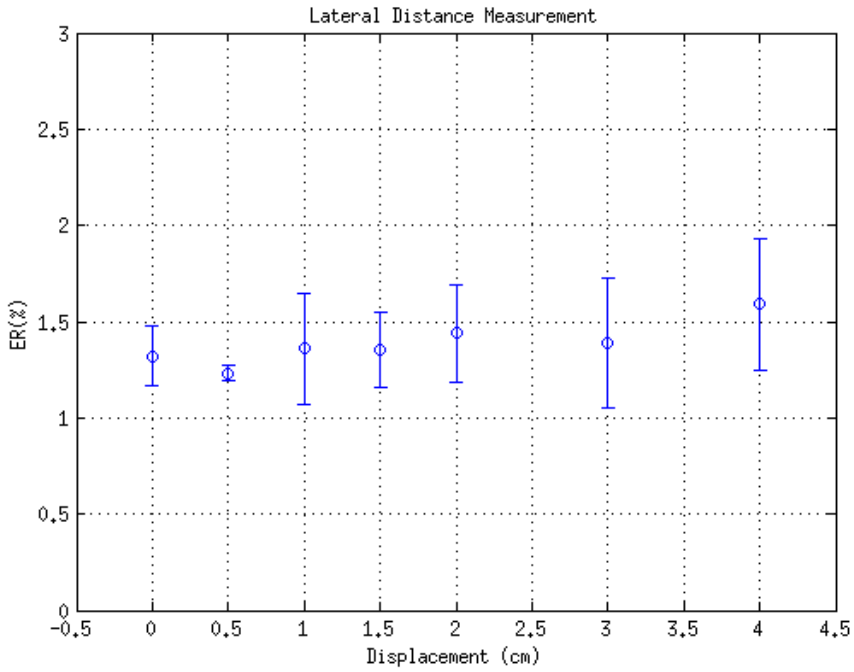


Figure 46: Lateral testing results starting from the detector's axial center (0 cm) showing a very slight increase in energy resolution percentage as the alphas approach the edges of the ion chamber guard ring interior diameter.

4.8 Noise Reduction

A significant portion of time for this project was spent determining noise sources. Electronic noise within the system can be caused by a variety of different sources and can have dramatic effects on the signal output. Several techniques were explored to minimize the noise within the detector.

The first method explored was to place a capacitor in parallel with the grounding wire to the Frisch grid. By placing a capacitor in parallel with the grounding wire, an RF filter is introduced to the system that should filter out higher

frequency noise sources. This technique was not used in the final design because it did not contribute to decreasing noise in the output signal.

One of the major noise sources in the IC signals for both the anode and cathode is thought to be vibrational noise. The biggest improvement made on vibrational noise reduction was the replacement of the metal KF-50 roughing pump hose with a plastic KF-50 hose. This succeeded in eliminating low frequency vibrational noise within the system.

Another technique used to eliminate and reduce noise was to determine ground loops or antennas. This was accomplished by touching wide metal grounding straps to various external parts of the system. One of the most significant sources of RF noise was eliminated by wrapping the pre-amp boxes with grounding straps. The external BNC and SHV male connectors of the pre-amp box were acting as antenna for RF frequencies; by wrapping a grounding strap around these connectors we were able to reduce our high frequency noise, the effects of which can be seen in Figure 47.

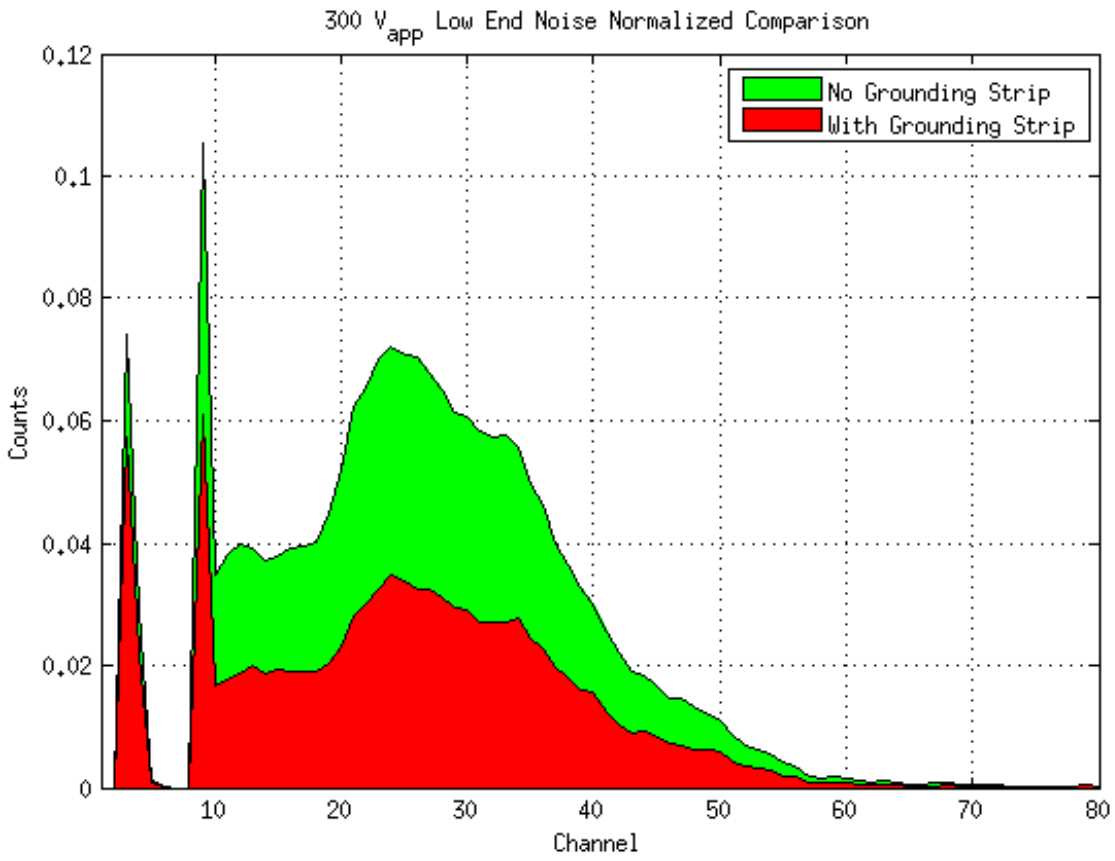


Figure 47: Normalized low-end energy measurements of before (green) and after (red) grounding straps were wrapped around the cathode preamp. RF noise was significantly decreased by wrapping grounding straps around the preamps. The cutoff below channel 10 is just an artifact of the data acquisition threshold.

4.9 Z Determination

Fragment mass determination may be performed by finding velocity and energy values, which are based on standard analysis of the TOF and IC systems. To extract the particle atomic number (Z), the stopping power (-dE/dx) can be examined in the gas through a further analysis of the IC system. Two methods to

implement this in the UNM spectrometer ionization chamber are discussed: Bragg Curve Spectroscopy and Active Cathode timing.

4.9.1 Bragg Curve Spectroscopy

As described in Section 2.6.1, Bragg curve spectroscopy is valid for alpha particles as well as light fission fragments (> 1 MeV/amu) where the peak of the Bragg curve is discernible. The Bragg peak area and the full area of the Bragg curve were compared using different time domains in the data acquisition. The CAEN desktop digitizer was used to record measurements from the anode signal for various alpha sources. To read the different components of the Bragg curve, the anode signal was split into two channels, CH1 and CH2, with different shaping times used on each channel. A long signal integration time is proportional to the particle energy, while a short signal integration time is proportional to Bragg peak height. Thus the same short signal size reflects the same Z over a range of long signal sizes, as discussed in the theory section. The long shaping time on CH1 was chosen to be 3 μs, and the short shaping time on CH2 was chosen to be 0.5 μs based on observed signal response and raw pulse duration. Data was taken for the ^{239}Pu alpha source and the ^{252}Cf source. The results of these tests can be seen in the following Figures 48 and 49.

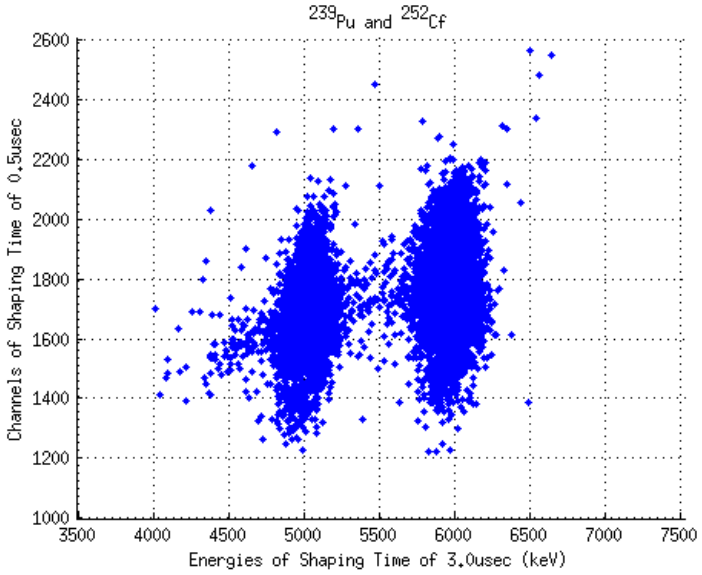


Figure 48: Bragg Curve Spectroscopy results for alpha particles. This is an expanded view of the low energy section of Figure 49.

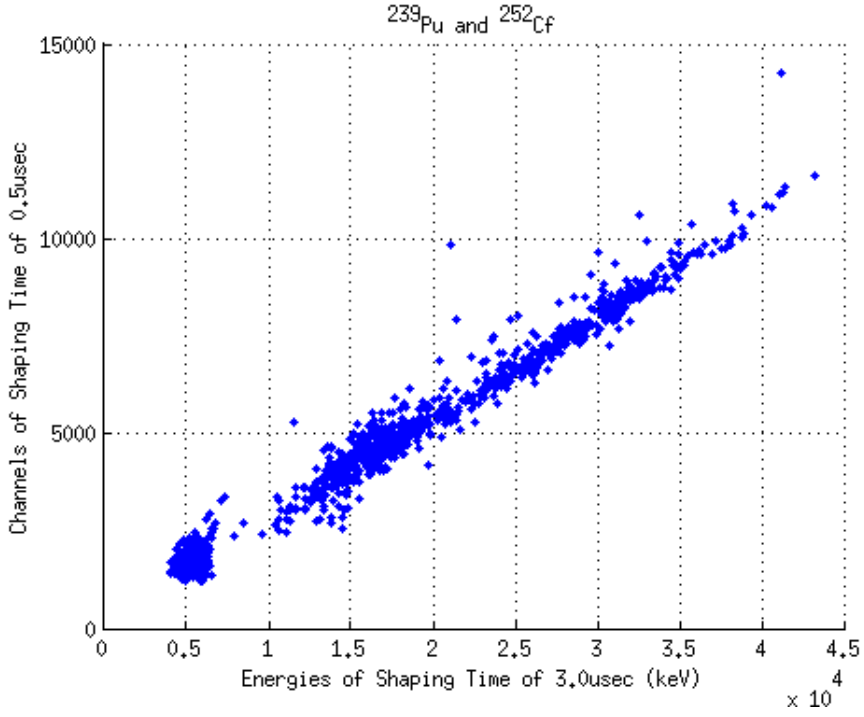


Figure 49: Bragg Curve Spectroscopy results for fission fragments and alphas, noting the horizontal scale is 10^4 keV.

Figure 48 shows the Bragg peak height for alpha particles, which corresponds to Channels of shaping time of 0.5 μs, on the y-axis. As predicted by theory in Section 2.4, the Bragg peak height is consistently the same for alphas, as seen in the short shaping time axis, though the alpha energies are different. For the fission fragments in Figure 49, the Bragg peak heights of the light fragments are apparent in the lower channels around 5000 on the y-axis. The heavy fragments are shown on the plot, but Bragg peaks are not discernible for these. At the pressures used to prevent alpha particle punch through, the fission fragments are stopped near the cathode, and it is possible that straggling in the electron drift towards the Frisch grid may spread out the sharpness of the Bragg peak. This technique was demonstrated in literature for fission fragments at lower pressures [Tyukavkin, 2009], so further investigation with our system is warranted.

4.9.2 Active Cathode Energy Extension

An active cathode can be used to determine more information about the charge of heavy and light fission fragments (> 0.5 MeV/amu). As mentioned in the theory of Section 2.5, the active cathode uses the cathode signal (t_{IC1}) and anode signal (t_{IC2}) as time stamps to determine the range of a particle. The difference in cathode and anode pulse timing, Δt, is presented in Figures 50-53. Using the Bethe formula, Equation 12, combined with the other measured parameters such

as energy and velocity, the charge of the particle can be determined. Again, data was taken for the ^{239}Pu alpha source, the tri-nuclide source, and for the ^{252}Cf source. The results of the active cathode timing and energy data can be seen in Figures 50-53. The difference in range from alpha particles of different energies is immediately clear in Figures 50 and 52 from the difference in timing Δt, and can be seen along with fission fragments in Figure 51. Bragg curve results for just the fission fragments are seen in Figure 53. The pressures were optimized to examine alpha particles, which have a much lower stopping power than fission fragments, and so the range of fission fragments is much shorter and resolution not as clear. A more detailed analysis on the active cathode results is presented in Section 5.2.

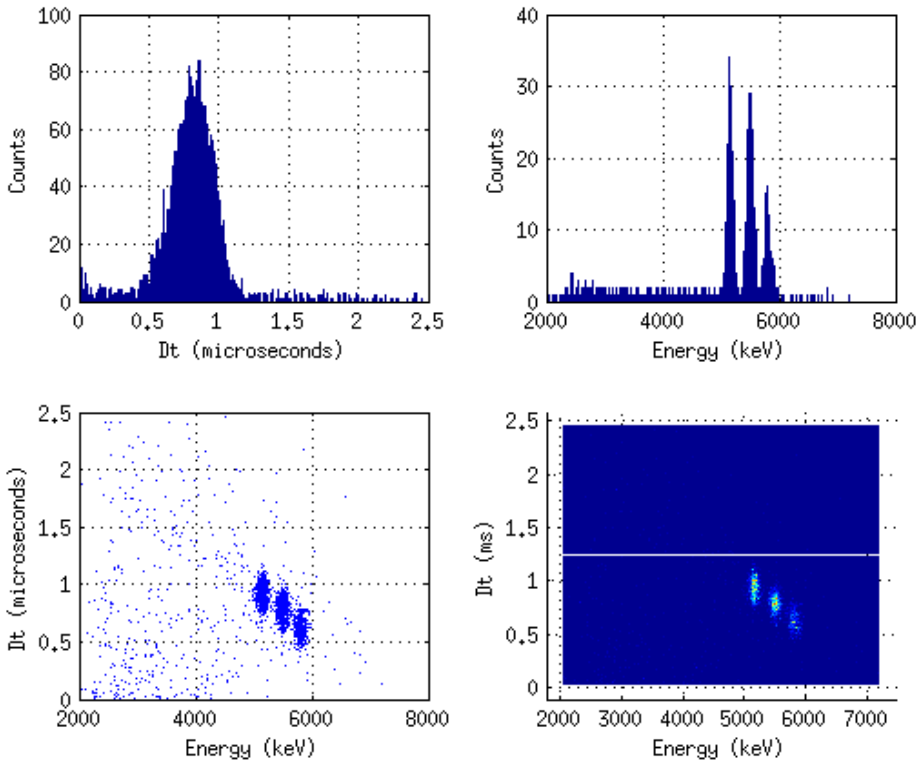


Figure 50: Active cathode timing and energy data for the Tri-nuclide alpha source.

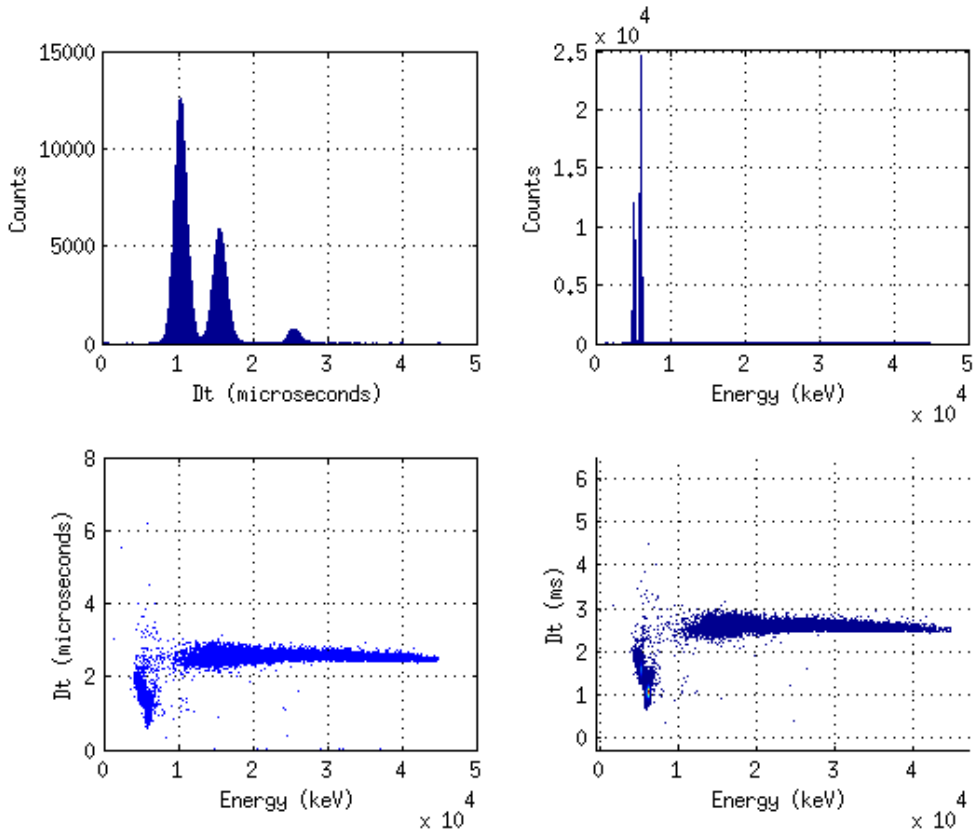


Figure 51: Active cathode timing and energy data for the ^{252}Cf and ^{239}Pu sources, full spectra shown. Due to the great difference in count rate due to alpha vs. fission branching in ^{252}Cf, only the alphas are visible in the counts vs. energy plot.

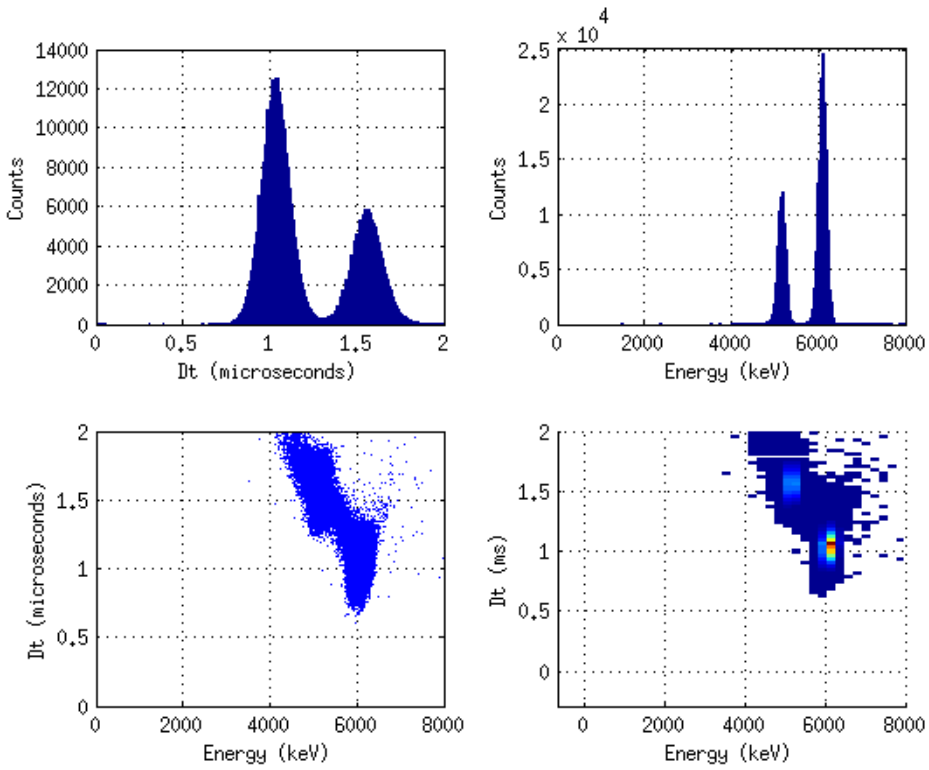


Figure 52: Active cathode timing and energy data scaled to display alpha particle data for ^{252}Cf and ^{239}Pu.

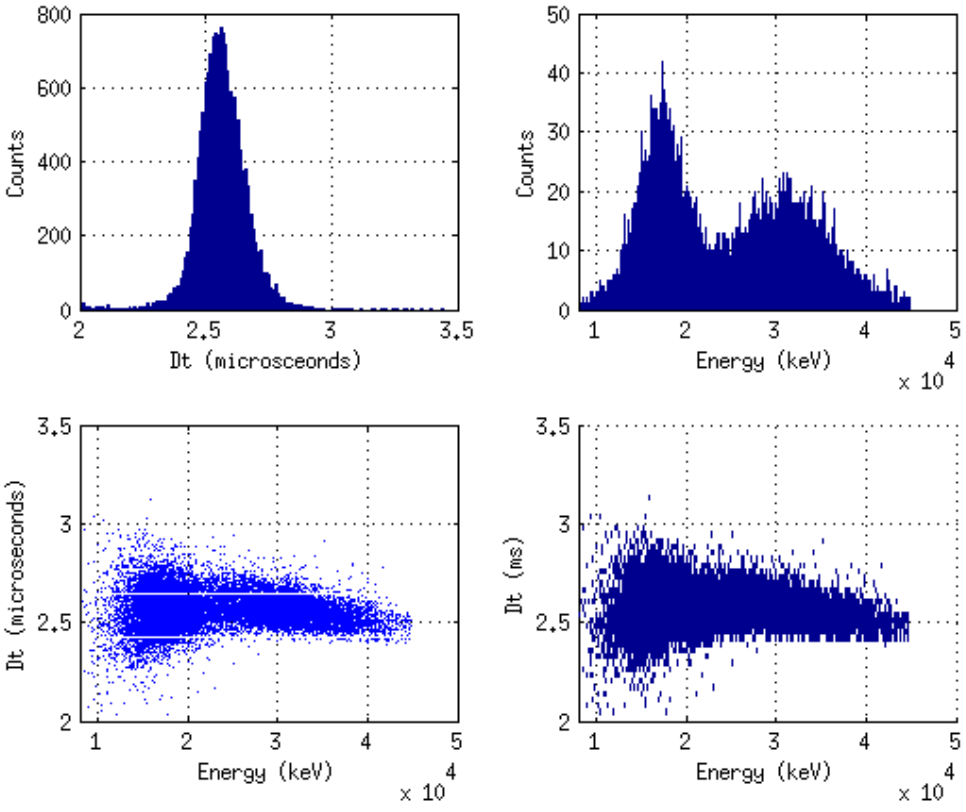


Figure 53: Active cathode timing and energy data scaled to display ^{252}Cf fission fragment data

Chapter 5

Preliminary Analyses of Charge and Mass

5.1 LANL Preliminary Energy Data

Preliminary, independent measurements of both energy and time of flight were taken at the LANSCE facility in Los Alamos in January of 2014. The ionization chamber was run in a non-active cathode mode, wherein the cathode was grounded to reduce noise and simplify setup. A ^{235}U target was placed in the spectrometer target chamber and then hit with a beam of low energy neutrons to produce fission fragments. One of the independent energy measurement results from the IC measurements taken at LANL can be seen in Figure 54.

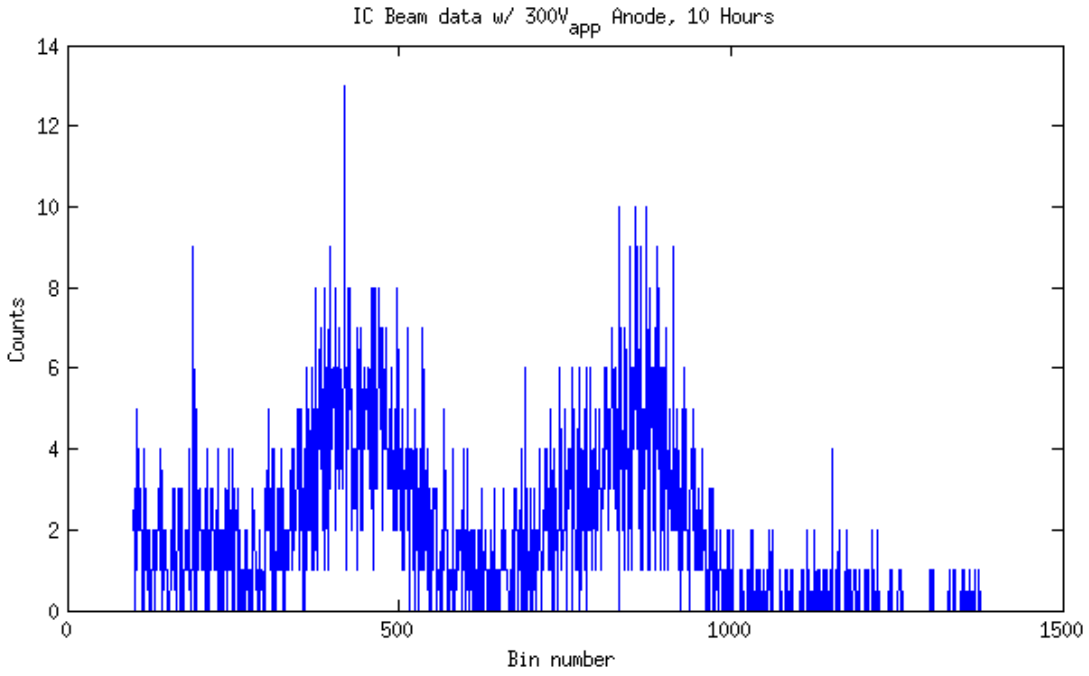


Figure 54: LANSCE preliminary energy measurement results.

5.2 Energy Loss and Straggling

The preliminary analysis of both the charge and mass of an incoming particle is dependent on the kinetic energy of the incoming particle, as dictated by Equations 2 and 12. Equation 12 is restated here for convenience:

$$-\frac{dE}{dx} = \frac{4\pi}{m_e c^2}\frac{nZ^2}{\beta^2}\left(\frac{e^2}{4\pi\varepsilon_o}\right)^2\left[ln\left(\frac{2m_e c^2\beta^2}{I(1-\beta^2)}\right)-\beta^2\right] \qquad \text{[Eq. 12]}$$

Due to the energy dependence of both charge and mass, it is important to understand energy straggling that can affect the energy measurement in the IC. The particles lose energy passing through the carbon foils and window and, due

to the statistical nature, that reduced energy value is also broadened; this is called energy straggling.

SRIM was used to estimate the energy loss and straggling of alpha particles and fission fragments expected to enter the IC. The expected energy loss in the TOF due to the 100 μg/cm^2 carbon foils is expected to be about ~100 keV for alpha particles [Blakeley, 2013] from initial values of 5.1 to 6.1 MeV for the sources used. For the Mylar windows, several thicknesses were examined to determine the energy losses for alpha particles and fission fragments. The SRIM results for the energy losses of several Mylar thicknesses can be seen graphically in Figure 55. For 2.5 μm Mylar, we would expect an average energy loss of ~295 keV, corresponding to about 5.7% energy loss. Other calculations done by Meierbachtol et al. have shown energy losses at 21% for light fission fragments with a straggling of 1.8% [Meierbachtol, 2014b]. These results can be used to help determine the actual kinetic energy of the incoming particle, as well as all uncertainties in energy, and thus mass.

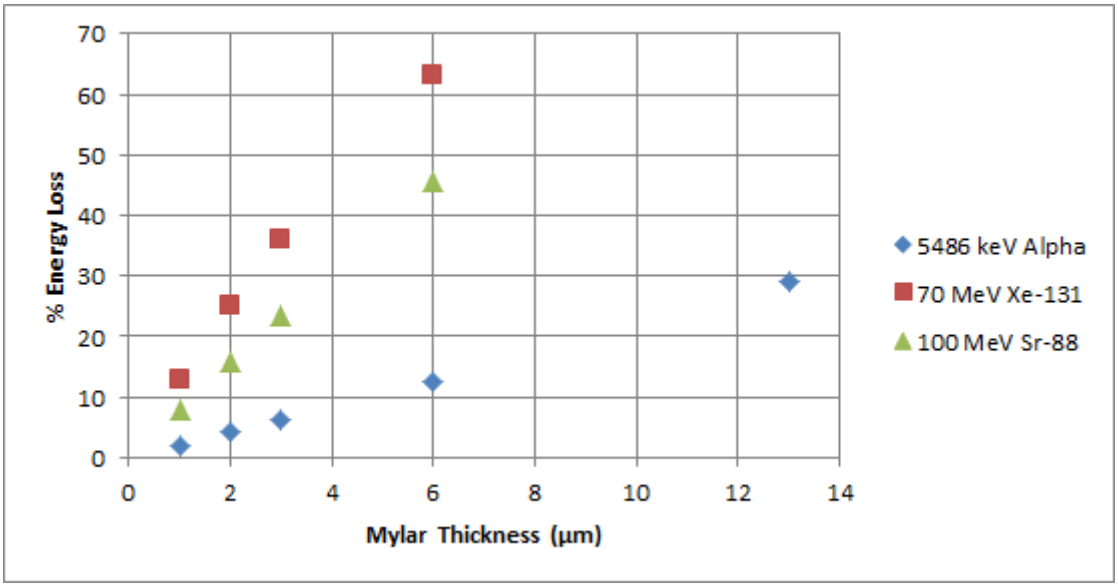


Figure 55: Energy losses in Mylar windows based on SRIM simulations.

Energy loss through Mylar windows was examined experimentally using a silicon surface barrier detector and the tri-nuclide source, with spectra in Figure 56. For 2.5 µm Mylar windows we determined the alpha energy loss to be approximately 280 keV, which is less than the energy loss based on SRIM calculations. The peak broadening can also be seen to increase. The width is based on a combination of straggling coming out of the source, detector response, and straggling in the Mylar; the last factor dominating the change.

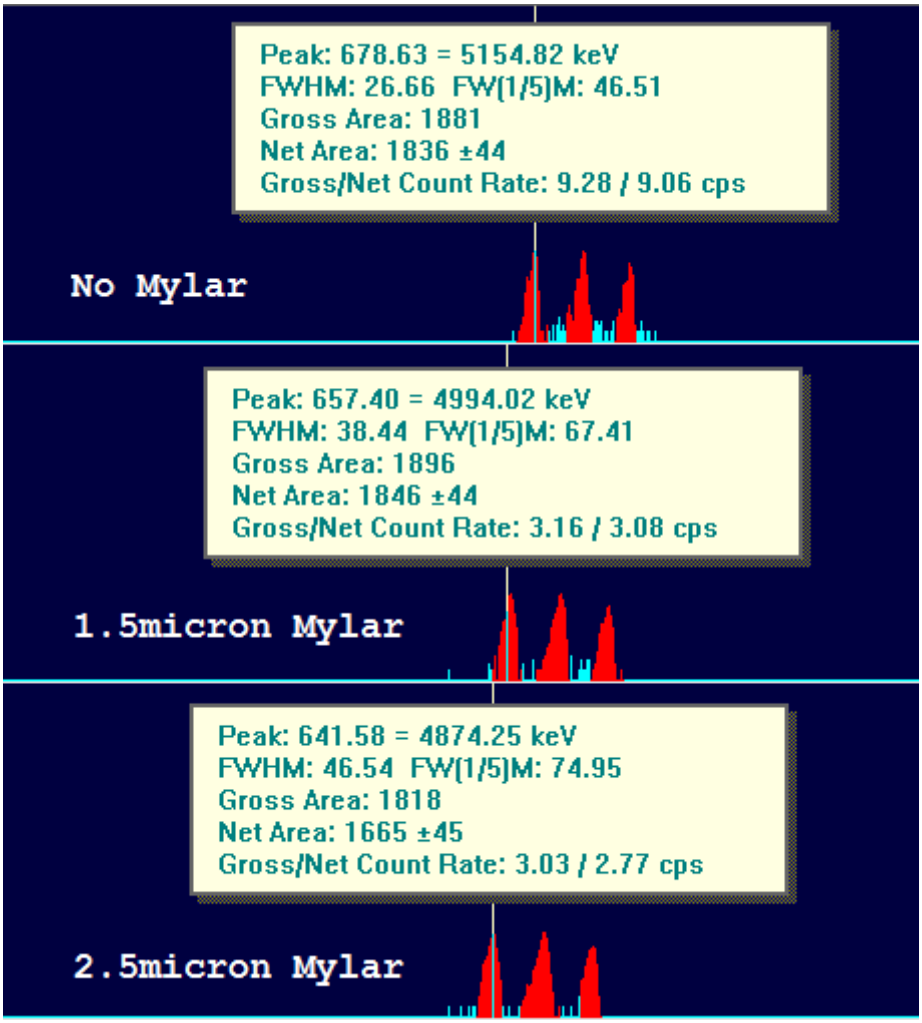


Figure 56: Experimental energy of tri-nuclide source without Mylar (top), with 1.5 μm Mylar (middle), and with 2.5 μm Mylar (bottom).

Degradation in the energy resolution is primarily due to the broadening of the energy peak from passing through the Mylar window. This is evident in the experimental results of the FWHM of the 5156 keV alpha peak for different Mylar thicknesses in Figure 56. We can determine the contribution of the Mylar to the energy broadening by using the following equation:

$$(FWHM_{tot})^2 = \left(FWHM_{Mylar}\right)^2 + (FWHM_{Gas})^2 \qquad \text{[Eq. 15]}$$

Where the total FWHM is made up of contributions from the inherent FWHM of the gas, and the FWHM due to the broadening effects of the Mylar. We can then determine the total standard deviation, σ, by combining Equations 8 and 15:

$$(\sigma_{tot})^2 = \left(\sigma_{Mylar}\right)^2 + (\sigma_{Gas})^2 \qquad \text{[Eq. 16]}$$

We used SRIM [Zeigler, 2008] to simulate what the energy broadening may be for different Mylar thicknesses. The results of these tests were then compared to the data from Figure 56, as seen in Figure 57.

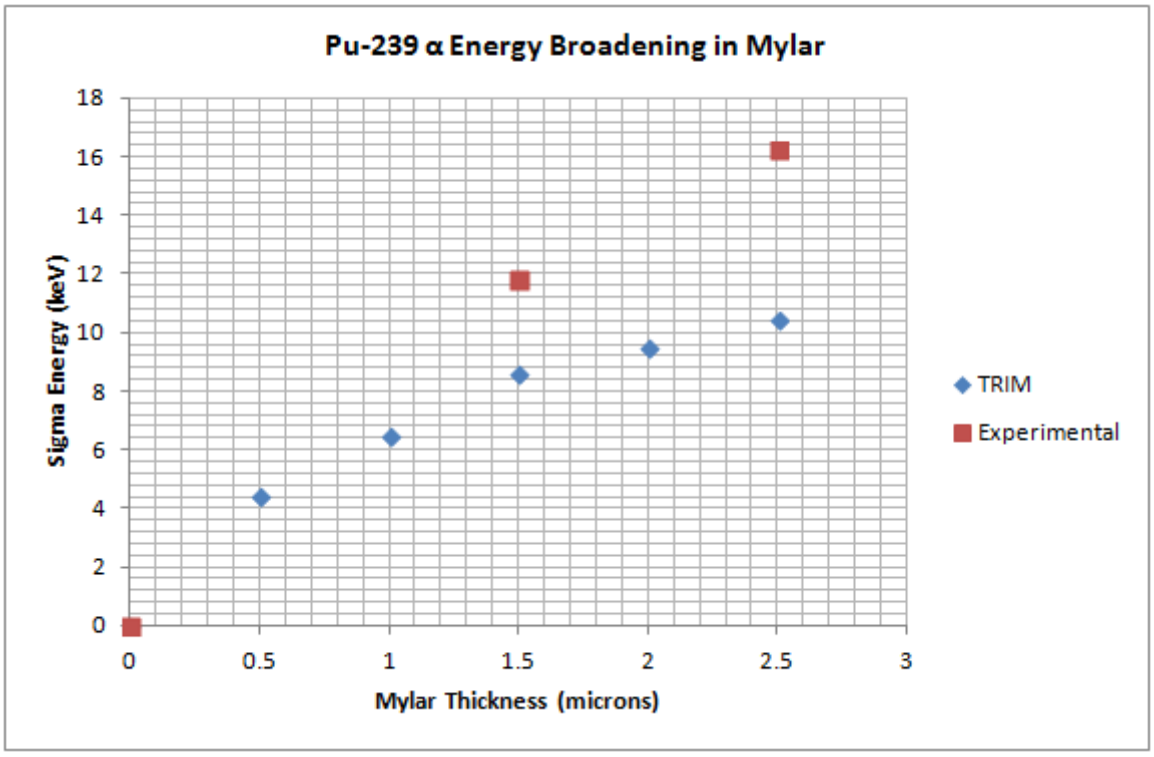


Figure 57: Standard Deviation (energy broadening) of 5156 keV ^{239}Pu alpha particle.

SRIM calculations were then done for both light and heavy fission fragments and compared to the energy broadening for alphas, as seen in Figure 58.

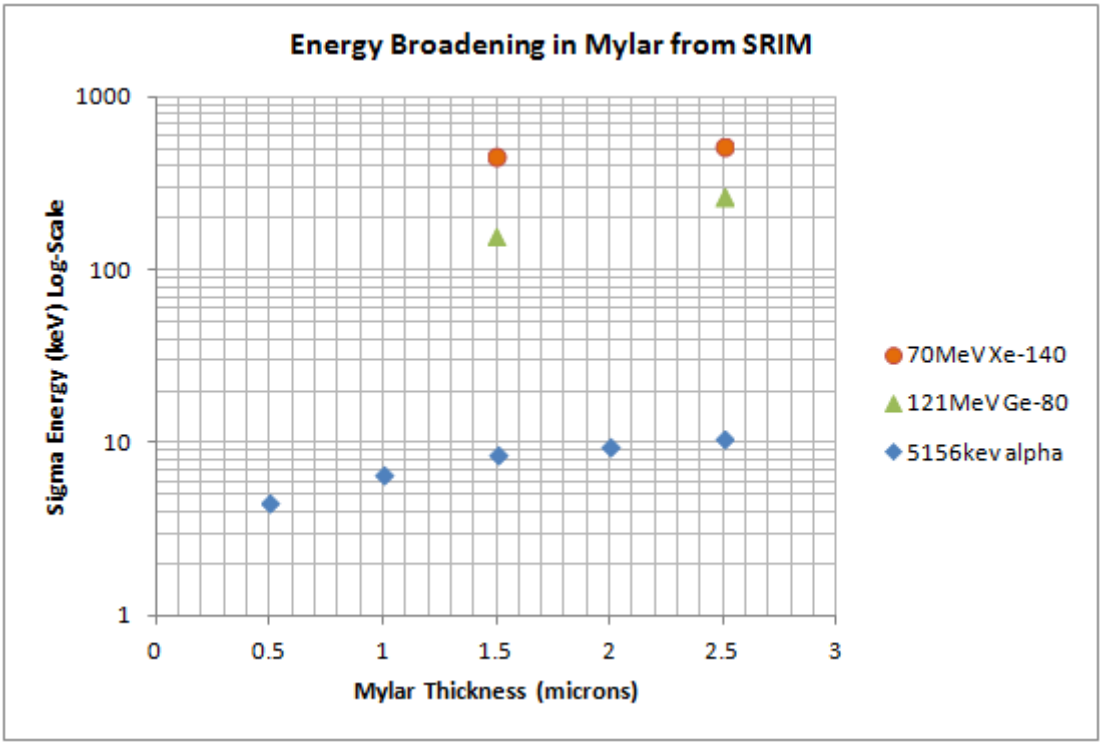


Figure 58: Energy broadening (standard deviation) of alpha particles and fission fragments based on Mylar thickness.

The data from both Figures 57 and 58 can help us to understand the degradation in energy resolution as a function of Mylar thickness.

5.3 Active Cathode Analysis

Following the Bethe equation, the range is a function of velocity and charge. Thus, for the same velocity, particles with different charges will have different

ranges. Unlike Bragg curve analysis which requires approximately 1 MeV/amu or greater, this works down to about 0.5 MeV/amu and will give information on heavy fission fragments.

Expected alpha particle drift times were calculated based on ranges simulated with SRIM for a given pressure and expected electron drift velocities based on E/P. Due to the small pressure variation, and thus electron velocity variation, in our experimental system, plots can be seen in Figure 59. These drift time plots can be used to determine whether or not our experimental data is reasonable, as the pressure drift may dramatically shift the value of E/P, thus shifting the value of the drift velocity. Figure 59 relates different alpha particle energies, and thus different penetration depths, to different Δt values over a range of electron drift velocities.

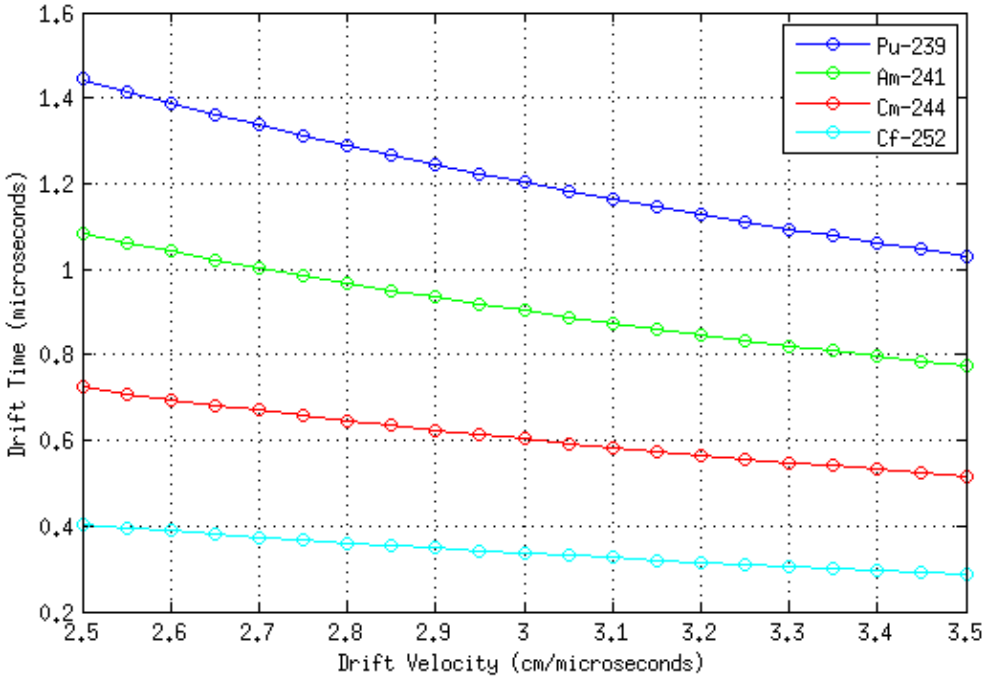


Figure 59: Active cathode drift time plot for alphas in P-10 gas at a pressure of 300 Torr with varying drift velocity.

For the purposes of the analysis done on our experimental data, the drift velocity was assumed to be at the maximum literature value for P-10 gas, this corresponds to a drift velocity of 3.45 cm/μs [Khryachkov, 2003]. Based on this value, the range of the incoming particle can be determined based on Equation 12 from Section 2.5. Experimental results of the active cathode method for particle range measurement can be seen in Figure 60.

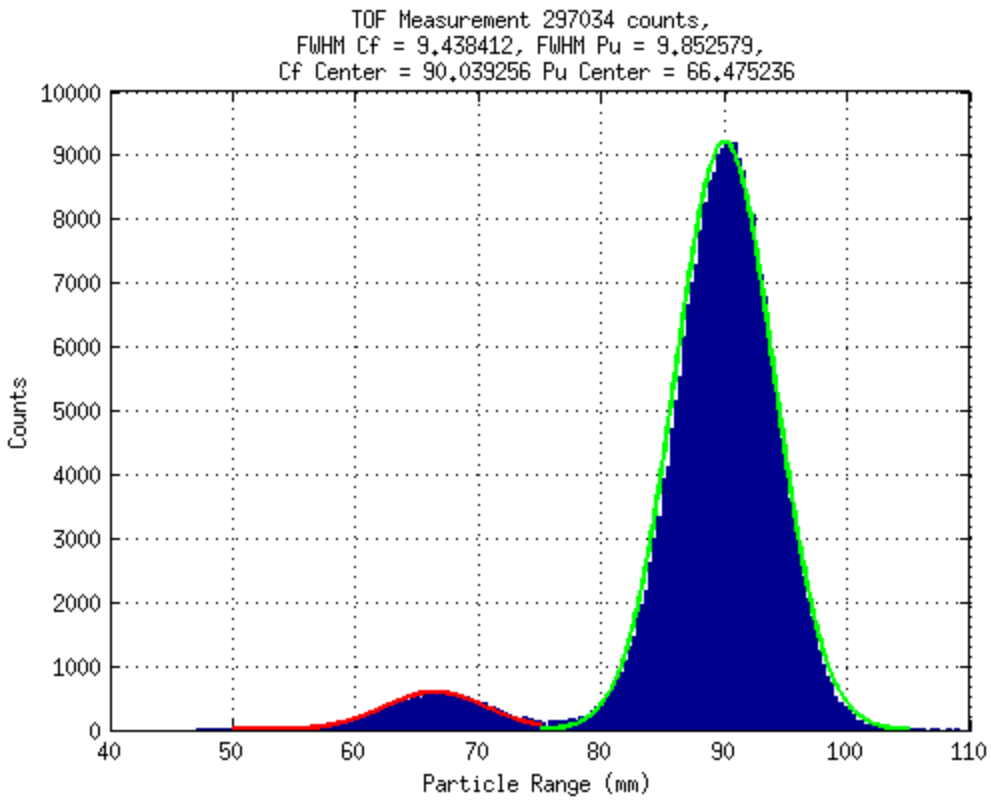


Figure 60: Alpha particle experimental range data based on maximum drift velocity (v_d = 3.45 cm/μs) for alphas in P-10 gas at approximately 300 Torr.

The expected value for particle range of ^{252}Cf alphas is approximately 130 mm at a pressure of 300 Torr, and the expected range of ^{239}Pu alphas is approximately 101 mm at a pressure of 300 Torr, as depicted in Figure 45. Our experimental data in Figure 60 shows the particle range of ^{252}Cf alphas at approximately 66.5 mm at a pressure of 300 Torr, and the range of ^{239}Pu alphas at approximately 90.0 mm at a pressure of 300 Torr. The assumption of a 3.45 cm/μs drift velocity, combined with the variation in internal pressure due to the PID gas controller, explains the discrepancy between expected values and experimental values.

The results of the active cathode range method for fission fragments can be seen in Figure 61. The light and heavy fragments were easily separated in the data based on their energies, and are presented here overlapped with different curves. Here we see the range is much shorter than that of alpha particles, as we would expect from our SRIM calculations. The IC pressure was chosen to be high enough to measure alpha particles, and to avoid "ranging out" near the end length of the active region of the IC, but then the fission fragments stop close to the cathode. With the longer drift distances towards the Frisch grid for electrons from incident fission fragment ionization, there is also more uncertainty in the timing values and thus range determination. Future tests must be performed at lower pressures appropriate for spreading out the ranges of fission fragments.

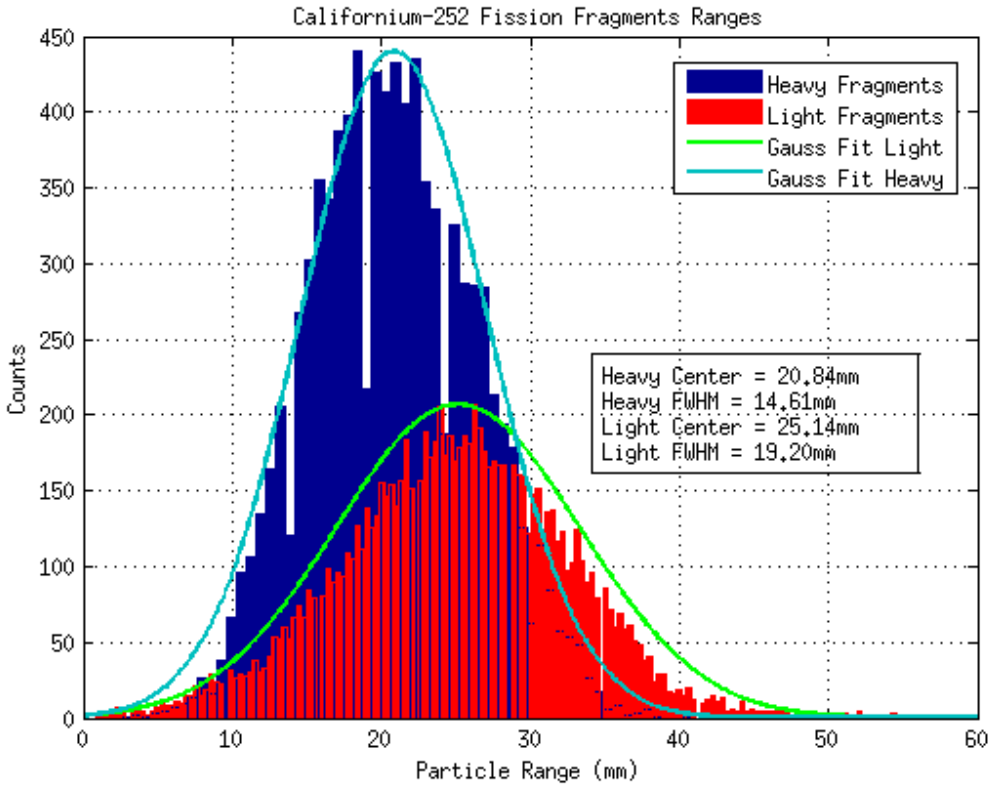


Figure 61: Experimental range plot for ^{252}Cf fission fragments, assuming a maximum drift velocity of 3.45 cm/μs at a pressure of approximately 300 Torr.

5.4 Preliminary Calculations of Mass

Expected energy losses are different depending on the energy of the incoming particle. For the entire spectrometer, from TOF through Mylar windows, we can use the following equation to describe the full energy loss:

$$\Delta E_{tot} = \left(\Delta E_{Mylar}\right) + 2 * \left(\Delta E_{Carbon}\right) + \left(\Delta E_{Target}\right) \qquad \text{[Eq. 17]}$$

Where ΔE_{carbon} is nearly the same for the first and second carbon foil for the fast moving particles, and there is some energy loss leaving the target. Some effects common to the IC and TOF may be ignored in mass determination. Through the

use of SRIM, we estimated the total energy loss for 5156 keV alphas to be approximately 447.4 keV from TOF through IC. Experimentally, the energy loss of a 5156 keV alpha through the carbon foils and Mylar is approximately 480 keV, based on previous experimental values from Figure 55 and data from Blakeley [Blakeley, 2013].

The TOF, and thus velocity, is measured after energy loss through the first carbon foil, as well as the energy loss in the target itself. These common factors can be ignored in determining mass, but the measured IC energy must be corrected due to losses from the second carbon foil and the IC window. The full experimental equation for calculation of particle mass, including the effects of energy loss, can be described by the following:

$$m = 2\frac{(E+\Delta E_{Carbon}+\Delta E_{Mylar})}{(\frac{L}{t_2-t_1})^2} \qquad \text{[Eq. 18]}$$

Experiments were run with ^{252}Cf and ^{239}Pu sources using the combined, correlated spectrometer, which resulted in TOF velocity data and IC energy data. The data from the IC and TOF were time stamped and correlated particle by particle to extract mass. The mass results of the full spectrometer data can be seen in Figure 62 for alpha particles and Figure 63 for fission fragments.

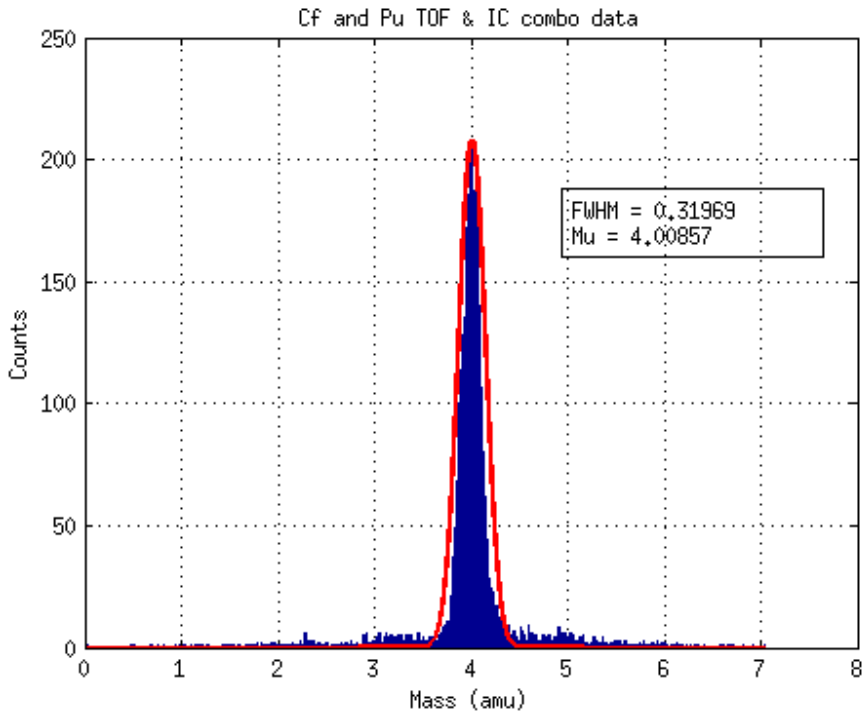


Figure 62: Mass plot for ^{252}Cf and ^{239}Pu alphas.

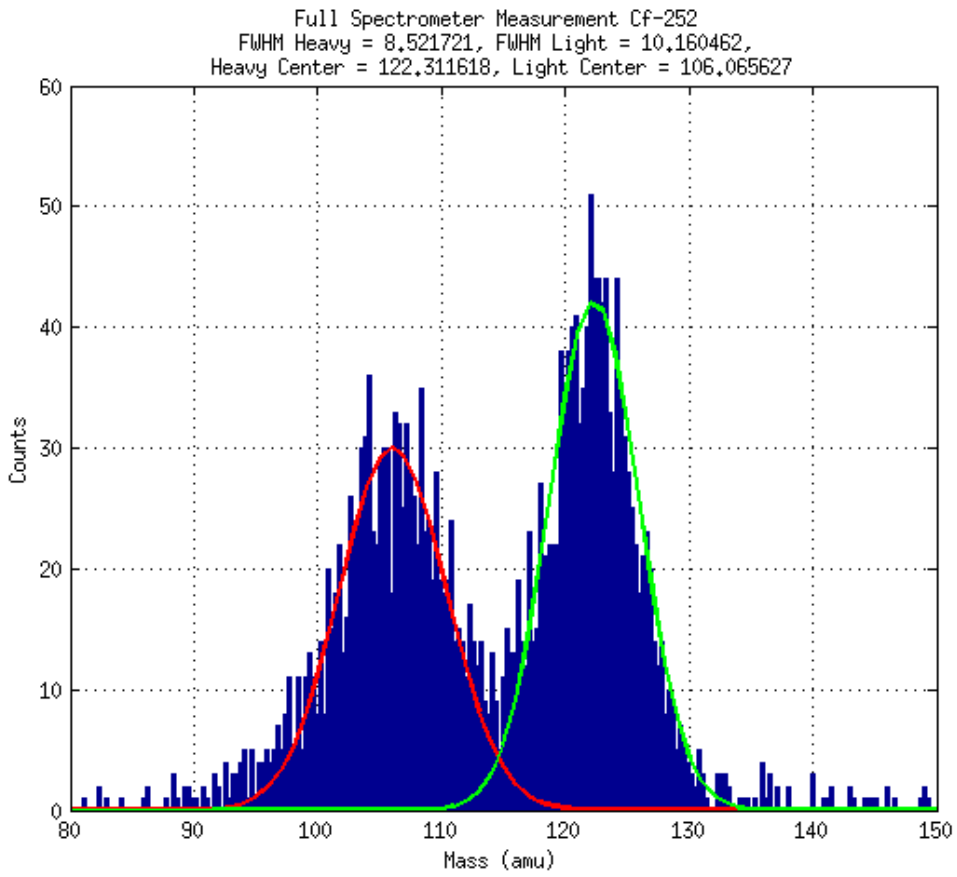


Figure 63: Mass plot for fission fragments.

From Figure 62 we see that the mass of alpha particles is measured as 4.0 with a FWHM of 0.3 amu. This is exactly what we would expect to achieve based on our calibrated TOF time measurement and IC energy measurement. From Figure 63 we see that the mass of light fission fragments is measured as 106.1 amu from our spectrometer, this is close to the literature value of 106.0 amu from Schmitt. However, we measured the heavy fission fragment mass as 122.3 amu which is not close to the literature value of 141.9 amu from Schmitt [Schmitt, 1966]. One

consideration is the different energy loss of heavy (and thus higher Z) fragments vs. lighter (and lower Z) fragments. Another is that heavier particles have a both a lower velocity and a higher charge and thus ionize more densely, they have a higher LET. This increases the portion of recombination, leading to a larger pulse height defect for heavier fragments. The particle-by-particle measurements and correlations are successful, though further calibration and corrections must be performed.

Chapter 6

Conclusions & Future Work

The UNM fission fragment spectrometer development is part of a multi-year effort with LANL with the goal of high resolution fission fragment measurements. A high energy resolution ionization chamber with an active cathode was successfully built for use in fission fragment spectroscopy. Along with improvements upon the entire UNM fission fragment spectrometer, there are also several changes and additions that need to be done on the ionization chamber in order to improve the energy resolution, as well as the range measurement. A summary of accomplishments in each subsection is followed by suggestions for future improvements.

6.1 Combined Spectrometer and Window

A window structure holding 2.5 μm thick Mylar was designed, built, tested, and implemented into the spectrometer. The window has been successfully electrically isolated from the outer vacuum chamber walls of the IC. The 2.5 μm window has been shown to have an average alpha energy loss of approximately 295 keV, corresponding to about 5.7% energy loss; this was verified experimentally for alpha particles. The energy loss for light fission fragments is assumed to be approximately 21% with a straggling of 1.8% [Meierbachtol, 2014b].

As shown experimentally, the 2.5 μm Mylar windows were chosen to prevent failure at pressures not exceeding 300 Torr. Switching to isobutane gas may allow for thinner windows to be used in the future, thus reducing energy straggling and losses. Another window material that our collaborators at LANL are using, silicon nitride (SiN), does not have noticeable leakage, even for much thinner windows. SiN windows are extremely fragile and we are watching their experimental developments, specifically their handling and mounting techniques, before upgrading. The energy straggling is expected to be reduced by switching to SiN windows [Mierbachtol, 2014a; Döbeli, 2004].

6.2 Energy Measurement

An energy resolution of 3-4% for alpha particles (implying 1-2% for fission fragments) was achieved with this ionization chamber running at a low chamber pressure of 300 Torr with P-10 gas. At higher chamber pressures (600 Torr +), we achieved an energy resolution of < 1.5%, which is comparable to that of the previous IC iteration done by Mader [Mader, 2013]. Based on lateral measurements, we found that there was little effect on the energy resolution if the incoming particle entered the chamber from different lateral positions, away from the IC central axis.

Improvement on the energy resolution at low pressures will still need to be done to achieve the one amu mass resolution requirement for the entire spectrometer. The ionization chamber has been characterized for alpha particles, which are at much lower energies and have lower masses than that of fission fragments. Characterization experiments, such as those in Section 4, must be done for fission fragments in order to improve their energy resolution.

6.3 Range Measurement

Uncalibrated range measurements of alpha particles and fission fragments inside of the ionization chamber using an active cathode were successfully

demonstrated. The uncertainty in the value of the drift velocity contributed to the lack of calibration for range measurements. The FWHM of range measurements was measured to be around 10 mm for alphas, 15 mm for heavy fragments, and 20 mm for light fragments.

Further work on characterizing and improving the ionization chamber for range measurements will be needed for proper calibration, especially for measurement of fission fragments. Calibration of range measurements can be accomplished through timing calibration with known sources and a known signal processing delay and sampling time.

6.4 Spectrometer Arms

The UNM fission fragment spectrometer has been successfully built as a one-arm design. A significant piece of future work in regards to the entire UNM fission fragment spectrometer is the construction of a second arm. The second arm will enable us to take binary fission fragment coincidence measurements. The full dual arm spectrometer will be tested in the low energy beam line at the Lujan center at LANL to gather correlated binary fragment data in $^{235}U(n,f)$. The full binary measurement will enable us to determine the total kinetic energy of both fragments.

6.5 Chamber Gas

All of the data collected using the ionization chamber was collected using P-10 gas. Another gas commonly used in ionization chamber measurements is isobutane gas [Meierbachtol, 2014a]. Isobutane was mentioned in Section 2 in regards to drift velocity, where its E/P vs. drift velocity curve (Figure 14) has no clear saturation point and increases with increasing E/P. This gas may be more stable in regards to energy centroid peak drift for use in the active cathode design as the slope of the curve is small, meaning that the drift velocity may not deviate as much as it does with P-10 gas. The E/P vs. drift velocity curve for P-10 gas has a maximum velocity point, though it is located on a narrow peak, meaning that deviation from the peak causes a dramatic change in drift velocity, leading to peak drift.

For the future, using isobutane gas may allow for improvements in energy centroid peak drift stability as well as being able to run at lower pressure values. Isobutane gas has a much larger stopping power than that of P-10 gas, meaning that particles stop and ionize in a shorter distance. In our IC we used P-10 gas and determined that running at lower pressures runs the risk of ranging out alpha particles past the active region of the chamber. Though several orders of magnitude more expensive, high purity isobutane gas will allow the use of lower

pressure, which in turn minimizes the risk of Mylar window failure. Lower pressures may also allow us to switch to thinner windows which will help to reduce energy straggling and improve resolution. Isobutane gas has also been shown to have improved energy resolution in comparison to P-10 gas [Adhikari, 2006; Mierbochtol, 2014b].

6.6 Testing Facilities

We used small laboratory sources such as ^{239}Pu and ^{252}Cf in the characterization and design of the UNM fission fragment spectrometer.

For the future, other sources with varying energies will help to fully characterize the spectrometer and help to complete current data sets. For example, the Sandia Ion Beam Laboratory offers the option of using targets to recoil heavy elements (C through Pu) for analysis, or knock off light elements (H through F) for analysis [IBA Sandia, 2014]. The Argonne Tandem Linear Accelerator System (ATLAS) can provide beams of essentially all stable isotopes from protons to uranium, and a variety of light radioactive beams [ATLAS, 2014]. Both of these facilities, along with the Lujan center at LANL, offer a large variety of calibration, testing, and data collection opportunities for the UNM spectrometer.

Bibliography

[Adhikari ,2006] Adhikari, S.; Basu, C.; et al., 2006. *Performance of an Axial Gas Ionization Detector*. IEEE Transactions on Nuclear Science, August, 53(4), pp. 1-19.

[Ahmed, 2007] Ahmed, S. N., 2007. *Physics and Engineering of Radiation Detection*. 1st ed. San Diego: Elsevier.

[Arnold, 2014] Arnold, C.W.; Tovesson, F.; et al., 2014. *Development of position-sensitive time-of-flight spectrometer for fission fragment research*, ArXiv preprint ArXiv: pp. 1403.1573.

[ATLAS, 2014] "*Argonne Physics Division - ATLAS." Argonne Physics Division - ATLAS*. [Online]. 2014. Available at: http://www.phy.anl.gov/atlas/

[Barna, 2004] Barna, R.; et al., 2004. *PISA – an experiment for fragment spectroscopy at the Internal Beam of COSY: application of an Axial Ionization Chamber*, Nuclear Instruments and Methods in Physics Research A, Volume 519, pp. 610-622.

[Blakeley, 2013] Blakeley, R., 2013. *A Time-of-Flight Spectrometer for Fission Fragment Identification*, M.Sc. Thesis, University of New Mexico, Albuquerque, New Mexico, USA.

[BNL, 1952] Brookhaven National Laboratory. [Online]. 1952. Available at: http://www.nndc.bnl.gov/

[Bocquet, 1988] Bocquet, J. P.; Brissot, R.; Faust, H. R., 1988. *A Large Ionization Chamber for Fission Fragment Nuclear Charge Identification at the Lohengrin Spectrometer*. Nuclear Instruments and Methods in Physics Research A, Volume 267, pp. 466-472

[Boucheneb, 1989] Boucheneb, N.; et al., 1989. *High-Resolution Measurements of Mass, Energy and Nuclear Charge Correlations for Th-229(n,f) with the COSI FAN TUTTE Spectrometer*, Nuclear Physics, A 502, pp. 261-270.

[Brown, 1949] Brown, M. A.; Biondi, S., 1949. *Measurement of Electron-Ion Recombination*, Cambridge: Massachusetts Institute of Technology Research Laboratory of Electronics.

[CAEN, 2014] CAEN 5724 5724A user manual, 24 July 2014, available at www.caen.it

[Döbeli, 2004] Döbeli, M.; Kottler, C.; et al., 2004. *Gas Ionization Chambers with Silicon Nitride Windows for the Detection and Identification of Low Energy Ions*. Nuclear Instruments and Methods in Physics Research B, Volume 219-220, pp. 415-419.

[Gruhn, 1982] Gruhn, C. R.; Binimi, N. M.; et al., 1982. *Bragg Curve Spectroscopy. Nuclear Instruments and Methods*, Volume 196, pp. 33-40.

[Hagiwara, 2008] Hagiwara, M.; Sanami, T.; et al., 2008. *Extension of Energy Acceptance of Bragg Curve Counter at High-Energy End*. Nuclear Instruments and Methods in Physics Research A, Volume 592, pp. 73-79.

[IBA Sandia, 2014] "*Sandia National Laboratories.": Research Facilities: Technology Deployment Centers: Ion Beam Laboratory*. [Online]. 2014. Available at: http://www.sandia.gov/research/facilities/technology_deployment_centers/ion_beam_laboratory.html

[Khryachkov, 2003] Khryachkov, V. A.; Dunaeva, I. V.; et al., 2003. *A Method for Rapid Measurements of Working Gas Properties in a Pulse Ionization Chamber*. Instruments and Experimental Techniques, 46(6), pp. 804-813.

[Knoll, 2000] Knoll, G. F., 2000. *Radiation Detection and Measurement*. 3rd ed. New Jersey: John Wiley & Sons.

[Kozulin , 2008] Kozulin, E. M.; Bogachev, A. A.; et al., 2008. *The CORSET Time-of-Flight Spectrometer for Measuring Binary Products of Nuclear Reactions*. Instruments and Experimental Techniques, 51(1), pp. 44-58.

[Mader, 2013] Mader, D., 2013. *An Ionization Chamber for Fission Fragment Analysis*, M.Sc. Thesis, University of New Mexico, Albuquerque, New Mexico, USA.

[Meierbachtol , 2014a] Meierbachtol, K; Tovesson, F; et al., 2014. *A High Resolution Ionization Chamber for the SPIDER Fission Fragment Detector*, Fission and Properties of Neutron-Rich Nuclei-Proceedings of the Fifth International Conference on ICFN5. Edited by Hamilton Joseph H & Ramayya Akunuri V. Published by World Scientific Publishing Co. Pte. Ltd., 2014. ISBN# 9789814525435, pp. 682-684, Vol. 1

[Meierbachtol, 2014b] Meierbachtol, K. C. *"First Results of Fission Mass Yield Measurements with SPIDER at LANSCE."* FIESTA Workshop. New Mexico, Santa Fe. 12 Sept. 2014. Lecture.

[Oed, 1984] Oed, A.; et al., 1984. *High Resolution Axial Ionization Chamber for Fission Products,* Nuclear Instruments and Methods 225, pp. 508

[Piesert, 1984] Peisert, A.; Sauli, F., 1984. *Drift and Diffusion of Electrons in Gases: A Compilation*. CERN report 84-08.

[Sanami, 2008] Sanami, T.; Hagiwara, M.; et al., 2008. *A Bragg Curve Counter with an Active Cathode to Improve the Energy Threshold in Fragment Measurements*. Nuclear Instruments and Methods in Physics Research A, Volume 589, pp. 193-201.

[Sanami, 2009] Sanami, T.; Hagiwara, M.; et al., 2009. *A Bragg Curve Counter with an Internal Production Target for the Measurement of the Double-Differential Cross-Section of Fragment Production Induced by Neutrons at Energies of Tens of MeV*. Nuclear Instruments and Methods in Physics Research A, Volume 610, pp. 660-668.

[Schmitt, 1966] Schmitt, H.; Neiler, J.; Walter, F., 1966. *"Fragment Energy Correlation Measurements for Cf252 Spontaneous Fission and U235 Thermal-Neutron Fission."* Physical Review 141.3, pp. 1146-160.

[Sharma, 2006] Sharma, S. L.; et al., 2006. *Some studies on the pulse-height loss due to capacitive decay in the detector-circuit of parallel plate ionization chambers*, Nuclear Instruments and Methods in Physics Research Section A Accelerators Spectrometers Detectors and Associated Equipment; 566(2): pp. 540-551.

[Tovesson , 2013] Tovesson, F.; Arnold, C.; et al., 2013. *SPIDER: A new instrument for fission fragment research at the Los Alamos Neutron Science Center*, EPJ Web of Conferences, Vol. 62, pp. 5002, EDP Sciences.

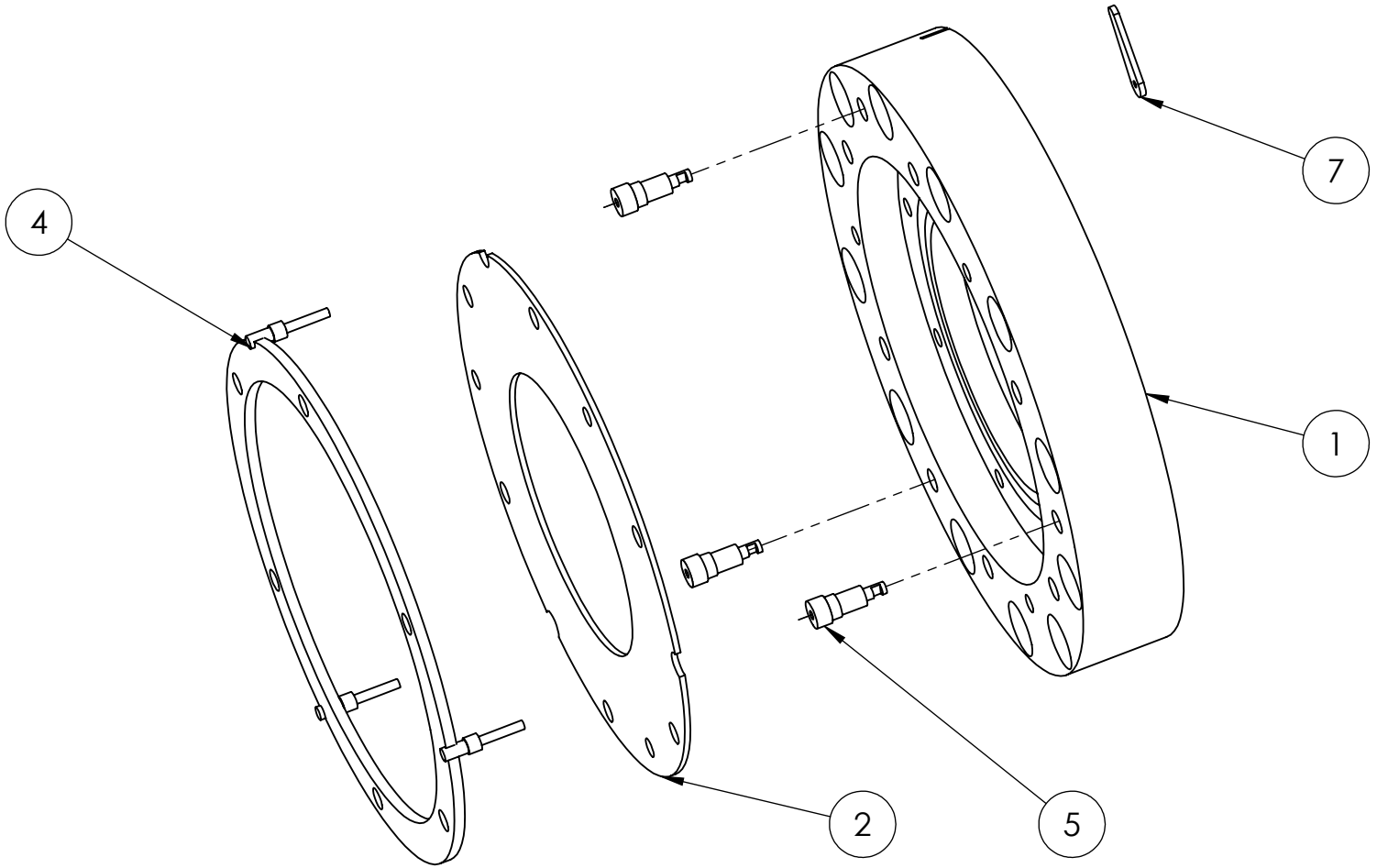
[Turner, 2007] Turner, J. E., 2007. *Atoms, Radiation, and Radiation Protection*. 3rd ed. Weinheim: Wiley-VCH.

[Tyukavkin, 2009] Tyukavkin, A. N.; et al., 2009. "*Measuring the Nuclear Charge of Fission Fragments Using a Large Ionization Chamber—part of the Double-arm Time-of-flight Spectrometer*." Instruments and Experimental Techniques 52.4: 508-18.

[Ziegler, 2014] Ziegler, J. F., *Particle Interactions with Matter*. [Online]. 2014. Available at: www.SRIM.org.

Appendix A

A.1 IC Assembly Design Drawings



ITEM NO.	DESCRIPTION	QTY.
1	Teflon	1
2	Cathode	1
4	plugring	1
5	BNCminijack	3
7	TeflonInset	1

SolidWorks Student Edition.
For Academic Use Only.

DIMENSIONING AND TOLERANCING PER ASME Y14.5 1994

DIMENSIONS ARE IN INCHES UNLESS OTHERWISE SPECIFIED

TOLERANCES ARE AS FOLLOWS UNLESS OTHERWISE SPECIFIED

x.x = ±0.03
x.xx = ±0.01
x.xxx = ±0.005
Angles = ±2°

MATERIAL N/A

FINISH N/A

Mechanical Engineering, Mechatronic Engineering, & Manufacturing Technology
California State University, Chico

Template version 060411

	NAME	DATE
DRAWN	L. Heffern	140721
CHECKED		
ENG APPR		
MFG APPR		
Q A		

TITLE
Window Plug Assembly

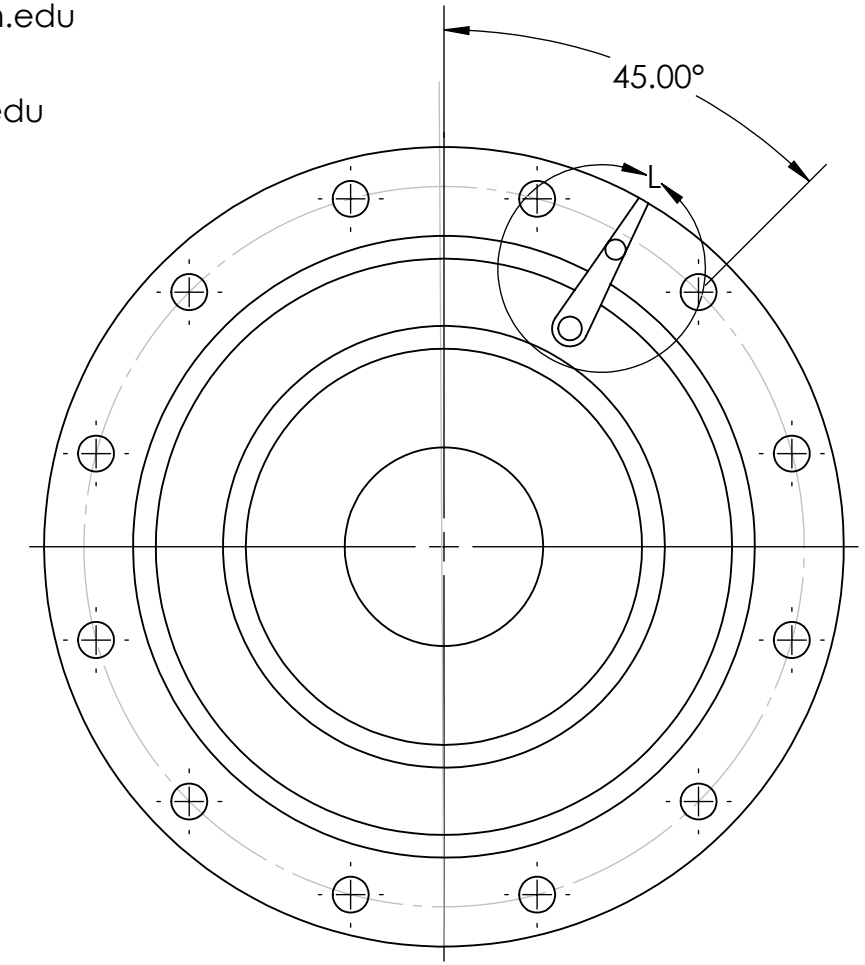
SIZE A | DWG NO SU14-007-A01M-A1 | REV –

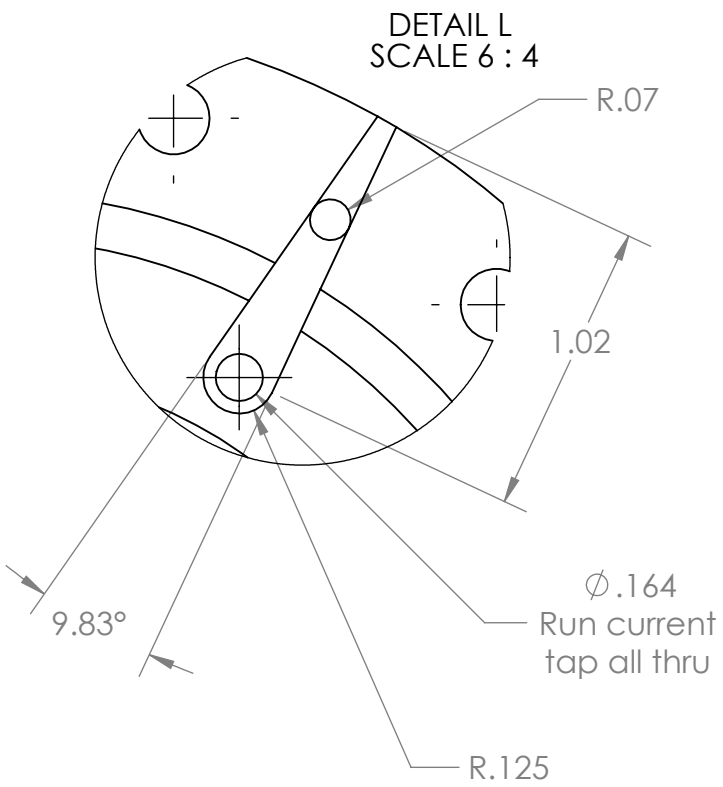
SCALE 1:5 | SHEET 1 OF 1

5 4 3 2 1

D C B A

Contact:
Lena Heffern
Lheffern@unm.edu
or
Adam Hecht
Hecht@unm.edu



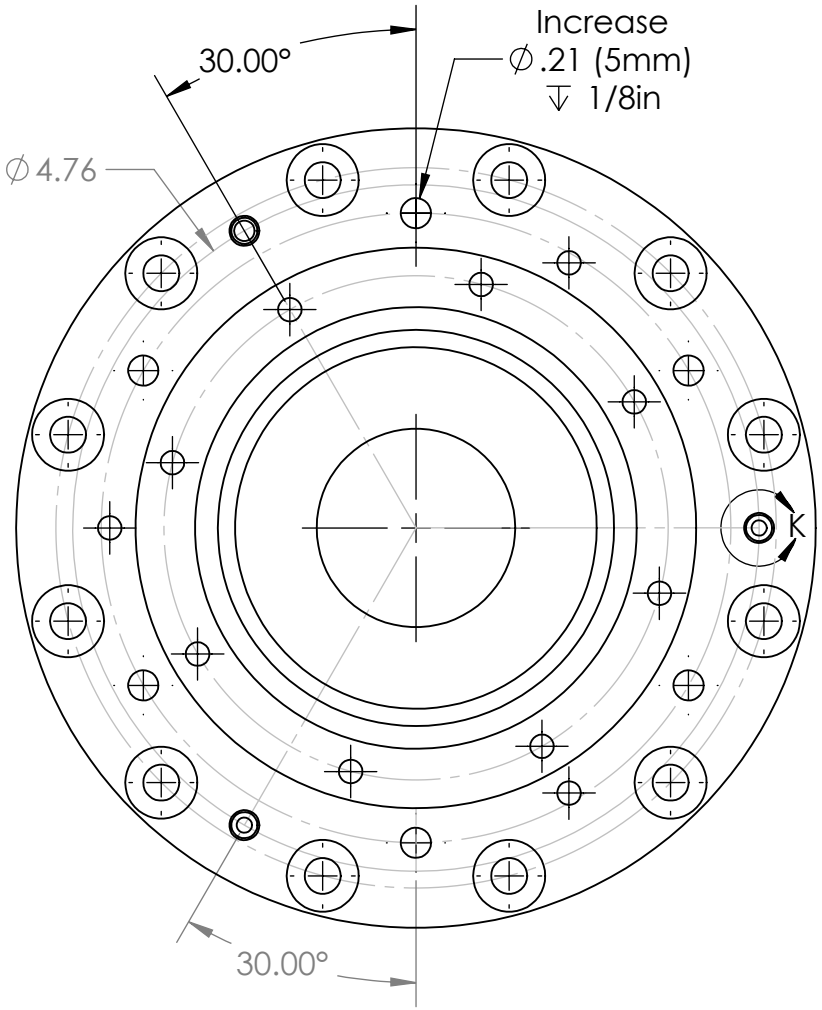


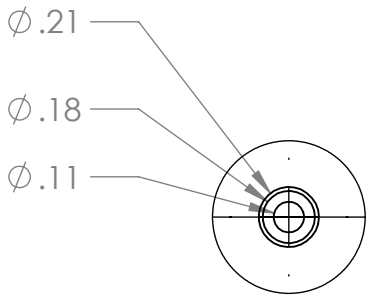
SolidWorks Student Edition.
For Academic Use Only.

DIMENSIONING AND TOLERANCING PER ASME Y14.5 1994 DIMENSIONS ARE IN INCHES UNLESS OTHERWISE SPECIFIED TOLERANCES ARE AS FOLLOWS UNLESS OTHERWISE SPECIFIED x.x = ±0.03 x.xx = ±0.01 x.xxx = ±0.005 Angles = ±2°	**Department of Chemical & Nuclear Engineering** **University of New Mexico** *Template version 060411*	
MATERIAL: Teflon FINISH:	NAME / DATE DRAWN: L. Heffern 140721 CHECKED: ENG APPR: MFG APPR: Q A:	TITLE: **Teflon Disk** SIZE: A DWG NO: SU14-007-A01M-P1 REV: 13 SCALE 3:4 SHEET 1 OF 6

5 4 3 2 1

D C B A





DETAIL K
SCALE 6 : 4

SolidWorks Student Edition.
For Academic Use Only.

DIMENSIONING AND TOLERANCING PER ASME Y14.5 1994 DIMENSIONS ARE IN INCHES UNLESS OTHERWISE SPECIFIED TOLERANCES ARE AS FOLLOWS UNLESS OTHERWISE SPECIFIED x.x = ±0.03 x.xx = ±0.01 x.xxx = ±0.005 Angles = ±2°	**Department of Chemical & Nuclear Engineering** **University of New Mexico** *Template version 060411*		
MATERIAL: Teflon		NAME	DATE
FINISH	DRAWN	L. Heffern	140721
	CHECKED		
	ENG APPR		
	MFG APPR		
	Q A		

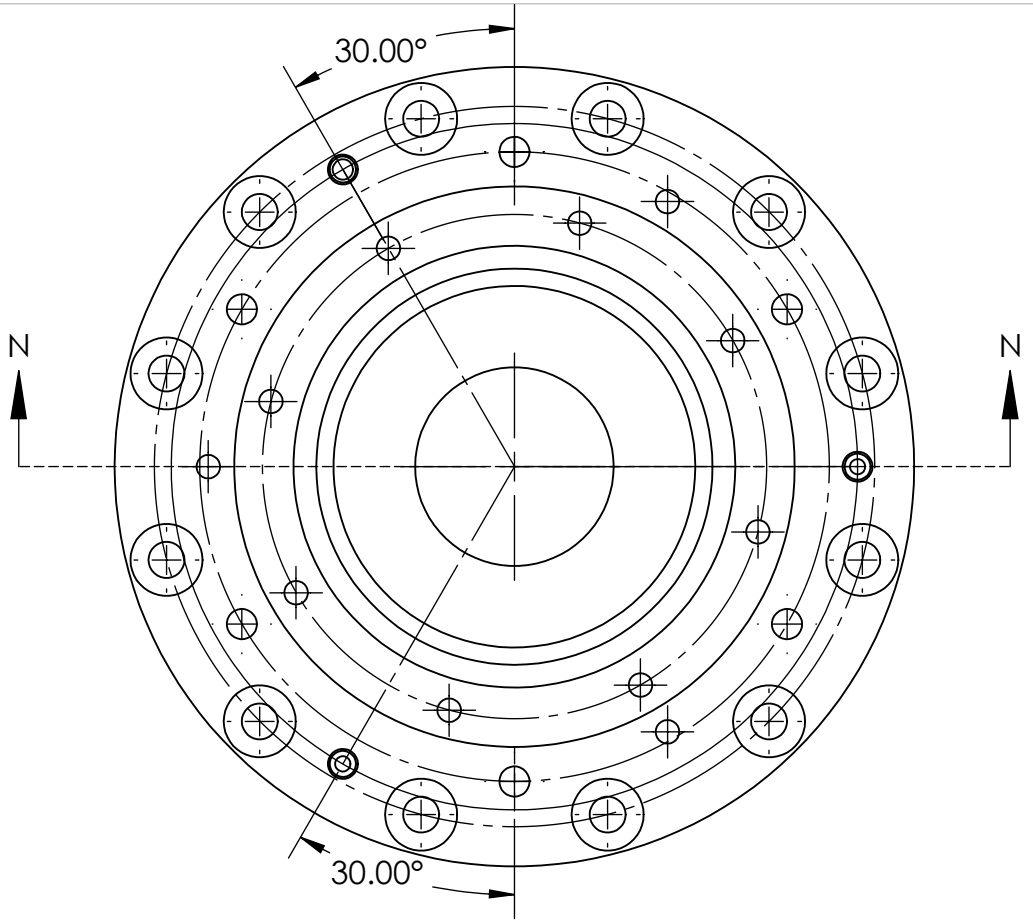
TITLE: **Teflon Disk**

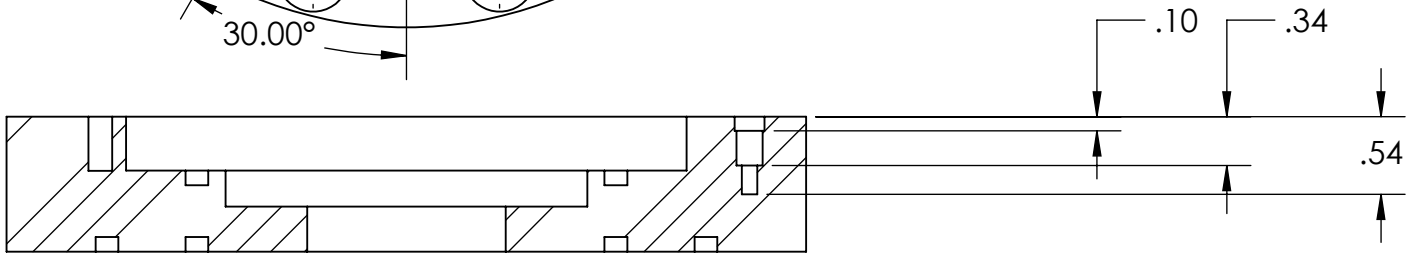
SIZE	DWG NO	REV
A	SU14-007-A01M-P1	13

SCALE 3:4 SHEET 2 OF 6

5 4 3 2 1

D C B A





SECTION N-N

SolidWorks Student Edition.
For Academic Use Only.

DIMENSIONING AND TOLERANCING PER ASME Y14.5 1994

DIMENSIONS ARE IN INCHES UNLESS OTHERWISE SPECIFIED

TOLERANCES ARE AS FOLLOWS UNLESS OTHERWISE SPECIFIED

x.x = ±0.03
x.xx = ±0.01
x.xxx = ±0.005
Angles = ±2°

MATERIAL: Teflon

FINISH:

Department of Chemical & Nuclear Engineering
University of New Mexico

Template version 060411

	NAME	DATE
DRAWN	L. Heffern	140721
CHECKED		
ENG APPR		
MFG APPR		
Q A		

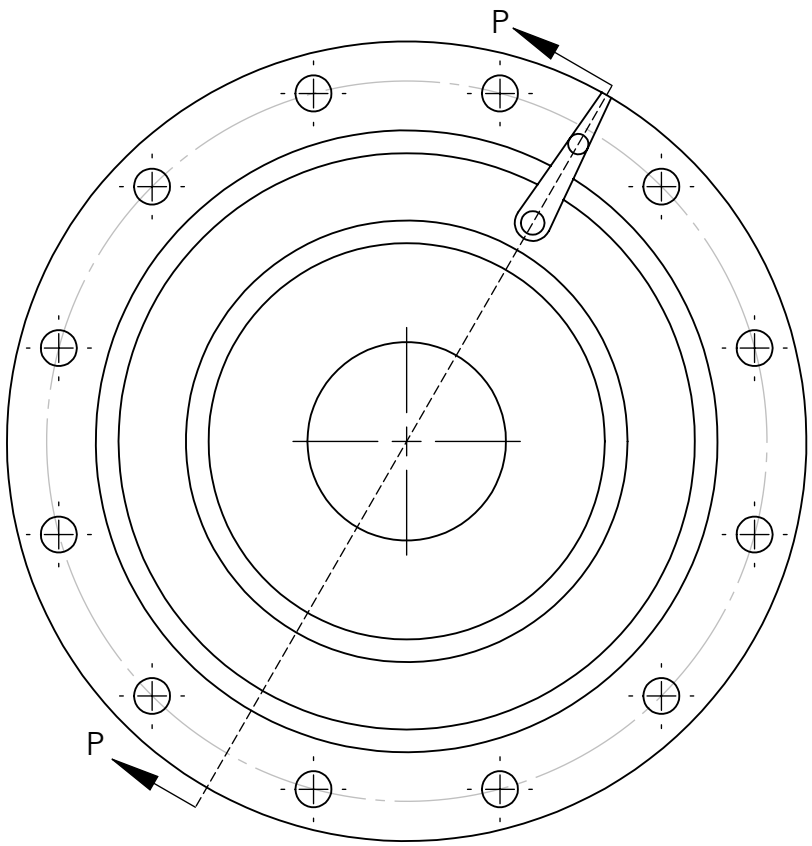
TITLE: **Teflon Disk**

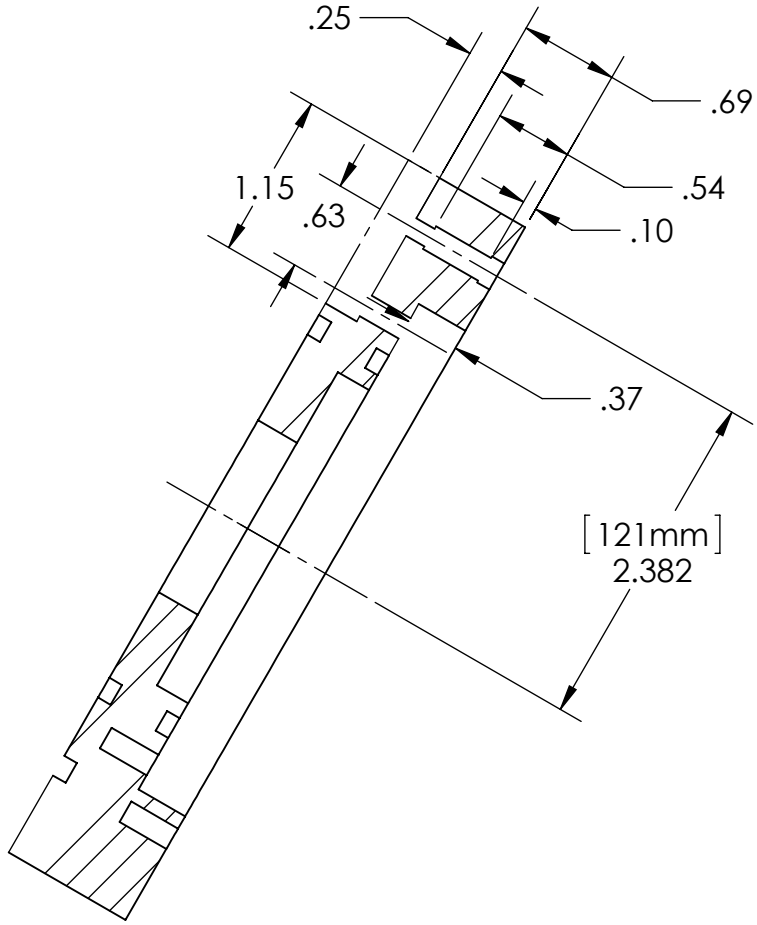
SIZE A | DWG NO SU14-007-A01M-P1 | REV 13

SCALE 3:4 | SHEET 3 OF 6

5 4 3 2 1

D C B A





SECTION P-P

SolidWorks Student Edition.
For Academic Use Only.

DIMENSIONING AND TOLERANCING PER ASME Y14.5 1994

DIMENSIONS ARE IN INCHES UNLESS OTHERWISE SPECIFIED

TOLERANCES ARE AS FOLLOWS UNLESS OTHERWISE SPECIFIED

x.x = ±0.03
x.xx = ±0.01
x.xxx = ±0.005
Angles = ±2°

MATERIAL: Teflon

FINISH:

Department of Chemical & Nuclear Engineering
University of New Mexico

Template version 060411

	NAME	DATE
DRAWN	L. Heffern	140721
CHECKED		
ENG APPR		
MFG APPR		
Q A		

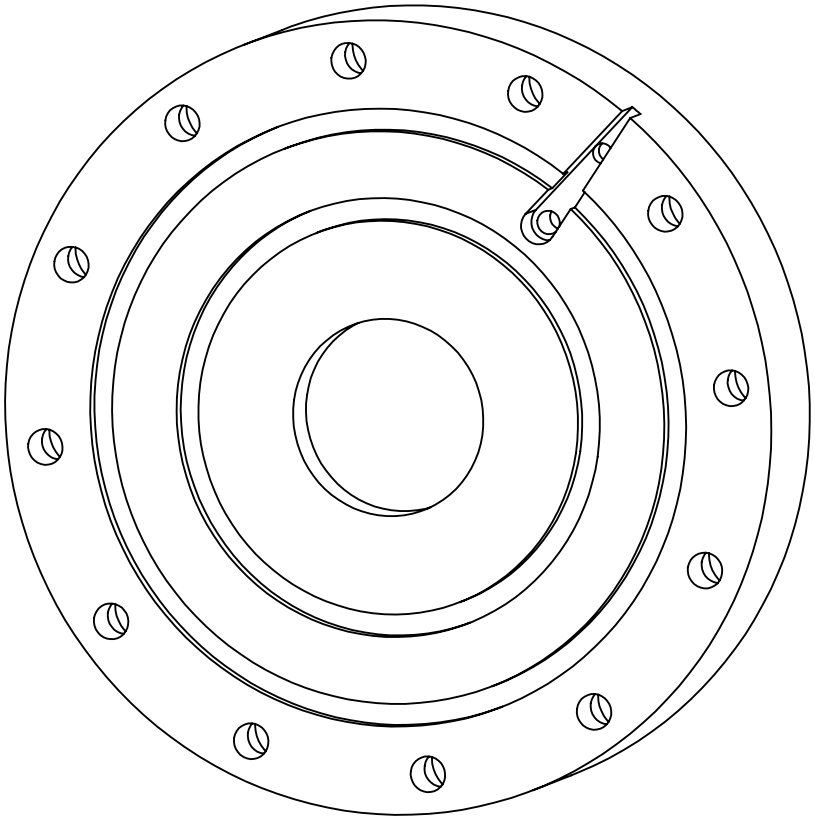
TITLE: **Teflon Disk**

SIZE: A | DWG NO: SU14-007-A01M-P1 | REV: 13

SCALE 3:4 | SHEET 4 OF 6

5 4 3 2 1

D C B A



SolidWorks Student Edition.
For Academic Use Only.

DIMENSIONING AND TOLERANCING PER ASME Y14.5 1994 DIMENSIONS ARE IN INCHES UNLESS OTHERWISE SPECIFIED TOLERANCES ARE AS FOLLOWS UNLESS OTHERWISE SPECIFIED x.x = ±0.03 x.xx = ±0.01 x.xxx = ±0.005 Angles = ±2°	**Department of Chemical & Nuclear Engineering** **University of New Mexico** *Template version 060411*		
MATERIAL: Teflon		NAME	DATE
FINISH	DRAWN	L. Heffern	140721
	CHECKED		
	ENG APPR		
	MFG APPR		
	Q A		

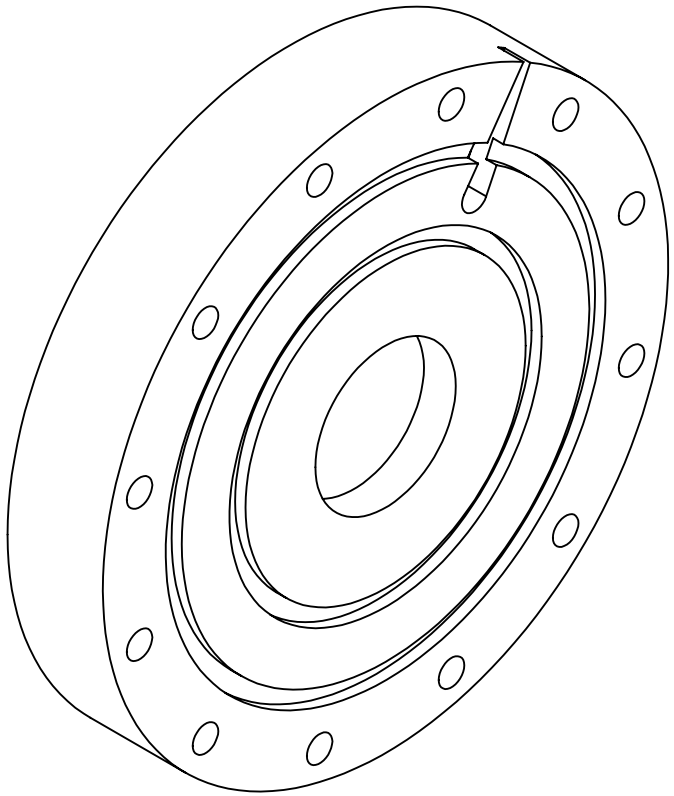
TITLE: **Teflon Disk**

SIZE	DWG NO	REV
A	SU14-007-A01M-P1	13

SCALE 3:4 SHEET 5 OF 6

5 4 3 2 1

D C B A



SolidWorks Student Edition.
For Academic Use Only.

DIMENSIONING AND TOLERANCING PER ASME Y14.5 1994

DIMENSIONS ARE IN INCHES UNLESS OTHERWISE SPECIFIED

TOLERANCES ARE AS FOLLOWS UNLESS OTHERWISE SPECIFIED

x.x = ±0.03
x.xx = ±0.01
x.xxx = ±0.005
Angles = ±2°

MATERIAL: Teflon

FINISH:

Department of Chemical & Nuclear Engineering
University of New Mexico

Template version 060411

	NAME	DATE
DRAWN	L. Heffern	140721
CHECKED		
ENG APPR		
MFG APPR		
Q A		

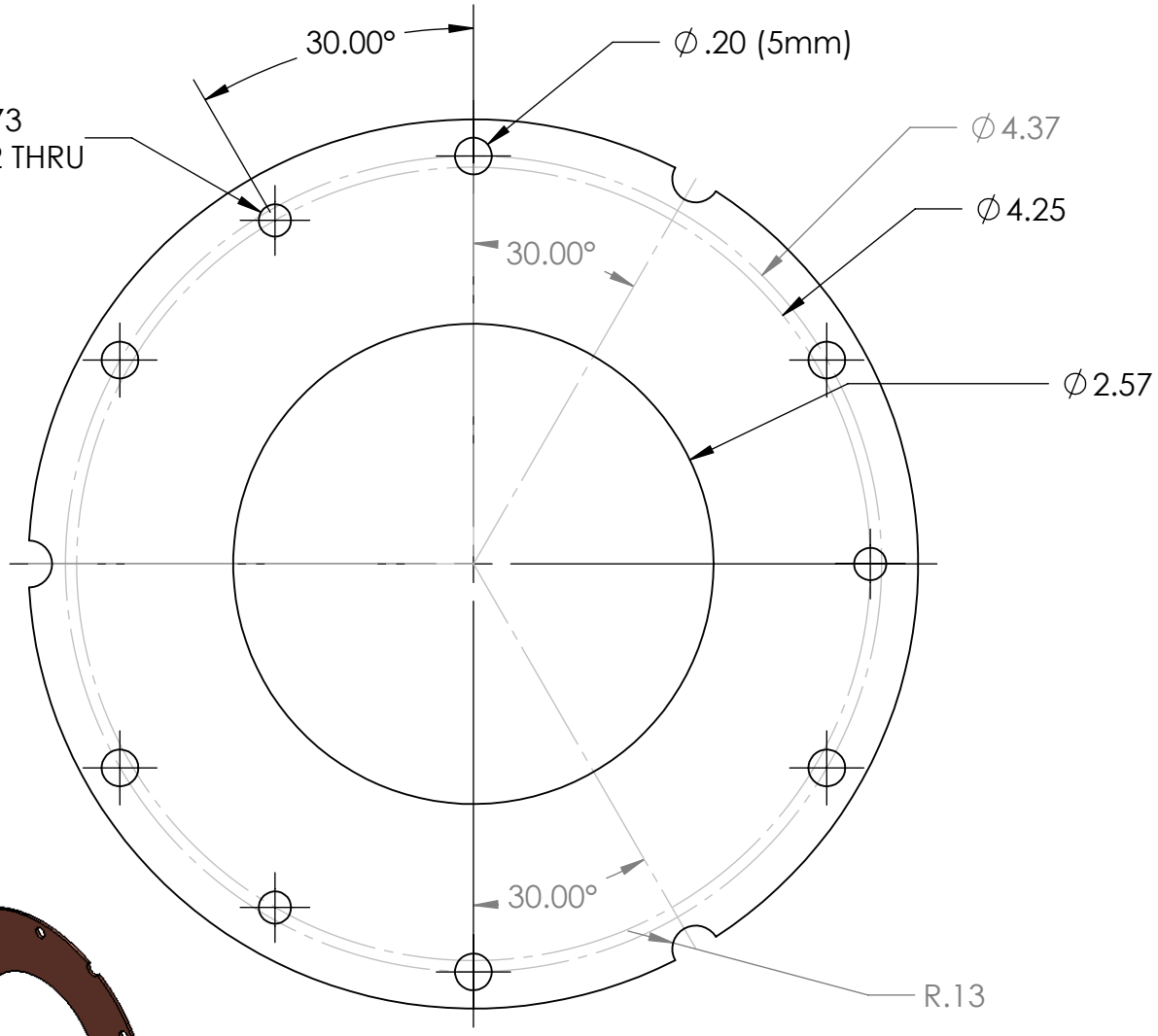
TITLE: **Teflon Disk**

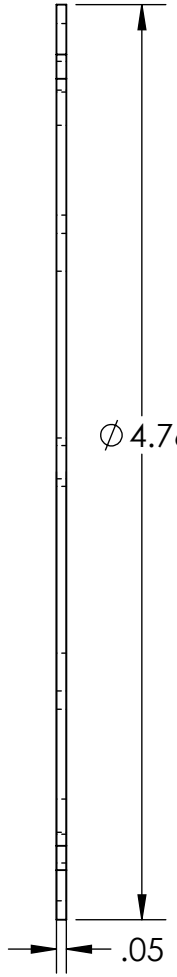
SIZE: A | DWG NO: SU14-007-A01M-P1 | REV: 13

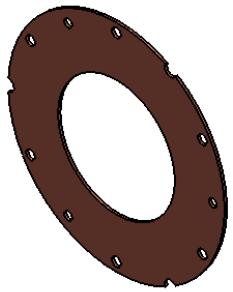
SCALE 3:4 | SHEET 6 OF 6

5 4 3 2 1

D C B A







SolidWorks Student Edition.
For Academic Use Only.

DIMENSIONING AND TOLERANCING PER ASME Y14.5 1994 DIMENSIONS ARE IN INCHES UNLESS OTHERWISE SPECIFIED TOLERANCES ARE AS FOLLOWS UNLESS OTHERWISE SPECIFIED x.x = ±0.03 x.xx = ±0.01 x.xxx = ±0.005 Angles = ±2°			
MATERIAL: Copper			
FINISH			

Mechanical Engineering, Mechatronic Engineering, & Manufacturing Technology
California State University, Chico

Template version 060411

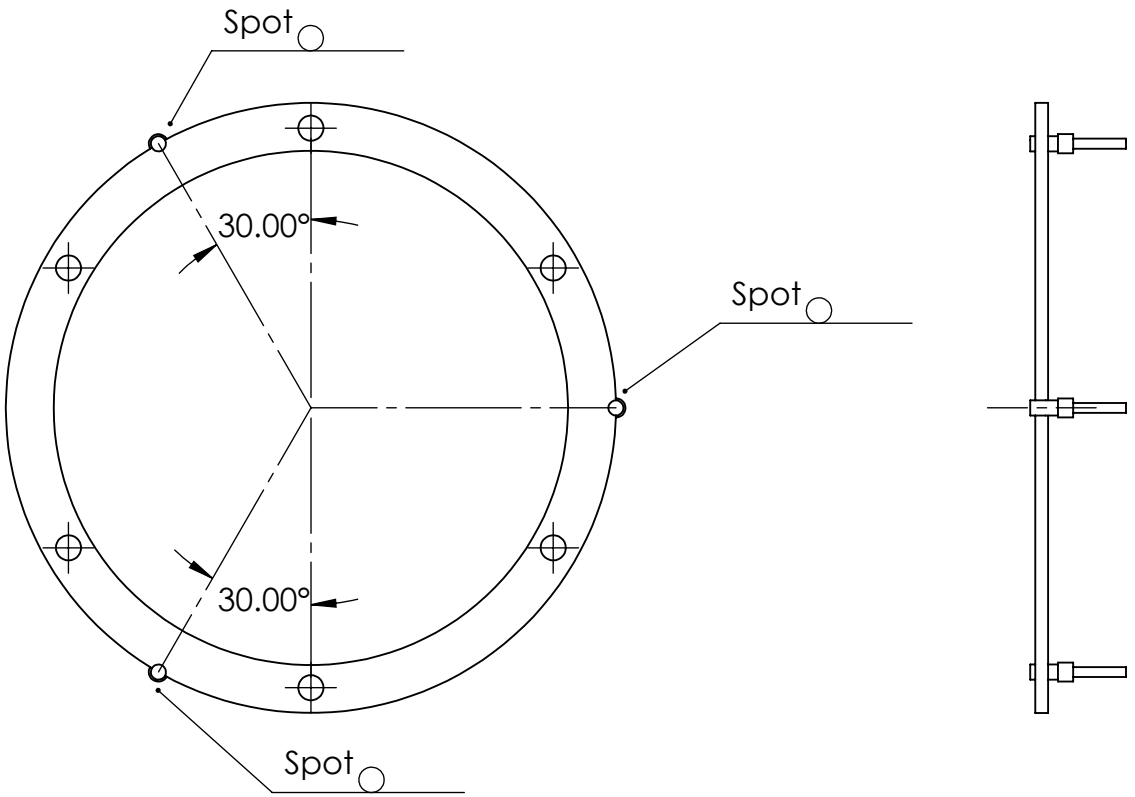
	NAME	DATE	TITLE
DRAWN	L. Heffern	140721	**Cathode**
CHECKED			
ENG APPR			
MFG APPR			
Q A			

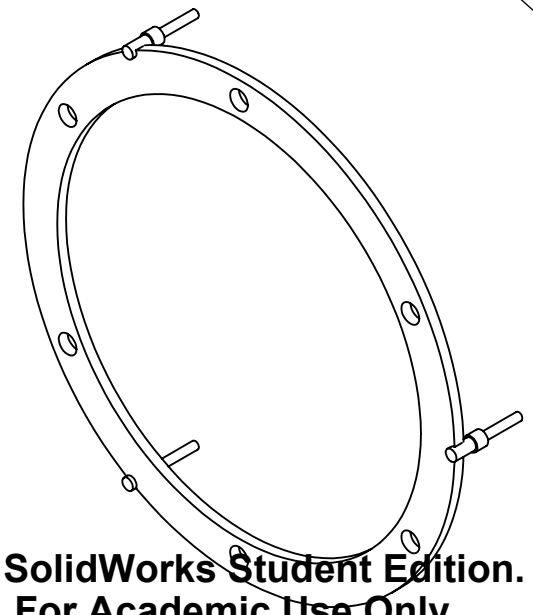
SIZE	DWG NO	REV
A	SU14-007-A02M-P3	2

SCALE 1:1 SHEET 1 OF 1

5 4 3 2 1

D C B A





SolidWorks Student Edition.
For Academic Use Only.

DIMENSIONING AND TOLERANCING PER ASME Y14.5 1994

DIMENSIONS ARE IN MILLIMETERS UNLESS OTHERWISE SPECIFIED

TOLERANCES ARE AS FOLLOWS UNLESS OTHERWISE SPECIFIED

x.x = ±0.1
x.xx = ±0.01
x.xxx = ±0.005
Angles = ±2°

MATERIAL
Cu Supplied

FINISH
N/A

Department of Chemical & Nuclear Engineering
University of New Mexico

Template version 060411

	NAME	DATE
DRAWN	L. Heffern	210714
CHECKED		
ENG APPR		
MFG APPR		
Q A		

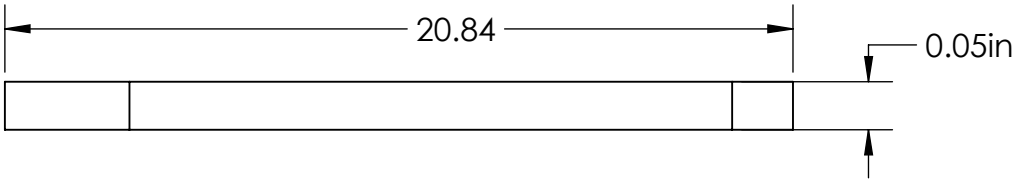
TITLE
Guard Ring Plug

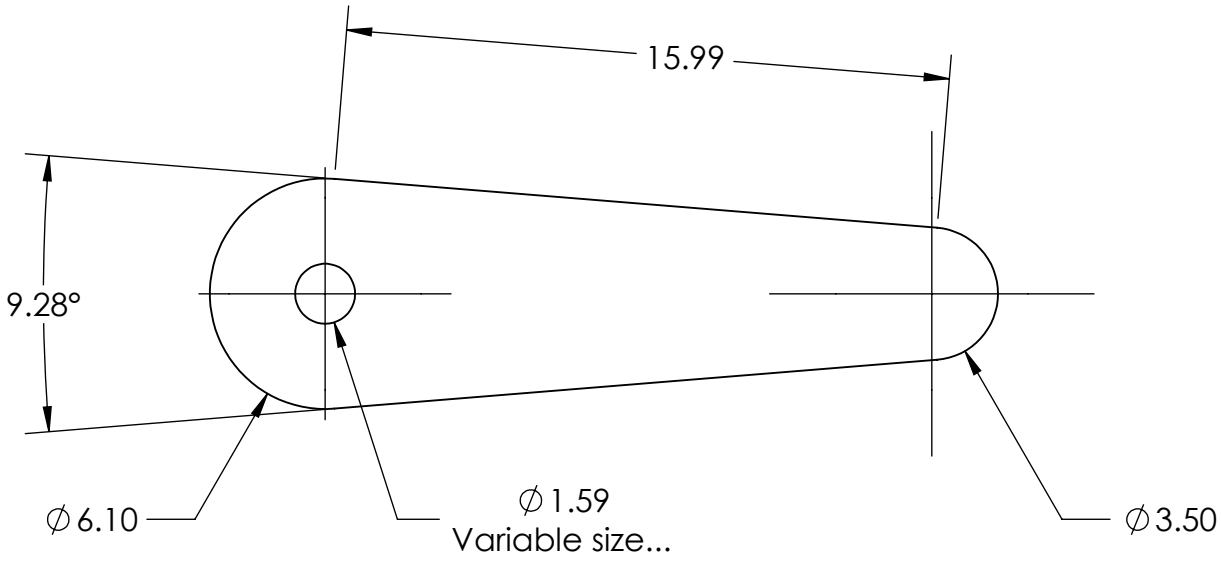
SIZE	DWG NO	REV
A	SU14-007-A01M-SA1	–

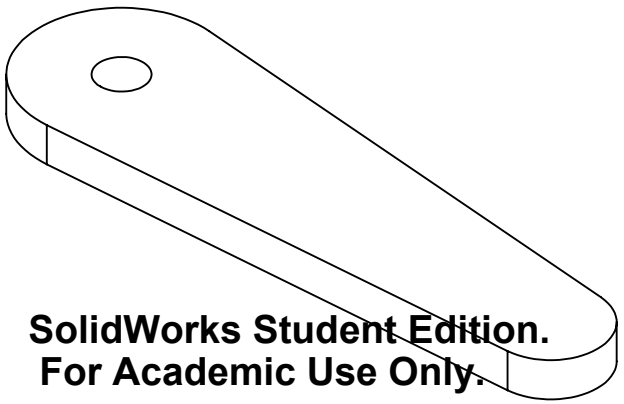
SCALE 2:3 SHEET 1 OF 1

5 4 3 2 1

D C B A







SolidWorks Student Edition.
For Academic Use Only.

DIMENSIONING AND TOLERANCING PER ASME Y14.5 1994	
DIMENSIONS ARE IN MILLIMETERS UNLESS OTHERWISE SPECIFIED	
TOLERANCES ARE AS FOLLOWS UNLESS OTHERWISE SPECIFIED x.x = ±0.1 x.xx = ±0.01 x.xxx = ±0.005 Angles = ±2°	
MATERIAL	Teflon
FINISH	N/A

Department of Chemical & Nuclear Engineering
University of New Mexico

Template version 060411

	NAME	DATE
DRAWN	L. Heffern	210714
CHECKED		
ENG APPR		
MFG APPR		
Q A		

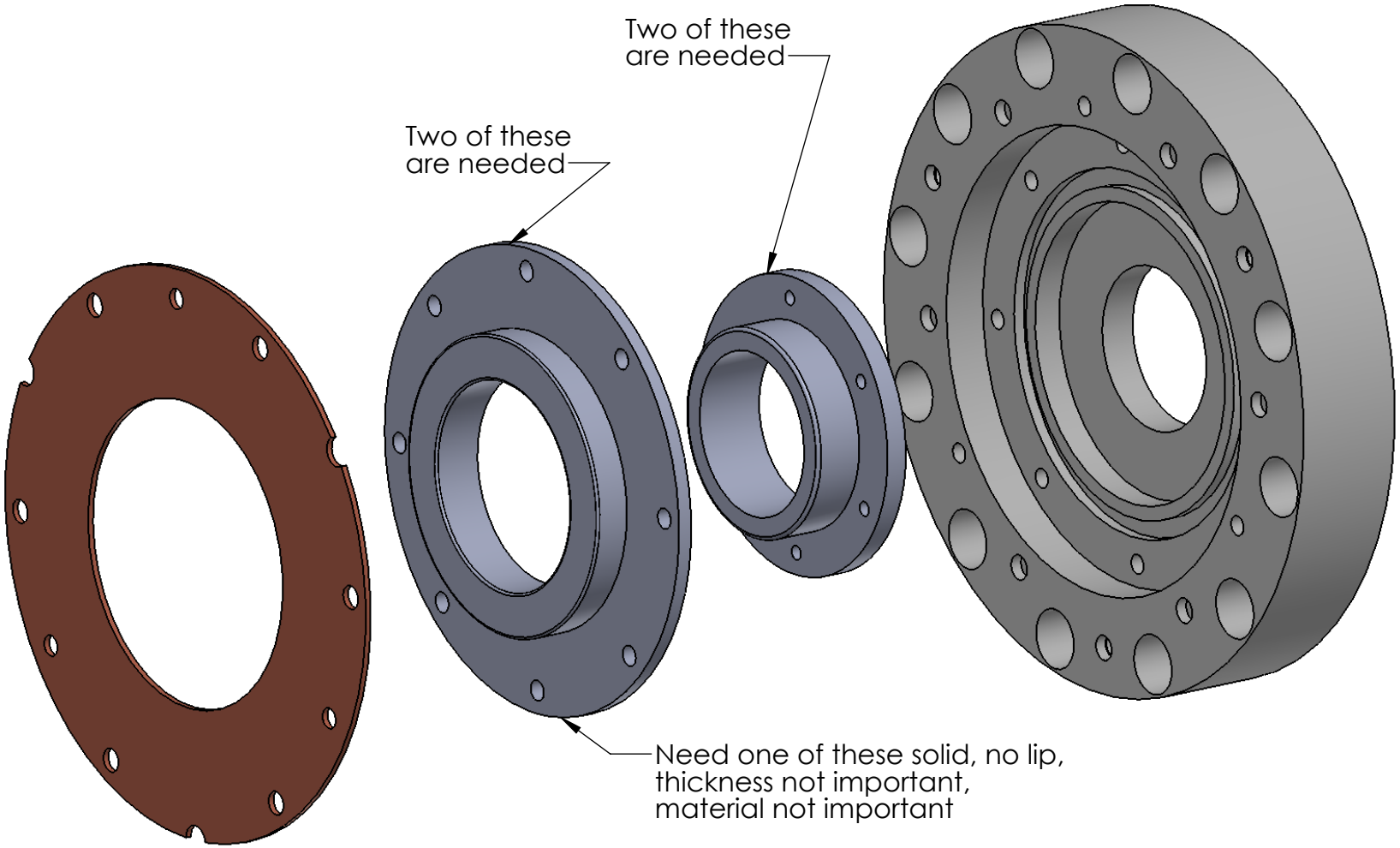
TITLE
Teflon Insert

SIZE	DWG NO	REV
A	SU14-007-A01M-P2	–

SCALE 5:1 SHEET 1 OF 1

5 4 3 2 1

D C B A



		UNLESS OTHERWISE SPECIFIED:		NAME	DATE
		DIMENSIONS ARE IN INCHES TOLERANCES: FRACTIONAL ± ANGULAR: MACH ± BEND ± TWO PLACE DECIMAL ± THREE PLACE DECIMAL ±	DRAWN		
			CHECKED		
			ENG APPR.		
			MFG APPR.		
		INTERPRET GEOMETRIC TOLERANCING PER:	Q.A.		
		MATERIAL	COMMENTS:		
NEXT ASSY	USED ON	FINISH			
APPLICATION		DO NOT SCALE DRAWING			

TITLE:

Window_SubAssembly

SIZE	DWG. NO.	REV
A	13SU-007-01SA	

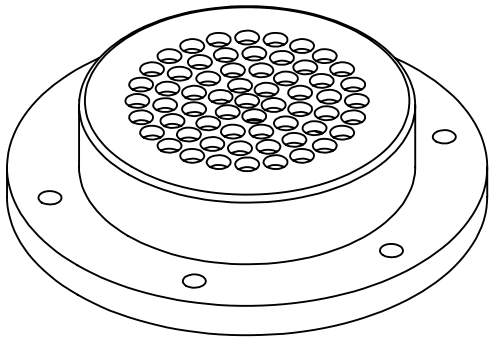
SCALE: 3:4 | WEIGHT: | SHEET 1 OF 1

PROPRIETARY AND CONFIDENTIAL

THE INFORMATION CONTAINED IN THIS DRAWING IS THE SOLE PROPERTY OF <INSERT COMPANY NAME HERE>. ANY REPRODUCTION IN PART OR AS A WHOLE WITHOUT THE WRITTEN PERMISSION OF <INSERT COMPANY NAME HERE> IS PROHIBITED.

SolidWorks Student Edition.
For Academic Use Only

5 4 3 2 1

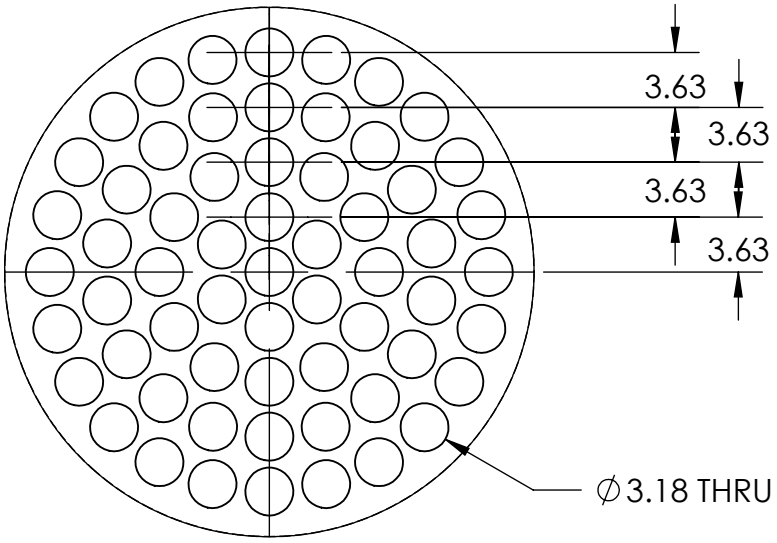


SolidWorks Student Edition.
For Academic Use Only.

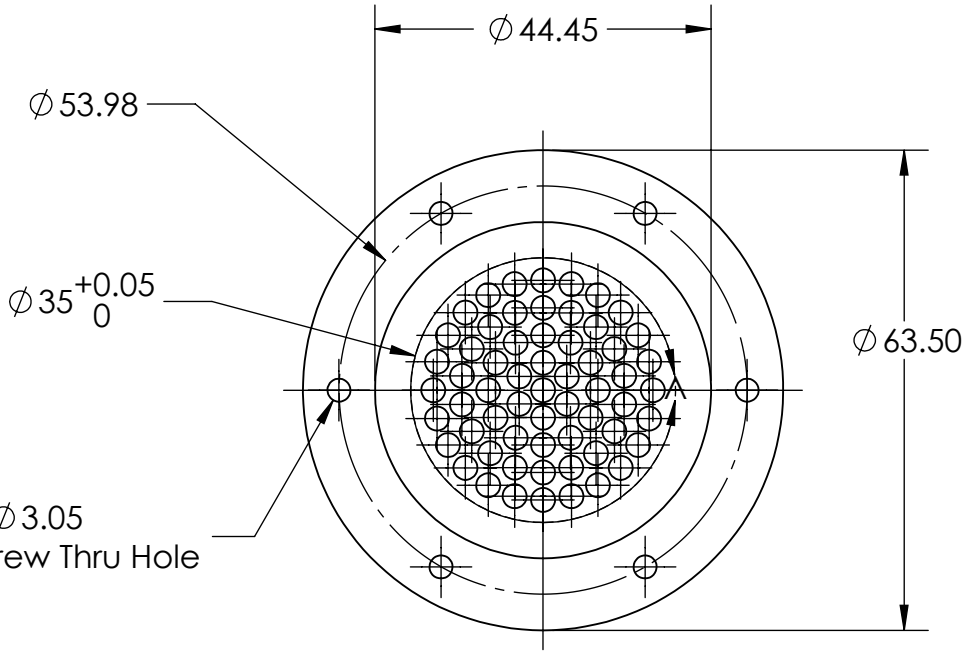
DIMENSIONING AND TOLERANCING PER ASME Y14.5 1994 DIMENSIONS ARE IN INCHES UNLESS OTHERWISE SPECIFIED TOLERANCES ARE AS FOLLOWS UNLESS OTHERWISE SPECIFIED x.x = ±0.03 x.xx = ±0.01 x.xxx = ±0.005 Angles = ±2°			**Department of Chemical & Nuclear Engineering** **University of New Mexico** *Template version 060411*
	NAME	DATE	TITLE
DRAWN	L. Heffern	240314	**Window Grid**
CHECKED			
ENG APPR			SIZE: A
MFG APPR			DWG NO: SP14-007-A02-P01
Q A			REV: –
MATERIAL: 6061 Al			SCALE 1:1
FINISH: N/A			SHEET 1 OF 3

5 4 3 2 1

D C B A



DETAIL A
SCALE 2 : 1



SolidWorks Student Edition.
For Academic Use Only.

DIMENSIONING AND TOLERANCING PER ASME Y14.5 1994

DIMENSIONS ARE IN INCHES UNLESS OTHERWISE SPECIFIED

TOLERANCES ARE AS FOLLOWS UNLESS OTHERWISE SPECIFIED

x.x = ±0.03
x.xx = ±0.01
x.xxx = ±0.005
Angles = ±2°

MATERIAL: 6061 Al

FINISH: N/A

Department of Chemical & Nuclear Engineering
University of New Mexico

Template version 060411

	NAME	DATE
DRAWN	L. Heffern	240314
CHECKED		
ENG APPR		
MFG APPR		
Q A		

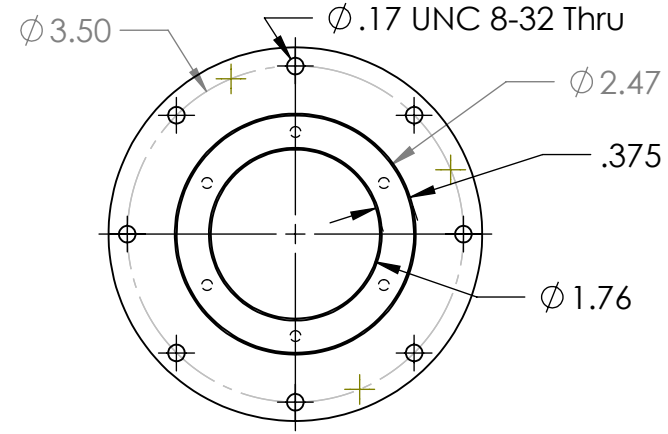
TITLE: **Window Grid**

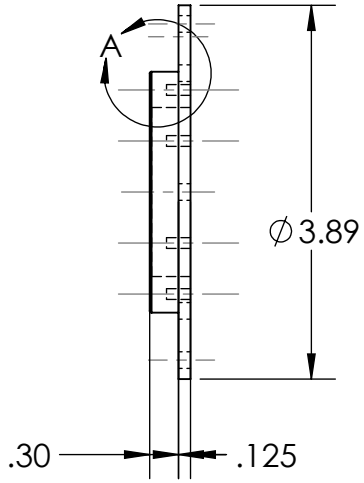
SIZE: A | DWG NO: SP14-007-A02-P01 | REV: –

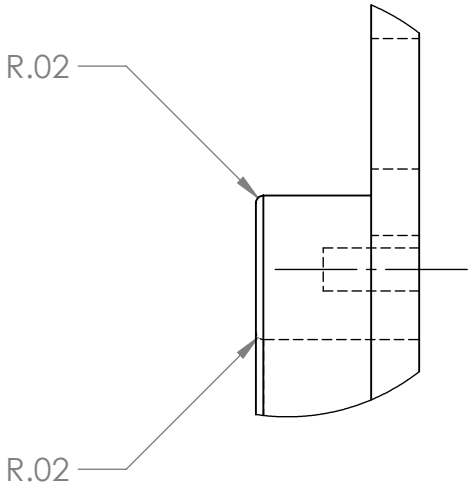
SCALE 1:1 | SHEET 2 OF 3

D C B A

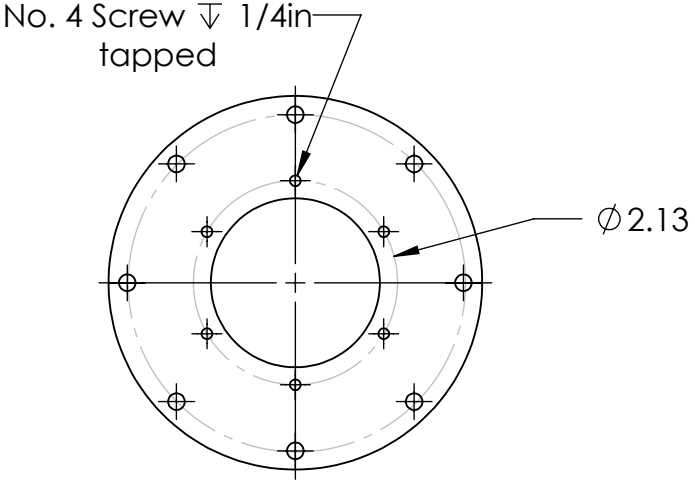
5 4 3 2 1

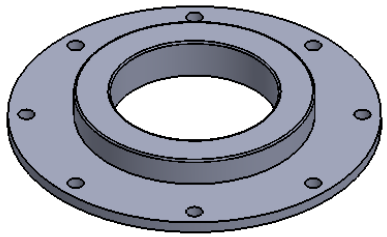






DETAIL A
SCALE 2 : 1





		UNLESS OTHERWISE SPECIFIED:		NAME	DATE
		DIMENSIONS ARE IN INCHES TOLERANCES: FRACTIONAL ± ANGULAR: MACH ± BEND ± TWO PLACE DECIMAL ± THREE PLACE DECIMAL ±	DRAWN		
			CHECKED		
			ENG APPR.		
			MFG APPR.		
		INTERPRET GEOMETRIC TOLERANCING PER:	Q.A.		
		MATERIAL 6061-T6 Al	COMMENTS:		
NEXT ASSY	USED ON	FINISH			
APPLICATION		DO NOT SCALE DRAWING			

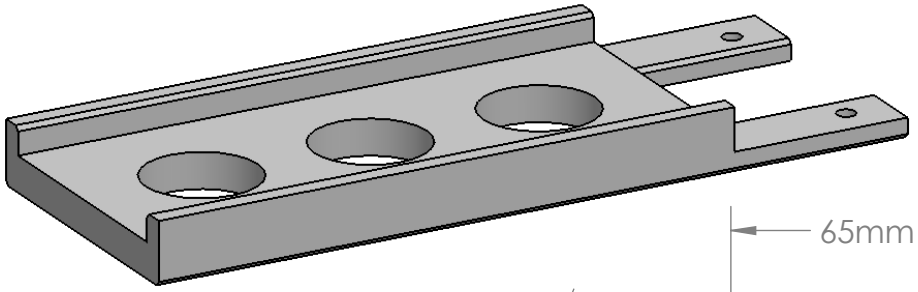
TITLE:
Mylar_Window_Flange

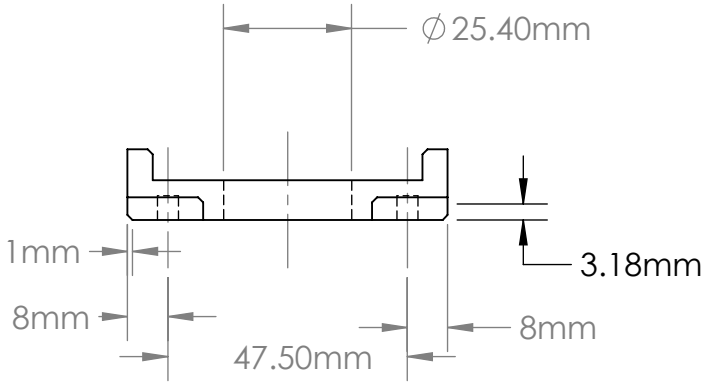
SIZE	DWG. NO.	REV
A	13SU-007-03P	
SCALE: 1:2	WEIGHT:	SHEET 1 OF 1

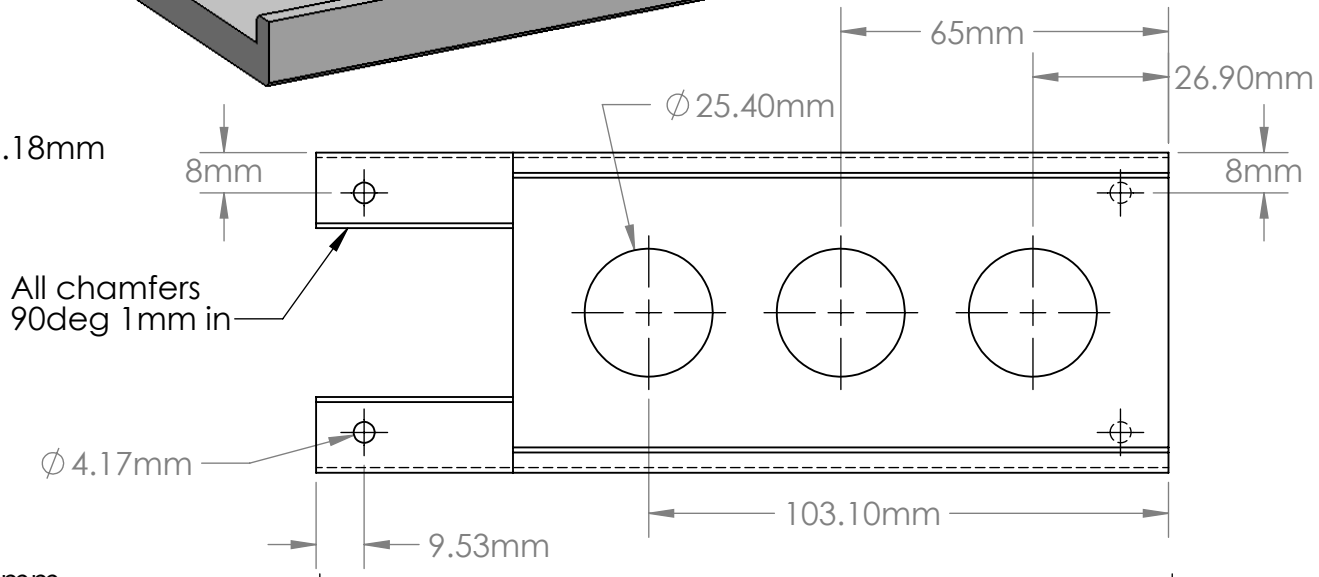
PROPRIETARY AND CONFIDENTIAL
THE INFORMATION CONTAINED IN THIS DRAWING IS THE SOLE PROPERTY OF <INSERT COMPANY NAME HERE>. ANY REPRODUCTION IN PART OR AS A WHOLE WITHOUT THE WRITTEN PERMISSION OF <INSERT COMPANY NAME HERE> IS PROHIBITED.

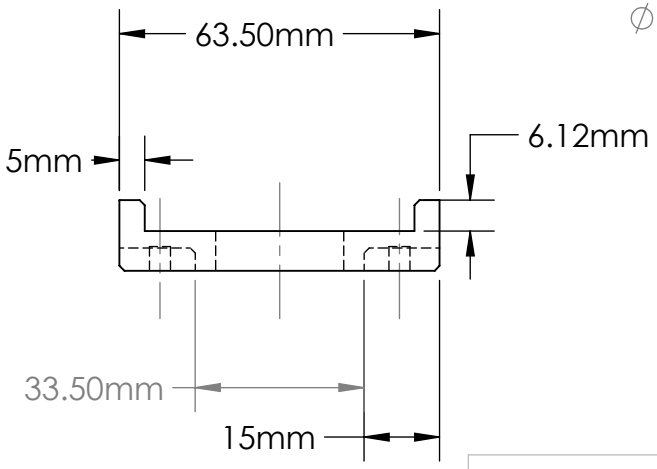
SolidWorks Student Edition.
For Academic Use Only.

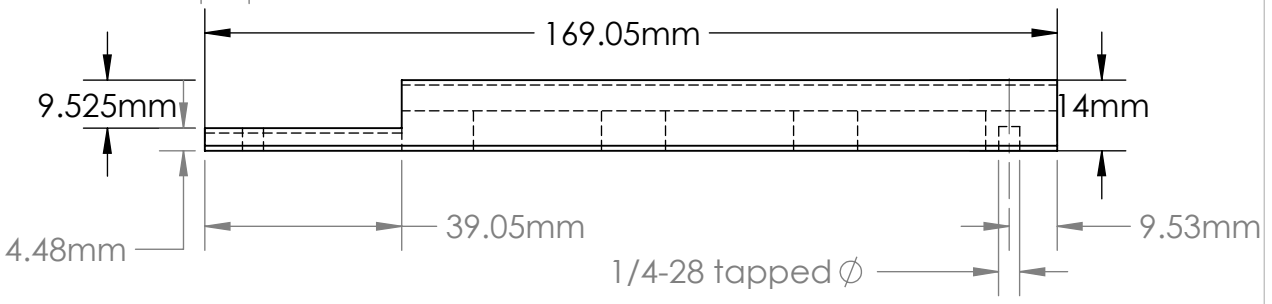
5 4 3 2 1











		UNLESS OTHERWISE SPECIFIED:		NAME	DATE
		DIMENSIONS ARE IN INCHES TOLERANCES: ANGULAR ± 1deg X.X ± 0.03 X.XX ± 0.01 X.XXX ± 0.005	DRAWN		
			CHECKED		
			ENG APPR.		
			MFG APPR.		
			Q.A.		
		INTERPRET GEOMETRIC TOLERANCING PER:	COMMENTS:		
		MATERIAL Teflon			
NEXT ASSY	USED ON	FINISH			
APPLICATION		DO NOT SCALE DRAWING			

UNM

TITLE:

Sled Base metric

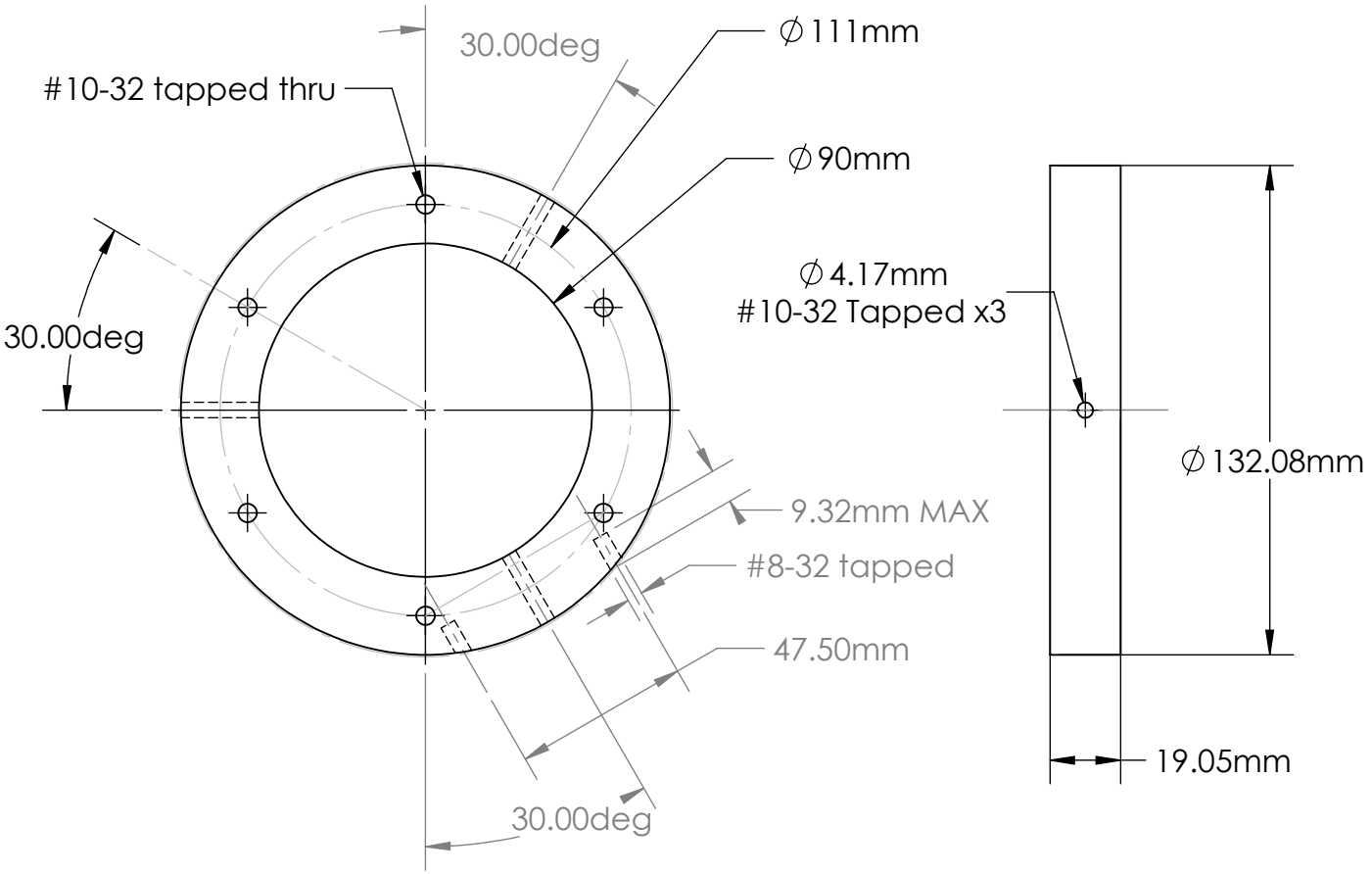
SIZE	DWG. NO.	REV
A	13FA-007-05P	
SCALE: 2:3	WEIGHT:	SHEET 1 OF 1

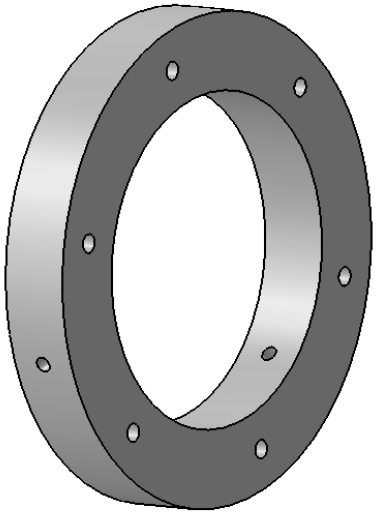
UNCLASSIFIED

THE INFORMATION CONTAINED IN THIS DRAWING IS THE PROPERTY OF the University of New Mexico. ANY REPRODUCTION IN PART OR AS A WHOLE WITHOUT THE WRITTEN PERMISSION OF the University of New Mexico IS PROHIBITED.

SolidWorks Student Edition.
For Academic Use Only.

5 4 3 2 1





		UNLESS OTHERWISE SPECIFIED:		NAME	DATE
		DIMENSIONS ARE IN INCHES TOLERANCES: ANGULAR ± 1deg X.X ± 0.03 X.XX ± 0.01 X.XXX ± 0.005	DRAWN		
			CHECKED		
			ENG APPR.		
			MFG APPR.		
			Q.A.		
		INTERPRET GEOMETRIC TOLERANCING PER:	COMMENTS:		
		MATERIAL Teflon - Supplied			
NEXT ASSY	USED ON	FINISH			
APPLICATION		DO NOT SCALE DRAWING			

UNM

TITLE:

Sled Face Metric

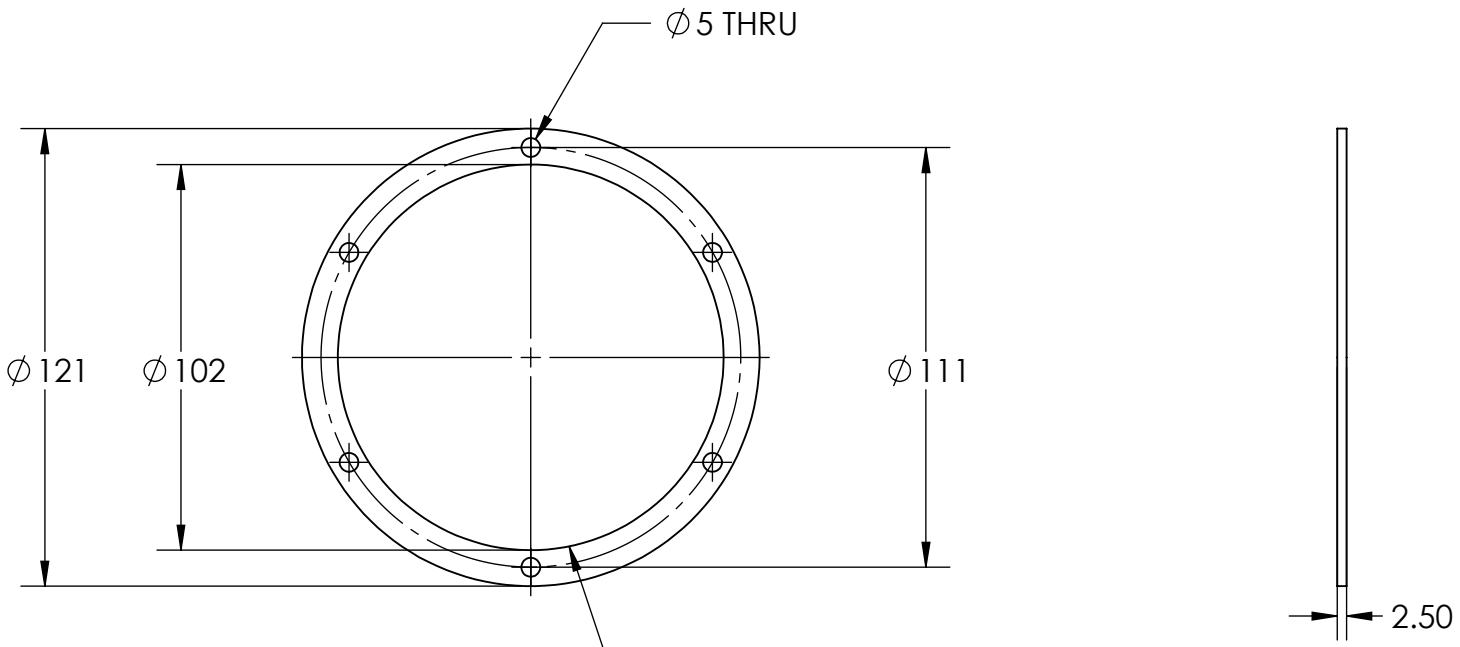
SIZE	DWG. NO.	REV
A	13FA-007-06P	
SCALE: 1:2	WEIGHT:	SHEET 1 OF 1

UNCLASSIFIED

THE INFORMATION CONTAINED IN THIS DRAWING IS THE PROPERTY OF the University of New Mexico. ANY REPRODUCTION IN PART OR AS A WHOLE WITHOUT THE WRITTEN PERMISSION OF the University of New Mexico IS PROHIBITED.

SolidWorks Student Edition.
For Academic Use Only.

5 4 3 2 1



SolidWorks Student Edition.
For Academic Use Only.

DIMENSIONING AND TOLERANCING PER ASME Y14.5 1994

DIMENSIONS ARE IN MILLIMETERS UNLESS OTHERWISE SPECIFIED

TOLERANCES ARE AS FOLLOWS UNLESS OTHERWISE SPECIFIED

x.x = ±0.1
x.xx = ±0.01
x.xxx = ±0.005
Angles = ±2°

MATERIAL: Solid Copper

FINISH: N/A

Department of Chemical & Nuclear Engineering
University of New Mexico

Template version 060411

	NAME	DATE
DRAWN	L. Heffern	080414
CHECKED		
ENG APPR		
MFG APPR		
Q A		

TITLE: **Frisch Grid**

SIZE: A | DWG NO: SP14-007-A02IC-P3 | REV: –

SCALE 1:2 | SHEET 1 OF 1

5 4 3 2 1

D C B A

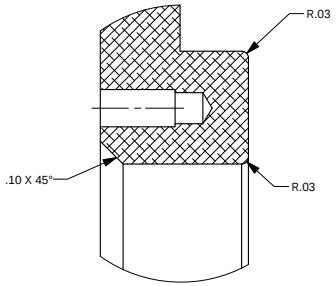
A.2 LANL Window Design Drawings

UNCLASSIFIED

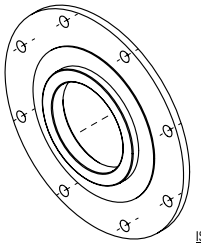
NOTES (UNLESS OTHERWISE SPECIFIED)

104 ABBREVIATIONS PER ASME Y14.38-1999.
200 DIMENSIONING AND TOLERANCING PER ASME Y14.5M-1994.
212 SURFACE TEXTURE SYMBOLS IN ACCORDANCE WITH ASME Y14.36M-1996.
213 SURFACE TEXTURE IN ACCORDANCE WITH ASME B46.1-1995.
226 COUNTERSINK ALL TAPPED HOLES TO MAJOR DIA.
233 REMOVE BURRS AND SHARP EDGES TO .015 MAX.
237 ALL INSIDE CORNERS TO BE R.015 MAX.
500 THOROUGHLY CLEAN PARTS TO REMOVE ALL OIL, GREASE, DIRT, CHIPS, ETC.
900 FOR TECHNICAL QUESTIONS, CONTACT: JUSTIN JORGENSON, 505-665-5536

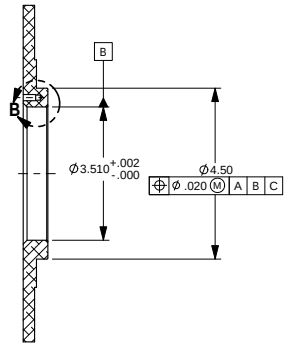
REVISIONS						
ZONE	REV	DESCRIPTION	CHANGED BY	DATE	CLASS REVIEW	APPROVED
	A	INITIAL RELEASE				



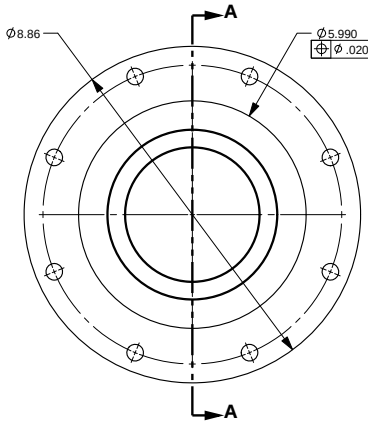
DETAIL B
SCALE 4 : 1

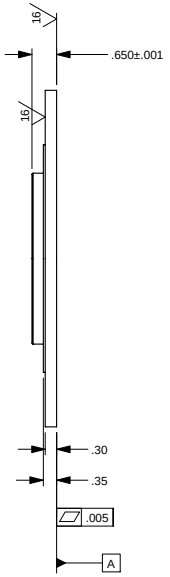


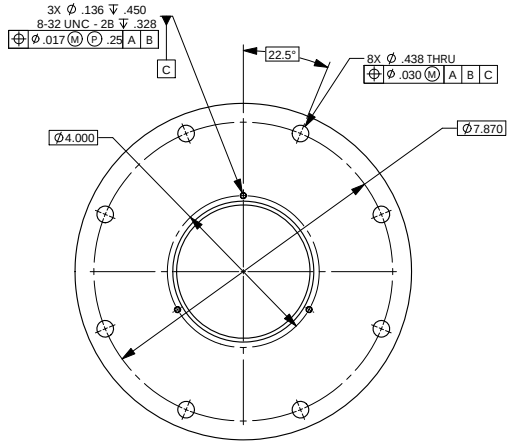
ISO VIEW
FOR REF ONLY



SECTION A-A
SCALE 1 : 1.5







PRELIMINARY
For Information or Review Only
Do Not Use for Fabrication or Procurement
Drawing Content Subject to Future Changes
Date: 7/10/2013

WEIGHT: 1.750 LB, DENSITY: .098 LB/IN^3

QTY REQD	PART OR IDENTIFYING NO.	NOMENCLATURE OR DESCRIPTION	MATERIAL SPECIFICATION	ITEM NO.
5		PLATE	ALUMINUM, 6061-T6	-

PARTS LIST/ BILL OF MATERIAL

CONFIRMED TO BE UNCLASSIFIED

CLASSIFIER: JUSTIN JORGENSON DATE: 07/10/13
DERIVED FROM: DUSA DESIGNATOR ADTO ORG:
DRAWING: UNC PART: UNC

UNLESS OTHERWISE SPECIFIED, DIMENSIONS ARE IN INCHES
TOLERANCES ARE:
.X = ± .03
.XX = ± .01
.XXX = ± .005
ANGULAR = ± 1°
MACHINED FINISH = 63

NEXT ASSEMBLY	USED ON
APPLICATION	

DRAWING LEVEL: DEVELOPMENTAL
TASK CONTRACTOR
A FILLED IN DATE INDICATES THAT THE APPROVAL SIGNATURE HAS BEEN OBTAINED FROM THAT PERSON NR=NOT REQUIRED

INITIAL RELEASE APPROVALS

DESIGNED	J. JORGENSON	AET-5
DRAWN	J. JORGENSON	AET-5
CHECKED		
ENGINEERING	J. JORGENSON	AET-5

Los Alamos NATIONAL LABORATORY
AET-5
PROJECT
LANSCE SPIDER INSTRUMENT
SPIDER SECOND ARM CHAMBER
MYLAR WINDOW FLANGE
DETAIL

SIZE	CAGE CODE	DRAWING NUMBER	REV
D	88516	134Y542691	01

SCALE 1:1 DO NOT SCALE DRAWING SHEET 1 OF 1

Printed on Wednesday, July 10, 2013 6:00:00 PM

SOLIDWORKS DWG TEMPLATE: SW ESA 020214-2 DRAWING: \AET-SRV\\134Y542691.SLDDRW, MODEL: \AET-SRV\\SPIDER MYLAR WINDOW PLATE.SLDPRT-

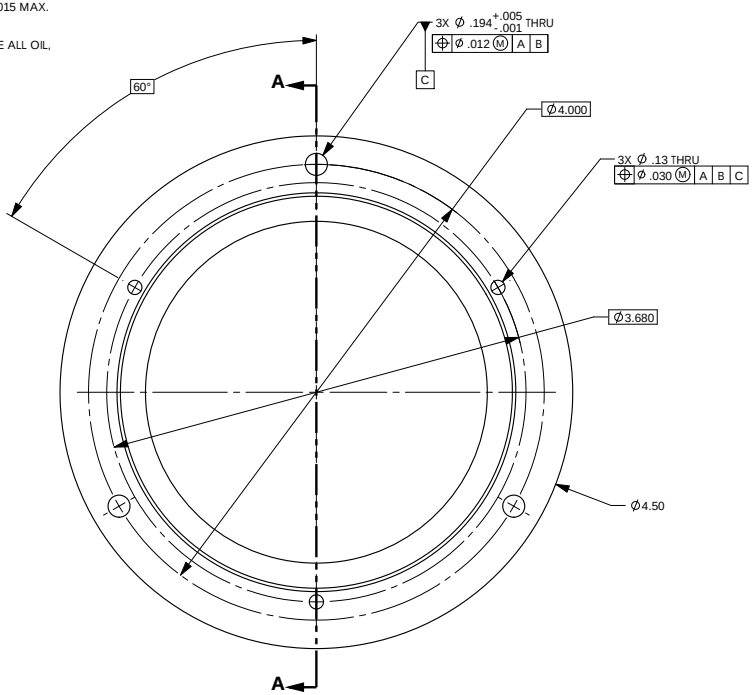
UNCLASSIFIED

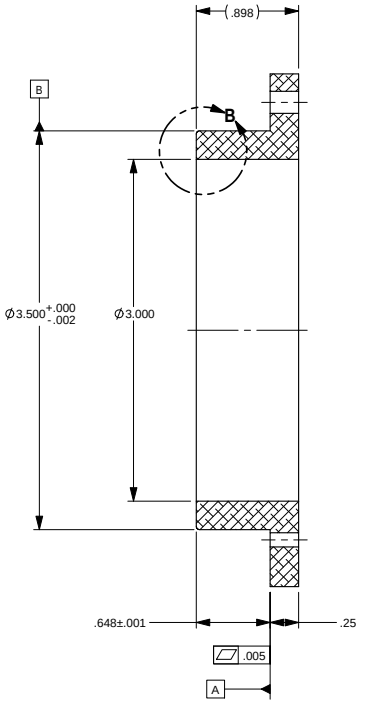
UNCLASSIFIED

NOTES (UNLESS OTHERWISE SPECIFIED)

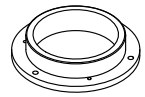
104 ABBREVIATIONS PER ASME Y14.38-1999.
200 DIMENSIONING AND TOLERANCING PER ASME Y14.5M-1994.
212 SURFACE TEXTURE SYMBOLS IN ACCORDANCE WITH ASME Y14.36M-1996.
213 SURFACE TEXTURE IN ACCORDANCE WITH ASME B46.1-1995.
226 COUNTERSINK ALL TAPPED HOLES TO MAJOR DIA.
233 REMOVE BURRS AND SHARP EDGES TO .015 MAX.
237 ALL INSIDE CORNERS TO BE R.015 MAX.
500 THOROUGHLY CLEAN PARTS TO REMOVE ALL OIL, GREASE, DIRT, CHIPS, ETC.
900 FOR TECHNICAL QUESTIONS, CONTACT: JUSTIN JORGENSON, 505-665-5536

REVISIONS						
ZONE	REV	DESCRIPTION	CHANGED BY	DATE	CLASS REVIEW	APPROVED
	A	INITIAL RELEASE				

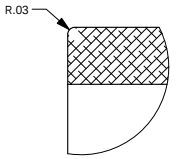




SECTION A-A
SCALE 2 : 1



ISO VIEW
FOR REF ONLY



DETAIL B
SCALE 4 : 1

QTY REQD	PART OR IDENTIFYING NO.	NOMENCLATURE OR DESCRIPTION	MATERIAL SPECIFICATION	ITEM NO.
3		PLATE	ALUMINUM, 6061-T6	-

PARTS LIST/ BILL OF MATERIAL

CONFIRMED TO BE UNCLASSIFIED

CLASSIFIER: JUSTIN JORGENSON DATE: 07/10/13
DERIVED FROM: DUSA DESIGNATOR ADTO ORG:
DRAWING: UNC PART: UNC

UNLESS OTHERWISE SPECIFIED, DIMENSIONS ARE IN INCHES
TOLERANCES ARE:
.X = ± .03
.XX = ± .01
.XXX = ± .005
ANGULAR = ± 1°
MACHINED FINISH = 63

NEXT ASSEMBLY	USED ON
APPLICATION	

DRAWING LEVEL: DEVELOPMENTAL
TASK CONTRACTOR

A FILLED IN DATE INDICATES THAT THE APPROVAL SIGNATURE HAS BEEN OBTAINED FROM THAT PERSON NR=NOT REQUIRED

INITIAL RELEASE APPROVALS

DESIGNED	J. JORGENSON	AET-5
DRAWN	J. JORGENSON	AET-5
CHECKED		
ENGINEERING	J. JORGENSON	AET-5

Los Alamos NATIONAL LABORATORY

AET-5

PROJECT
LANSCE SPIDER INSTRUMENT

SPIDER SECOND ARM CHAMBER
WINDOW GRID FLANGE
DETAIL

SIZE	CAGE CODE	DRAWING NUMBER	REV
D	88516	134Y542690	01

SCALE 1:1 DO NOT SCALE DRAWING SHEET 1 OF 1

PRELIMINARY
For Information or Review Only
Do Not Use for Fabrication or Procurement
Drawing Content Subject to Future Changes
Date: 7/10/2013

WEIGHT: .374 LB, DENSITY: .098 LB/IN^3

SOLIDWORKS DWG TEMPLATE: SW ESA 020214-2 DRAWING: \AET-SRV\\134Y542690.SLDDRW, MODEL: \AET-SRV\\SPIDER MYLAR GRID SUPPORT.SLDPRT-

Printed on Wednesday, July 10, 2013 5:55:14 PM

UNCLASSIFIED

UNCLASSIFIED

NOTES (UNLESS OTHERWISE SPECIFIED)

104 ABBREVIATIONS PER ASME Y14.38-1999.

200 DIMENSIONING AND TOLERANCING PER ASME Y14.5M-1994.

212 SURFACE TEXTURE SYMBOLS IN ACCORDANCE WITH ASME Y14.36M-1996.

213 SURFACE TEXTURE IN ACCORDANCE WITH ASME B46.1-1995.

226 COUNTERSINK ALL TAPPED HOLES TO MAJOR DIA.

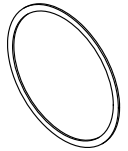
233 REMOVE BURRS AND SHARP EDGES TO .015 MAX.

237 ALL INSIDE CORNERS TO BE R.015 MAX.

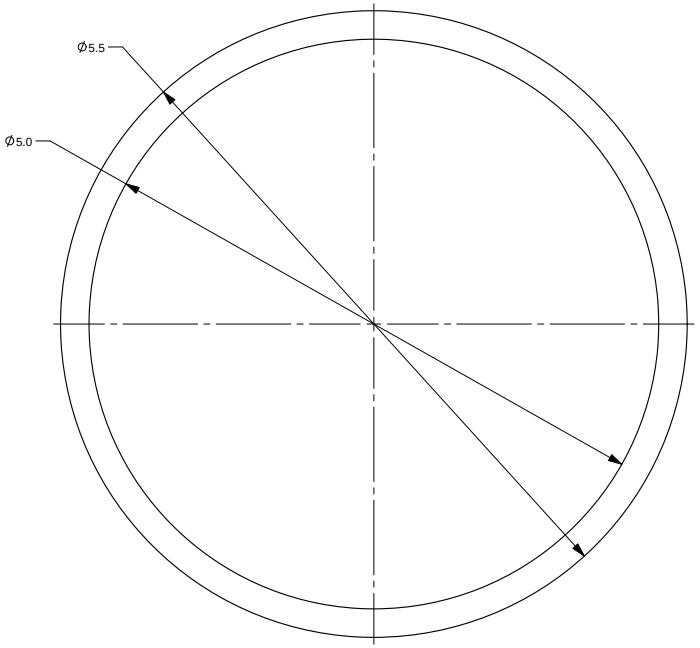
500 THOROUGHLY CLEAN PARTS TO REMOVE ALL OIL, GREASE, DIRT, CHIPS, ETC.

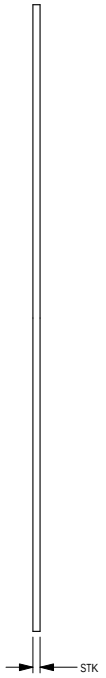
900 FOR TECHNICAL QUESTIONS, CONTACT:
JUSTIN JORGENSON, 505-665-5536

REVISIONS						
ZONE	REV	DESCRIPTION	CHANGED BY	DATE	CLASS REVIEW	APPROVED
	A	INITIAL RELEASE				



ISO VIEW
FOR REF ONLY





PRELIMINARY
For Information or Review Only
Do Not Use for Fabrication or Procurement
Drawing Content Subject to Future Changes
Date: 7/10/2013

QTY REQD	PART OR IDENTIFYING NO.	NOMENCLATURE OR DESCRIPTION	MATERIAL SPECIFICATION	ITEM NO.
1		SHEET, 13 GA., 14 GA., OR 15 GA. THK.	ALUMINUM	-

PARTS LIST/ BILL OF MATERIAL

CONFIRMED TO BE UNCLASSIFIED

CLASSIFIER: DATE:
DERIVED FROM: LA4000 REV 8 ORG: LA
DRAWING: UNC PART: UNC

UNLESS OTHERWISE SPECIFIED, DIMENSIONS ARE IN INCHES
TOLERANCES ARE:
.X = ± .03
.XX = ± .01
.XXX = ± .005
ANGULAR = ± 1°
MACHINED FINISH = 63

NEXT ASSEMBLY	USED ON
APPLICATION	

DRAWING LEVEL: DEVELOPMENTAL

TASK CONTRACTOR

A FILLED IN DATE INDICATES THAT THE APPROVAL SIGNATURE HAS BEEN OBTAINED FROM THAT PERSON NR=NOT REQUIRED

INITIAL RELEASE APPROVALS

DESIGNED	J. JORGENSON	AET-5
DRAWN	J. JORGENSON	AET-5
CHECKED		
ENGINEERING	J. JORGENSON	AET-5

Los Alamos NATIONAL LABORATORY

AET-5

PROJECT
LANSCE SPIDER INSTRUMENT

SPIDER SECOND ARM CHAMBER
MYLAR TENSIONING RING
DETAIL

SIZE	CAGE CODE	DRAWING NUMBER	REV
D	88516	134Y542692	01

SCALE 1:1 DO NOT SCALE DRAWING SHEET 1 OF 1

WEIGHT: .025 LB, DENSITY: .097 LB/IN^3

SOLIDWORKS DWG TEMPLATE: SW ESA 020214-2 DRAWING: \AET-SRV\\134Y542692.SLDDRW, MODEL: \AET-SRV\\TENSIONING RING.SLDPRT-

Printed on Wednesday, July 10, 2013 6:04:10 PM

UNCLASSIFIED

Appendix B

B.1 Environmental DAQ Python Code

```
/*
  DisplayMoreThan5V sketch
  prints the voltage on analog pin to the serial port
  Do not connect more than 5 volts directly to an Arduino pin.
*/
const float referenceVolts = 5;       // the default reference on a 5-volt board
//const float referenceVolts = 3.3;  // use this for a 3.3-volt board
const float R1 = 1000; // value for a maximum voltage of 10 volts
const float R2 = 1000;
// determine by voltage divider resistors, see text
const float resistorFactor = 1023.0 / (R2/(R1 + R2));
const int batteryPin = 0;        // +V from battery is connected to analog pin 0

void setup()
{
  Serial.begin(9600);
}
void loop()
{
  int val = analogRead(batteryPin);  // read the value from the sensor
  float volts = (val / resistorFactor) * referenceVolts ; // calculate the ratio
  float time = millis();
  delay(5000);
  Serial.print(time/1000);  // print a time stamp
  Serial.print("\t");
  Serial.println(volts);  // print the value in volts
}
import processing.serial.*;
Serial mySerial;
PrintWriter output;
void setup() {
  mySerial = new Serial( this, Serial.list()[0], 9600 );
  output = createWriter( "data.txt" );
}
void draw() {
   if (mySerial.available() > 0 ) {
       String value = mySerial.readString();
       if ( value != null ) {
                Output.print(time/1000);  // print a time stamp
                Output.print("\t");
           output.println( volts );
       }
   }
}
```